Towards Surface-Enlarged Diamond Materials

Creation of Surface-Enlarged Diamond Electrodes for Electrochemical Energy Applications

Dissertation

zur Erlangung des Doktorgrades

der Technische Fakultät der

Albert-Ludwigs Universität Freiburg im Breisgau

vorgelegt von

Fang Gao

Dekan:	Prof. Dr. Georg Lausen
Referent:	Prof. Dr. Oliver Ambacher
Korreferent:	Prof. Dr. Jose A. Garrido

Tag der mündlichen Prüfung: 15 Februar 2016

Abstract

Driven by the demand for energy generation and storage systems in portable devices, electrical vehicles and renewable energy for power grids, the past decades have seen a tremendous amount of research on the topic of energy storage and conversion. Devices such as supercapacitors and fuel cells have been intensively investigated. Since energy is either converted or stored at the electrolyte-electrode interface, an important issue for these electrochemical power sources is to enlarge the effective surface area of the working electrode. For this purpose, sp^2 carbon based materials, especially activated carbon, have been widely used in both scientific researches and commercially available products. For this kind of materials, two aspects may be improved. One is the small working potential window in aqueous solutions (~ 1 V), which limits the energy storage. Another is the low stability, especially towards oxidation.

Boron-doped diamond is an electrode material with extreme stability and a wide window of usable potentials even in aqueous solutions. Together with other unrivaled physical and chemical properties, diamond has attracted extensive electrochemical research since 1990s. However, the typical planar diamond electrode has a low surface area, which limits its applicability for energy-conversion and -storage. There has been successful scientific development of nanostructured diamond with enhanced surface areas, but the state-of-the-art technology remains limited regarding the achievable surface enhancement factor. The fabrication of nanostructured boron-doped diamond almost solely depends on reactive ion etching. This method generates vertical structures with a limited aspect ratio and therefore a maximum achievable surface enhancement factor in the range of 10 – 50, which is insufficient for energy applications. The electrochemical applications of these nanostructured electrodes remain limited to electrochemical sensing. Their application in energy related topics has rarely been reported. This thesis introduces an alternative and scalable bottom-up approach for the fabrication of surface-enlarged diamond electrodes, which is capable of producing significantly higher surface enhancements. The potential of these electrodes is investigated in two exemplary energy applications, which profit from the achieved surface enhancement.

This thesis begins with state-of-the-art diamond nanostructuring techniques, i.e. plasma assisted reactive ion etching. The current technology is carefully investigated in terms of limitations and non-ideal effects. Efforts have been made on the theoretic prediction of the wire shapes and achieving maximized surfaces. During this pursuit, the conventional top-down etching technique was found to be insufficient for manufacturing a surface large enough for energy applications. As a result, a new bottom-up approach was developed. In this method, a variety of non-diamond templates have been applied, and diamond coatings were fabricated on them. With this new approach the aspect ratio of diamond nanostructures are no longer limited by the etch-

ing isotopy. Also, the surface enlargement of diamond electrodes becomes fully scalable.

In the second part, the surface enlarged diamond electrodes are investigated for the exemplary energy storage system of electrochemical capacitors, where the surface enhancement is directly translated to an increased capacitance of the device. In the beginning of this part a discussion on electrolyte properties is included, because for supercapacitors the electrolyte plays an important role. Many important properties, like the potential window, the conductivity, as well as the double layer capacitance are all closely related to the chosen electrolyte. Particularly ionic liquids, a new category of solvent-free electrolytes have aroused wide attention, because they can effectively widen the potential window for sp^2 carbon materials up to 4.5 V. However, the combination of diamond and ionic liquid has not been investigated in depth so far. Therefore, in this part the performances of diamond electrodes in both ionic liquids and aqueous electrolytic solutions were investigated. Following this, real double-layer supercapacitor devices based on diamond are assembled and tested. Finally, to further enhance the areal capacitance, a thin coating of pseudocapacitive materials is coated onto the nanostructured diamond samples.

In the final part, diamond-based catalyst systems are investigated as a second possible application of large-surface diamond electrodes, Diamond-supported catalysts can be potentially used in energy related topics such as water splitting and direct-methanol fuel cells, where the high corrosion resistance of diamond plays a crucial role. Both planar diamond and 3D diamond nanostructures were used as robust supports for Pt catalyst. The highest catalytic performance so far reported for a Pt-diamond composite in terms of Pt specific area (m^2/g) has been achieved by diamond-Pt core shell nanowires. This material also shows stability under harsh working conditions.

To summarize, the results from this research provide valuable information for future diamond nanostructuring methods. Also, this work may serve as a pioneering attempt to use diamond as a material for energy conversion and storage. Finally, due to the successful fabrication of diamond nanomaterials with functional coatings, the gate to a group of new diamond-based composite materials is opened.

Zusammenfassung

Aufgrund des immer dringenderen Bedarfs an Energiespeicher- und Energiewandlungssystemen für mobile Elektronik, für Elektrofahrzeuge und für die Stromnetze hat die Forschung an Speicherung und -wandlung von Energie in den letzten Jahrzenten enorm an Bedeutung gewonnen. Systeme wie Superkondensatoren und Brennstoffzellen wurden intensiv erforscht. Derartige Technologien beruhen auf Energiespeicherung/-wandlung an einer Grenzfläche zwischen einer Elektrode und einem Elektrolyten. Aus diesem Grund ist die Erhöhung der Elektrodenoberfläche ein Primärziel dieser Forschung. Hierbei sind sp^2 kohlenstoffbasierte Materialien dominierend, allen voran Aktivkohle, sowohl in der Forschung als auch in kommerziellen Produkten. Für diese Materialklasse besteht jedoch in zwei wesentlichen Punkten Bedarf für Verbesserung. Zum einen wird die pro Oberflächeneinheit speicherbare Energie durch das enge nutzbare Spannungsfenster in wässrigen Elektrolyten (~ 1 V) begrenzt. Zum anderen ist Aktivkohle, besonders unter oxidativen Bedingungen, anfällig für Korrosion.

Bordotierter Diamant hat im Gegensatz dazu ein breites Spannungsfenster, auch in wässrigen Elektrolyten, und ist extrem korrosionsstabil. Von allen bekannten Elektrodenmaterialien hebt sich leitfähiger Diamant seit den 1990er Jahren besonders wegen seiner unerreichten physikalischen und chemischen Eigenschaften ab. Die typische planare Diamantelektrode hat jedoch eine begrenzte Oberfläche, was deren Anwendung in Energiesystemen entgegen steht. Es wurden zwar bereits nanostrukturierte Diamantelektroden entwickelt, diese bleiben aber in der erreichbaren Oberflächenvergrößerung beschränkt. Deren Herstellung beruht auf Plasmaätzen, welches vertikale Strukturen erzeugt. Das maximale Seitenverhältnis dieser Strukturen ist technologisch limitiert, was die erreichbare Oberflächenvergrößerung auf den Faktor 10 – 50 begrenzt, ein Wert der für elektrochemische Energiesysteme unzureichend ist. Elektrochemische Anwendungen dieser Elektroden bleiben daher auf Sensoranwendungen beschränkt. Diese Arbeit stellt einen alternativen und skalierbaren Ansatz zur Herstellung von Diamantelektroden vor, der in der Lage ist eine signifikant höhere Oberflächenvergrößerung zu erreichen. Die damit hergestellten Elektroden wurden auf ihr Potential in zwei Beispielanwendungen aus den Bereichen Energiespeicherung und Energiewandlung untersucht, die direkt von einer vergrößerten Oberfläche profitieren.

Im ersten Teil der Arbeit wird der Stand der Technik zur Herstellung von nanostrukturierten Diamantelektroden beleuchtet und im Hinblick auf dessen Limitierungen evaluiert. Dabei wurde der Versuch unternommen die maximal erreichbare Oberflächenvergrößerung mit einem theoretischen Modell vorherzusagen. Aus diesen Betrachtungen folgt, dass die konventionelle abtragende Ätztechnik nicht zur Herstellung von hinreichend großen Oberflächen für Energie Anwendungen in der Lage ist. Stattdessen wurde ein auftragender Ansatz entwickelt, mit dem iterativ Diamantelektroden mit sehr großer Oberfläche gewachsen werden konnten. Hierbei bleibt die Oberflächen-

vergrößerung voll skalierbar, da die Limitierung auf das Seitenverhältnis der Nanostrukturen entfällt.

Im zweiten Teil der Arbeit wurden die hergestellten Diamantelektroden beispielhaft am Energiespeichersystem elektrochemische Doppelschichtkondensatoren (Superkondensatoren) untersucht, wo sich eine vergrößerte Oberfläche direkt in einer gesteigerten Kapazität niederschlägt. Dieser Teil beginnt mit einer Untersuchung und Diskussion von Elektrolyteigenschaften. Viele Parameter von Superkondensatoren wie das nutzbare Spannungsfenster, der Serienwiderstand aber auch die Kapazität hängen von den Eigenschaften des Elektrolyten ab. Ionische Flüssigkeiten, eine neue Kategorie an lösemittelfreien Elektrolyten, erlauben auch bei Elektroden aus sp^2 Kohlenstoff maximal nutzbare Spannungen von bis zu 4.5 V und haben daher viel Aufmerksamkeit erregt. Deren Kombination mit Diamantelektroden wurde bisher allerdings nicht eingehend erforscht. In dieser Arbeit wurden die Diamantelektroden daher sowohl mit wässrigen Elektrolyten als auch mit ionischen Flüssigkeiten charakterisiert. Daraufhin wurden Superkondensatoren auf Basis von nanostrukturiertem Diamant gebaut und getestet. Schließlich wurde der Ansatz verfolgt die Kapazität der Diamantelektroden weiter durch Aufbringen eines dünnen Films von pseudokapazitiven Materialien zu erhöhen.

Im letzten Teil der Arbeit wurden als weitere Anwendung für oberflächenvergrößerte Diamantelektroden Pt-Katalysatorsysteme untersucht. Derartige Systeme könnten bei der Wasserspaltung oder Methanol Brennstoffzellen Anwendung finden, wo die hohe Korrosionsbeständigkeit von Diamant eine wichtige Rolle spielt. Sowohl planare Diamantelektroden als auch 3D Diamant-Nanostrukturen wurden als robuster Träger für Platin Katalysatoren verwendet und verglichen. Dabei wurde die bisher höchste berichtete katalytische Aktivität von Pt-Diamant Verbundstoffen im Bezug auf die spezifische Oberfläche von Platin (m^2/g) erreicht. Die hohe Stabilität auch unter harschen Bedingungen konnte gezeigt werden.

Die Ergebnisse dieser Arbeit liefern wertvolle Impulse für die Zukunft der Nanostrukturierung von Diamant. Darüber hinaus übernimmt sie eine Vorreiterrolle in der Evaluierung von Diamant als Material für Energiespeicher. Schließlich bereitet die erfolgreiche Verbindung eines funktionellen Materials mit nanostrukturiertem Diamant den Weg für eine neue Kategorie Diamant-Verbundmaterialien.

Some contents in this thesis have appeared previously in the following publications:

[1] F. Gao, C.E. Nebel, Diamond-based Supercapactors: Realization and Properties, ACS Applied Materials and Interfaces, *DOI: 10.1021/acsami.5b07027*

[2] F. Gao, C.E. Nebel, Diamond Nanowire Forest Decorated with Nickel Hydroxide as a Pseudocapacitive Material for Fast Charging-Discharging, Physica Status Solidi (a), 2015;212(11):2533-2538.

[3] F. Gao, R. Thomann, C.E. Nebel, Aligned Pt-diamond Core-shell Nanowires for Electrochemical Catalysis. Electrochem Commun. 2015;50:32-35.

[4] F. Gao, G. Lewes-Malandrakis, M.T. Wolfer, W. Müller-Sebert, et al. Diamond-coated silicon wires for supercapacitor applications in ionic liquids. Diamond and Related Materials. 2015;51:1-6.

[5] F. Gao, M.T. Wolfer, C.E. Nebel. Highly porous diamond foam as a thin-film micro-supercapacitor material. Carbon. 2014;80:833-840.

[6] F. Gao, N.J. Yang, C.E. Nebel. Highly stable platinum nanoparticles on diamond. Electrochimica Acta. 2013;112:493-499.

[7] F. Gao, N.J. Yang, H. Obloh, C.E. Nebel. Shape-controlled platinum nanocrystals on boron-doped diamond. Electrochem Commun. 2013;30:55-58.

[8] F. Gao, N.J. Yang, W. Smirnov, H. Obloh, C.E. Nebel. Size-controllable and homogeneous platinum nanoparticles on diamond using wet-chemically assisted electrodeposition. Electrochimica Acta. 2013;90:445-451

Table of Contents

Abstract i
Zusammenfassung iii
Table of Contents vi
Acronyms viii
Chapter 1: Introduction to the Diamond Nanostructuring 1
1.1 History and Current Situation of the Diamond Nanostructuring 1
1.2 Problem Analysis 2
1.3 Structure of the Thesis 4
Chapter 2: Diamond Nanowires 6
2.1 Background Preparation 6
2.2 Wire Etching Results and Non-ideal Effects 12
2.3 Surface Enlargement Optimization 18
2.4 Summary and Conclusion 21
Chapter 3: Diamond-Coated Wires and Diamond Foam 23
3.1 Diamond-Coated Silicon Wires 23
3.2 Diamond Foam 27
3.3 Summary and Conclusion 38
Chapter 4: Introduction to Diamond-Based Supercapacitors 39
4.1 General Principle for Supercapacitors 39
4.2 Electrolytes for Supercapacitors 41
4.3 Materials for Supercapacitors 42
Chapter 5: Characterization of the Electrolyte Interaction with Diamond 44
5.1 Aqueous Electrolytes 44
5.2 Ionic Liquids 49
5.3 Summary and Conclusion 58
Chapter 6: Performance Tests of Diamond-Based Supercapacitors 60
6.1 Testing Methods 60
6.2 Two-Electrode Measurements 66
6.3 Summary and Conclusion 73
Chapter 7: Pseudocapacitor Systems Based on Diamond Nanostructures 74

7.1 Motivation 74
7.2 Pt-Diamond System 74
7.3 Nickel-Diamond System 80
7.4 Summary and Conclusion 84
Chapter 8: Diamond-Based Materials for Energy Conversion 86
8.1 Diamond Electrodes Decorated with Platinum Nanoparticles 86
8.2 Diamond-Pt Core-Shell Nanowires as Catalyst 93
8.3 Summary and Conclusions 97
Chapter 9: Summary and Outlook 99
9.1 Summary 99
9.2 Outlook 99
Reference 101
Acknowledgement 114

Acronyms

AAO	Anodic Aluminum Oxide
AC	Alternating Current
AN	Aceton Nitrile
BDD	Boron-doped Diamond
BVBM	Valence Band Maximum
CBM	Conduction Band Minimum
CV	Cyclic Voltammetry
CVD	Chemical Vapor Deposition
DC	Direct Current
DF	Diamond Foam
DI	De-Ionized
DiaNW	Diamond Nanowires
DiaSiW	Diamond-coated Silicon Wires
ECW	Electrochemical Window
EIS	Electrochemistry Impedance Spectroscopy
GC	Glassy Carbon
HFCVD	Hot Filament Chemical Vapor Deposition
HOPG	Highly Oriented Pyrolytic Graphite
ICP	Inductively Coupled Plasma
MWCVD	Microwave Chemical Vapor Deposition
NiDia	Nickel-coated Diamond Nanowires
PC	Propylene Carbonate
PtDia	Platinum-coated Diamond Nanowires
PTFE	Polytetrafluoroethylene
RIE	Reactive Ion Etching

SEM	Scanning Electron Microscope
TEM	Transmission Electron Microscope

Chapter 1: Introduction to the Diamond Nanostructuring

1.1 History and Current Situation of the Diamond Nanostructuring

The pursuit of nanostructured diamond surfaces already begins at the end of last century. In 1997, Shiomi *et al* developed the reactive ion etching (RIE) techniques for the creation of diamond structures. Using CF_4/O_2 gas mixtures with Al metal masks, the group successfully patterned a diamond surface [1]. After that, similar top-down etching methods become popular for diamond micro- and nanostructuring, and diamond structures including columns [2], wires [3] and honeycomb structures [4] have been widely fabricated. A large variety of materials have shown suitability as shadow masks for diamond etching, including metals (Al [5], Ni [6], Au [7]), diamond nanoparticles [8, 9] and metal oxides [4, 10]. Invariably, these structures are vertically oriented due to the direction of vertically biased electrical fields during the etching process.

Although seldom reported, there is another approach for the formation of diamond nanostructures, i.e. bottom-up growth. This method was already developed in the middle of the 1990s, called chemical vapor infiltration techniques [11]. The growth process is similar to that of planar poly- or nanocrystalline diamond except that the growth is performed on porous templates with large surface area. The typical templates used in the early days of the development includes carbon fibers [11, 12], silicon carbide whiskers [13], anodic aluminum oxide (AAO) [14] and carbon nanotubes [15]. In later developments, especially in recent years, silicon-based materials, including silicon nanowire [16], silicon oxide spheres [17] and fibers [18, 19] have gained popularity.

The applications of these diamond nanostructures can be clearly divided into physical and chemical categories [20]. The early developments on diamond wires and columns predominantly concern field emissions [1, 21-24]. The tapered shape with a sharp tip significantly enhances the emission rate. Highly ordered structures like diamond honeycombs have been proposed to be used as photonic crystals [25]. More recently, diamond columns containing single color centers have been investigated as a means of promising single photon source [26]. Besides these physical applications, nanostructured diamond films, especially boron-doped ones, have also widely investigated in electrochemistry as scanning probes or sensor electrodes. The already reported results include scanning electrochemical microscopy [27] and the sensing of a large variety of chemicals, such as DNA [3, 8, 9], glucose [28, 29], dopamine[30] and Tryptophan [31].

However, by summarizing the development of diamond nanostructures we find that two aspects remain almost uninvestigated:

1) The fabrication is heavily dependent on the top-down etching methods. The attention paid to the alternative methods is insufficient. While the templated-growth is widely applied in the fabrication of porous materials, the investigation

of templated growth of diamond is rarely reported. Also, the previous studies on diamond nanostructuring seldom emphasize on the surface enlargement. The highest reported surface enlargement value is less than 10 times of a planar surface [6].

2) The application of diamond nanostructures in electrochemistry is limited to sensors. In the energy related topic such as energy conversion and storage, the development is almost blank. Given the importance of energy-related topics for nowadays society, this part of work is worth investigation.

At the same time, we need to notice that the second aspect is caused by the first one. For both energy storage and conversion, the phenomena take place at the electrode-electrolyte interface [32, 33]. Therefore, a large electrode surface area will lead to a multiplication effect. Such examples are easy to find in devices such as supercapacitors or fuel cells, where activated carbon is commonly used to provide large active electrode surface area.

1.2 Problem Analysis

In order to understand the fact that nowadays the surface enlargement technology cannot realize a high specific surface area, we can briefly make an estimation using diamond wires and diamond honeycomb as two examples. **Figure 1-1** shows two kinds of common diamond nanostructures reported previously, namely diamond honeycomb and diamond nanowires. For the estimation, supposing two structures both have the highest density, i.e. a close-pack. With simple geometric relationship, the maximum specific surface areas A_{sp} of these two structures are given by:

$$A_{sp} = \frac{2}{r\rho} \tag{1-1}$$

and

$$A_{sp} = \frac{2\pi}{(2\sqrt{3} - \pi)r\rho} \quad , \tag{1-2}$$

where r is the radius of the wire/hole, and ρ is the density of diamond. In both of the two cases, the surface area is the unary function of r: with smaller pore/wire size, the surface enlargement increase (**figure 1-2**). The typical value of r can be taken from literature. Taking r = 20 nm for wires [6] (**equation 1-1**) and r = 100 nm for honeycomb [4] (**equation 1-2**), the specific surface area is then calculated as 28.6 and 56.1 m^2/g respectively. However, for activated carbon, which is a nanoporous material, the specific area can typically achieve 2000 – 3000 m^2/g [34], which is more than one order of magnitude higher than that reported for diamond [10]. Moreover, the previous diamond nanostructures are mainly processed by plasma etching of bulk diamond samples. The surface area of these vertical structures (such as diamond honeycomb or diamond wires) is limited by the anisotropy of the etching techniques and thus not

suitable for up scaling. Therefore, to achieve a high areal capacitance by increasing the thickness of active layer is not possible for diamond.

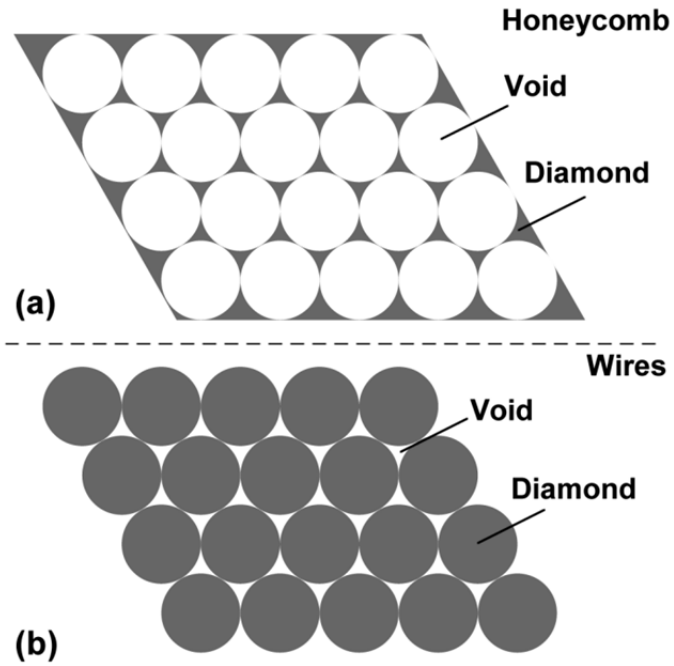

Figure 1-1: Schematic top-views of diamond honeycomb (a) and diamond wires (b).

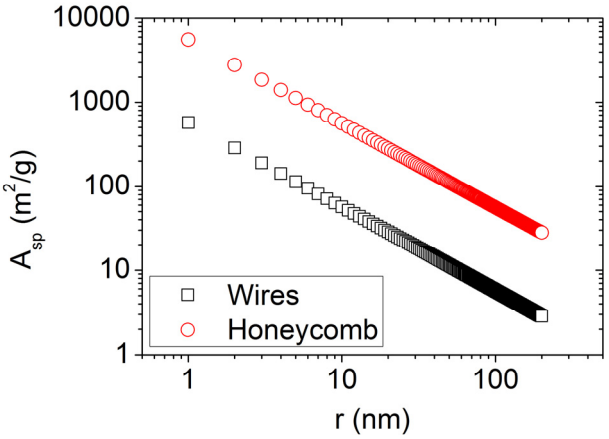

Figure 1-2: The relation between specific surface A_{sp} and hole/wire radius r.

Commercially, activated carbon is available from a variety of resources [35, 36] with reasonable prices (~ 100 euro/kg, Sigma Aldrich), while commercial electrochemical grade polycrystalline diamond costs ~ 10 euro/g. The surface nanostructuring will cause extra cost. Therefore, a lowering of the cost by reducing the amount of diamond used is also very important. Traditionally, diamond nanostructures are fabricated via etching from thick diamond layer which induces high fabrication costs. Therefore, this top-down fabrication may not be suitable for supercapacitor applications.

Motivated by the analysis above, the goal of this PhD work is to achieve large surface enlargement and reduce the fabrication cost. Because of the small gravimetric capacitance (F/g) compared to activated carbon, the targeted application will be micro-devices in which the areal capacitance (F/cm^2) plays an important role [37]. In order to overcome the limitation of top-down etching method, a new bottom-up approach is developed. The idea is to use a cheap, high-surface-area material as growth template for diamond. In this way diamond nanostructuring can be achieved with a small amount of diamond; also, the morphology of the nanostructure is more controllable. The advantages of bottom-up method in comparison with the traditional top-down method are listed in **table 1-1**.

	Top-down	Bottom-up
Starting material	Bulk materials	Gaseous precursors
Diamond thickness	> 5 µm	< 100 nm
Surface enlargement	Not scalable, limited by etching anisotropy	Scalable, by multilayer growth
Morphology controllability	Not controllable, only vertical structures	Controllable, depending on the morphology of templates

Table 1-1: Comparison between top-down and bottom-up approaches.

1.3 Structure of the Thesis

The main structure of the thesis is shown in **figure 1-3**.The thesis will start with a detailed analysis with the existing top-down etching method. Experimentally, the parameters for etching are carefully adjusted to find the optimized surface enlargement. Theoretically, the existing etching model is completed by taking into account non-ideal effects such as the non-cylindrical wire shape and the particle redeposition. An area enlargement of 20 times of a planar surface has been achieved. These results are shown in **chapter 2**. In order to pursuit higher surface enlargement and less diamond consumption, two different diamond structures are fabricated via bottom-up growth method, namely diamond-coated silicon nanowires and diamond foam. Although templated-growth has advantages, there are also obvious difficulties. The most prominent one is the compromise between large surface templates and a good CVD coverage. Up to now, the diamond coverage of complex 3D structures is not widely reported. A detailed discussion of this topic will be provided in **chapter 3**. After dealing with diamond surface enlargement, two energy related applications have been investigated using diamond nanostructures developed in the **chapters 2** and **3**. **Chapters 4** to **7** will be devoted to electrochemical energy storage, and **chapter 8** will elaborate on electro-catalysis for fuel cells. For the supercapacitor study, the electrolytes, especially ionic liquids (ILs), will be studied first. This topic is interesting because the combination of diamond and ILs have not been studied in detail previously. Open questions such as the conductivity, potential window of ILs will be included in **chapter 5**. In **chapter 6**,

supercapacitor devices will be assembled and tested. This is the first supercapacitor device based on diamond. In order to further enlarge the areal capacitance for diamond supercapacitors, highly porous metal oxide coatings are deposited on the diamond nanostructures in **chapter 7** to form "pseudocapacitors". With the help of pseudocapacitive coatings, the capacitance values of diamond electrodes are enhanced by up to two orders of magnitude. With the same idea of a pseudocapacitive coating, catalyst coatings are also deposited on diamond nanostructures in **chapter 8** to develop novel catalyst systems for fuel cell applications. The performance of such a Pt-diamond composite catalyst is comparable to commercial Pt-C catalysts with much higher stability and ability to work under highly corrosive environments.

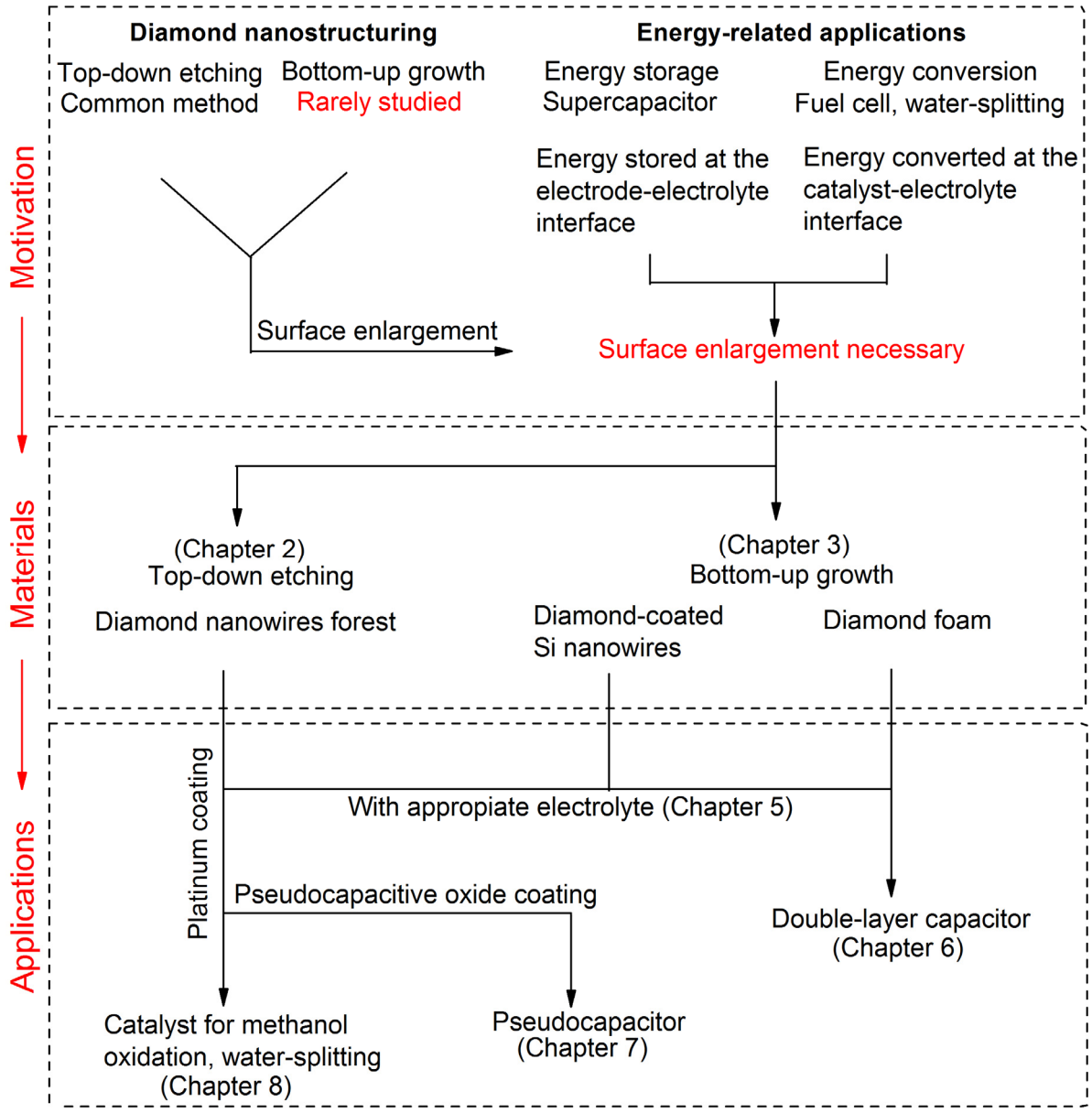

Figure 1-3: The main structure of this thesis.

Chapter 2: Diamond Nanowires

Diamond surface enlargement via nanowires fabrication has been widely reported. Mostly these wires are produced using plasma etching methods [8, 10, 38]. The fabrication method applied in this section has been developed by Smirnov *et al* [6, 39]. In this method, metal nanoparticles from the thermal de-wetting of thin metal films are used as shadow masks. Inductively coupled plasma (ICP) etching is then applied to fabricate diamond nanowires. However, there are still three problems which to be investigated and overcome in order to use the method for the realization of supercapacitor electrodes [6, 39]:

1) The etching parameters have not been optimized for the surface enhancement purpose; previously reported surface enlargement was merely ~ 10 times.
2) The metal particles are treated as stable bulk material; effects like particle shape, mask shrinking and redeposition are not considered.
3) There is no theoretical development about the shape of the wires; wires are considered as cylindrical.

In this chapter, effects of different plasma parameters are investigated in detail. Also, the interaction between the metal mask and plasma is discussed, and a theoretical prediction wire shape will be presented. Finally, the surface enlargements of different nanowire samples fabricated under different etching conditions are measured and analyzed.

2.1 Background Preparation

2.1.1 Nanowires and Surface Enlargement

In order to understand the surface enhancement during etching, theoretical analysis is necessary. Supposing close-packed wires (top view shown in **figure 2-1**) with a radius of r, the density of wires D_w will be given by:

$$D_w = \frac{1}{2\sqrt{3}r^2} \quad . \tag{2-1}$$

Suppose that the wires have cylindrical shape and a same length of L, the total surface area is:

$$A = \frac{1}{2\sqrt{3}r^2} \times 2\pi rL = \frac{\pi}{\sqrt{3}} \times \frac{L}{r} \quad . \tag{2-2}$$

Equation 2-2 gives the expression of enhanced surface due to cylindrical wire formation. It is only related to the aspect ratio of the wires for the close-packed case. Therefore, in order to achieve high surface area, the metal particles used as etching mask should be as dense and possible (ideally close-packing). At the same time, the wires should have a high aspect ratio. This means the etching should be as anisotropy

as possible and the metal particles should endure as long as possible in the etching plasma. In the rest part of this chapter, optimization will be made according to these principals.

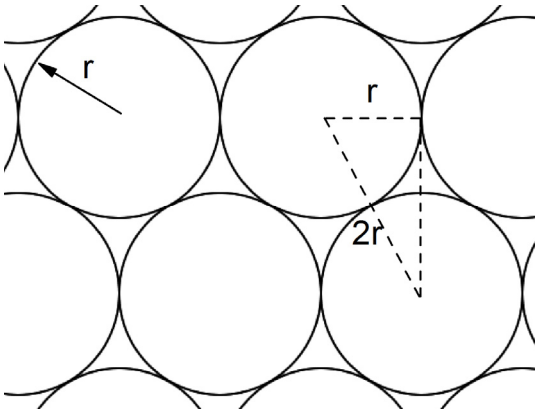

Figure 2-1: Schematic drawing of wires with close-packing, top view.

2.1.2 Starting Material and Characterization Techniques

For the diamond nanowire formation, bulk polycrystalline bulk diamond grown on highly boron-doped Si (100) substrate (resistivity 0.01 Ω/cm) with a thickness of 8 µm is used. The growth of such diamond layer follows the electrochemical requirements: high conductivity and low graphitic content [40]. The growth technique is microwave chemical vapor deposition (MWCVD). The growth parameters are listed in **table 2-1**. The resulting diamond film is microcrystalline, with grain sizes between 1 – 5 µm (**figure 2-2**).

Parameter	Values
Methane (% in H_2 mixture)	2
Microwave Power (W)	3200
Gas Pressure (mbar)	50
Temperature (°C)	750±10
[B]/[C] ratio	4000 ppm

Table 2-1: MWCVD growth parameters for the polycrystalline diamond film used for wire etching.

The surface enlargement provided by diamond nanostructuring is measured electrochemically using a three-electrode set-up (**figure 2-3**). A platinum wire was used as the counter electrode (CE) and a Ag/AgCl/KCl (1M) served as the reference electrode (RE). The nanostructured electrode is contacted to the electrolyte as the working electrode (WE). Cyclic voltammetry was used to characterize the surface enhancement. The capacitive current between ± 0.25 V vs. reference electrode is recorded. The capacitive current of an electrode is proportional to the surface area *A*:

$$I_C = C_n \nu A \quad , \tag{2-3}$$

where I_c is the capacitive current from the charging of the interfacial capacitance C_n (F/cm^2), and ν is the scan rate (mV/s). By comparing the surface area of a nanostruc-

tured sample to a planar diamond electrode, the surface enlargement factor can be calculated.

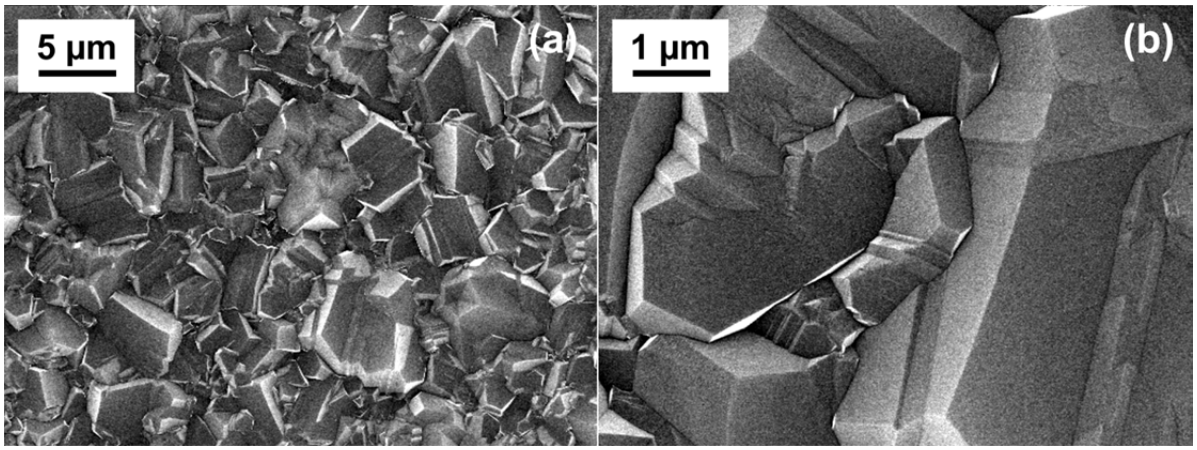

Figure 2-2: SEM images of the polycrystalline diamond film used for wire etching.

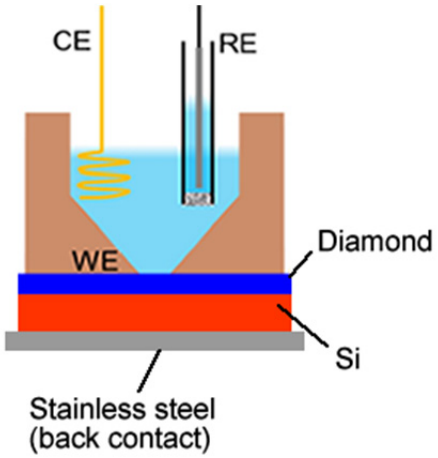

Figure 2-3: Schematic drawing of a three-electrode set-up used in this thesis for electrochemical characterizations. All the nanostructured diamond samples are fabricated on the top of heavily boron-doped Si (100) substrate (resistivity, ~ 0.01 Ω/cm), and contacted from the back of Silicon via a stainless steel plate.

2.1.3 Metal Mask Formation via Thermal Dewetting

The experimental procedures are similar from those reported previously [6]. The metal used in this work is titanium. When the thickness of a metal film is sufficiently thin, the surface/bulk atom ratio raise to a level where its melting temperature is reduced [41]. In this work, Ti films of thicknesses of 2, 3 and 4 nm are deposited on polycrystalline diamond surface via direct current (DC) sputtering. In order to melt the films and form nanoparticles, a temperature of 1000 °C is applied for 1 min. The results are shown in **figure 2-4**. For film thicknesses of 2 and 3 nm, the dewetting generates uniformly distributed Ti nanoparticles. However, when the film thickness increases to 4 nm, the dewetting process generates no longer nanoparticles. Therefore, the dewetting process is very sensitive to the film thickness. The size distribution and density of the na-

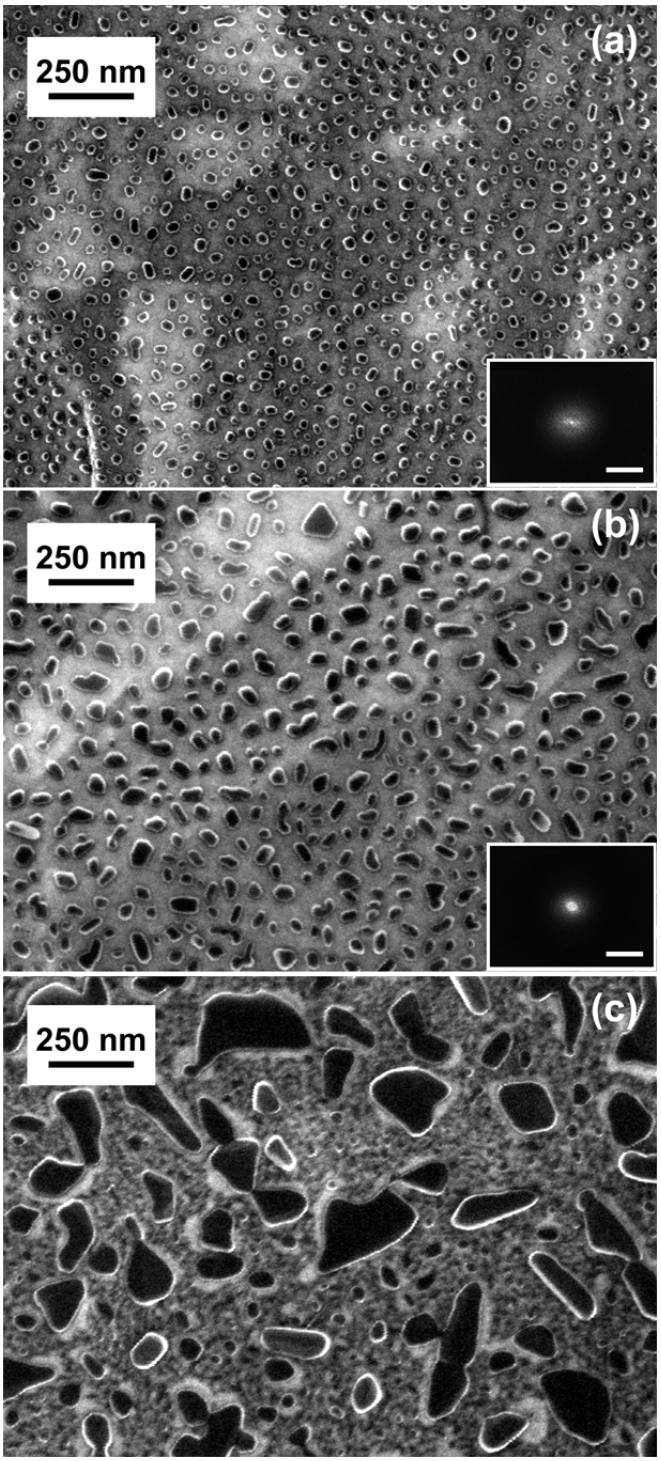

Figure 2-4: Thermal dewetting of (a) 2 nm, (b) 3 nm, and (c) 4 nm Ti films on polycrystalline diamond The dewetting was performed under N_2 atmosphere at 1000 °C for 1 min. The insets show the Fourie transformation of the corresponding image; scar bars are 100 μm^{-1}.

noparticles can be estimated from 2D Fourier transformation of the SEM images, according to the method developed by Smirnov [39]. For 2 nm thick Ti-film, the estimated particle size is 17.4 ± 3.3 nm with a density of 4.1×10^{10} cm^{-2}. For 3 nm film the size increases to 42.3 ± 6.5 nm with a density of 1.6×10^{10} cm^{-2}. Due to the narrow thickness window for metal film dewetting, the controllability of particle size and den-

sity is also limited. Therefore, please note that these particle densities and sizes are not necessarily optimized for the wire etching. In the following sections, the optimization will be made on the etching parameters.

2.1.4 ICP Etching

Among the dry etching processes for diamond, the ICP etching technique has been used extensively for its high plasma density and independent control of ion flux and ion energy [42]. The equipment is schematically drawn in **figure 2-5**. In the ICP etching technique, the plasma is generated inductively via an alternating electromagnetic field (ICP power). Meanwhile, the sample holder is biased via an AC voltage (HF power). During etching, the plasma density is controlled by ICP power and the bias voltage is controlled by the HF power.

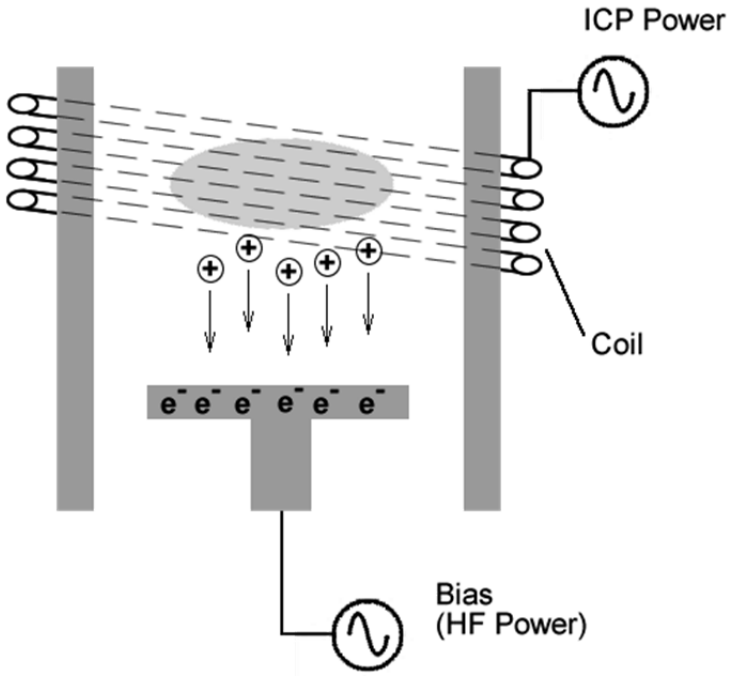

Figure 2-5: Schematic illustration of ICP etching.

Ideally, the wires can be elongated via long time etching, and the surface enlargement will also expand accordingly. Theoretically, if the etching is completely isotropic, the aspect ratio can be infinite (**figure 2-6 a**). However, in reality the mask will shrink with etching time and the ion speed cannot be purely one-dimensional. When the vanishing of the etching mask is not considered, the aspect ratio comes from the ratio between isotropic and anisotropic etching. In the case of no DC bias voltage, the ions' movements in plasma are purely random having speed fractions on all three directions, and the average speed is isotropic. From the etching mechanism, the HF power affects the DC bias during etching. With this bias voltage the average speed on Z-direction is enhanced and become much larger than on the X and Y directions (**figure 2-6 b**), and the etching become anisotropic [38]. Therefore, the aspect ratio of the wires is decid-

ed by the ratio between v_z and v_x. In this way, the larger the HF power, the more isotropic the etching gets, and in the end, the larger the aspect ratio becomes.

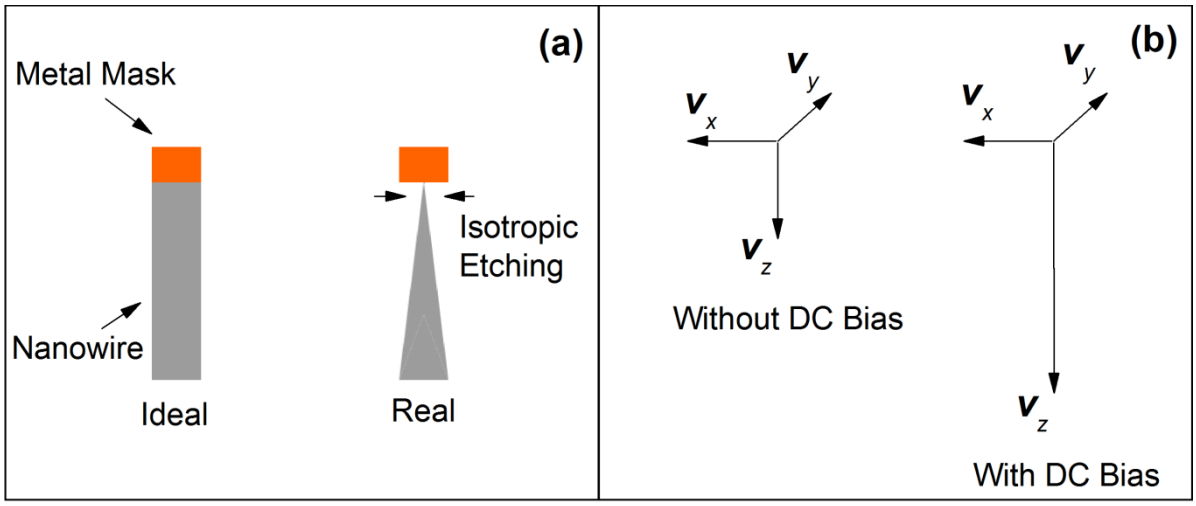

Figure 2-6: (a) Wire etching in ideal and real situations, showing mask-shrinking and under-etching; (b) velocity of ions in plasma, showing the effect of a DC bias.

However, when the vertical bias is increased, the ions will have higher sputtering effect on the mask, which decreases the etching selectivity between diamond and metal. **Table 2-2** indicates this phenomenon. The etching rate of bulk Ti and diamond is measured. At 100 W HF power, the ICP power only has an effect on the etching rate of diamond, while the metal is hardly etched (< 3 nm/min). Selectivity values (the etching rate ratio between diamond and Ti) above 60:1 are achieved. However, when the HF power was increased from 100 W to 150 W with the ICP power constant, the etching rate of metal mask was increased by one order of magnitude to 38 nm/min. The selectivity drops to only ~ 8. This can be explained by comparing the bond strength of diamond and metal. The diamond C–C bond has a very high bond energy of 335 kJ/mol [43], while the Ti–Ti bond energy is only 142 kJ/mol (calculated from the evaporation heat of 425 kJ/mol [44]). As a result, metal is sputtered faster than diamond.

ICP Power (W)	HF Power (W)	Etching Rate of Diamond (nm/min)	Etching Rate of Ti (nm/min)
700	100	180	3
500	100	152	2
500	150	263	38

Table 2-2: Etching rate measured on bulk Ti and Diamond at different etching conditions. For all the etching parameters pure O_2 plasma was used, and the gas pressure is 1.3 Pa. The substrate is water-cooled at 40 °C.

Therefore, 700 W ICP power and 100 W HF is the reasonable parameter for the wire fabrication. According to the data in **table 2-2**, with a selectivity of 60, a semispherical Ti particle of 50 nm can endure for about 8 min in the plasma. If the etching rate of

diamond is 180 nm/min, these particles can be used for fabricating diamond wires up to 1.44 μm.

2.2 Wire Etching Results and Non-ideal Effects

2.2.1 General Observations

The top and side views of diamond wires etched with 700 W ICP power and 100 W HF power are shown in **figure 2-7**. There are four obvious non-ideal effects:

1) The particles are etched much faster than expected. According to **table 2-2**, at

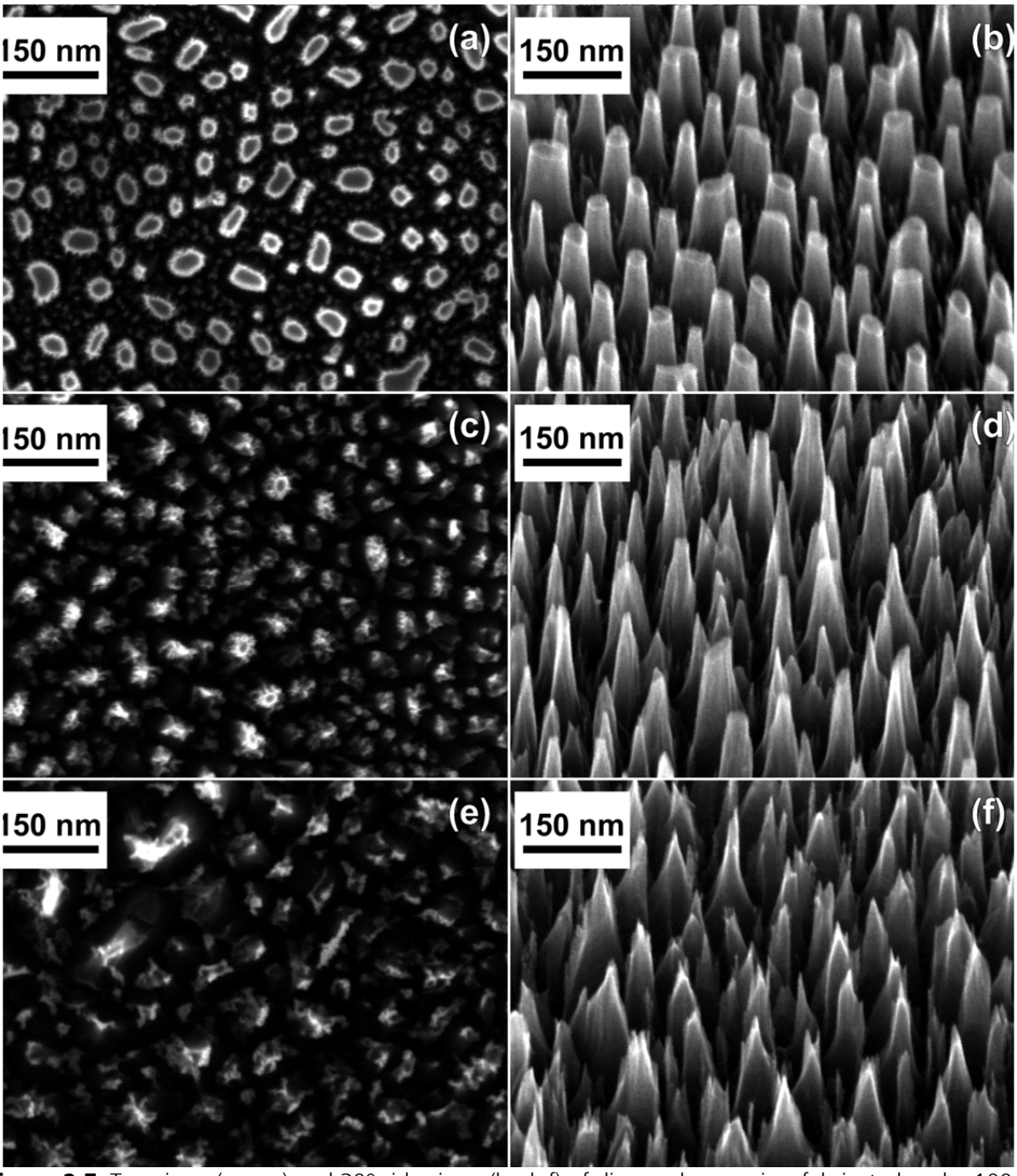

Figure 2-7: Top views (a, c, e) and 30° side views (b, d, f) of diamond nanowires fabricated under 100 W HF power, 1.3 Pa O_2 pressure, with nanoparticle masks from 3 nm Ti-film dewetting, for 3 min (a, b), 5 min (c, d), and 7 min (e, f); etching parameter: 700 W ICP power.

the given etching conditions, the particles should endure at least 8 min. However after only 5 min, the particles already disappear.

2) From the top-view image (**figure 2-7 a**), around the thick diamond wires which resulted from the metal mask there are thin secondary wires which resulted from the redeposition of the metal particles used as shadow masks [45].
3) The sidewalls of nanowires are not vertical showing isotropic etching and/or mask shrinking.
4) The etching rate of wires differs from bulk diamond. After 3 min of etching, the length of wires as measured in SEM (**figure 2-7 b**) is only 240 nm; at 5 min when the mask disappears, the length is only 300 nm.

In the next sections, experiments and discussions will be devoted to understanding these non-ideal phenomena.

2.2.2 Etching Parameters and Redeposition

In order to investigate these four phenomena, masks are fabricated by electron beam lithography on single crystalline diamond. These masks have definite shapes and are remotely separated. Therefore, they are suitable for the investigation of the individual behavior of metal mask under plasma etching. **Figure 2-8** shows a square mask with a size of 1×1 μm^2 after etching with the same parameters as the samples in **figure 2-7** for 4 min. The column is about 850 nm high as measured from the image. From the side-view (**figure 2-8 a**) the high density of the secondary wires are clearly seen. The height of these wires decreases when their distance from the column increases. This phenomenon can be explained by mask redeposition. The redeposition lengths of larger particles are shorter. Therefore, larger secondary masks tend to deposit closer to the column, and thus longer wires grow. From the top-view, a redeposition halo of a width between 100 – 120 nm is clearly seen surrounding the column.

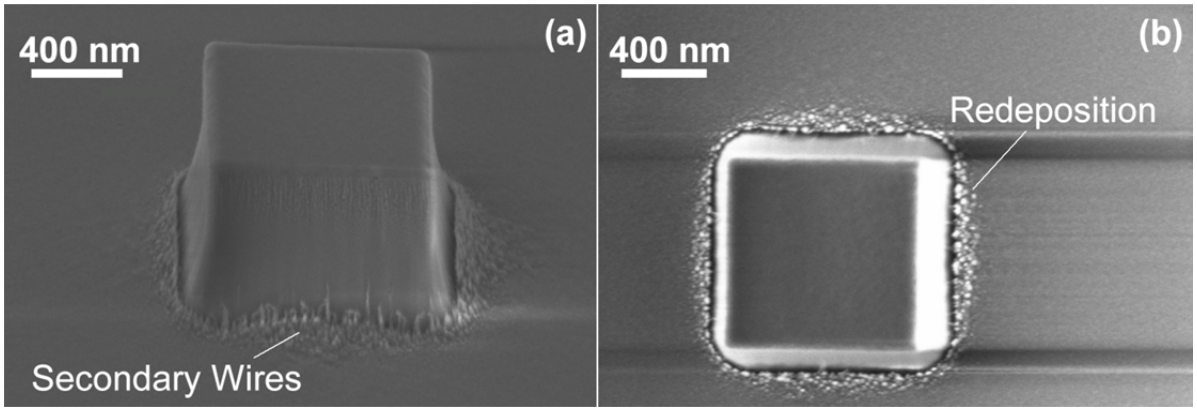

Figure 2-8: Top- and side view of a 1×1 μm^2 Ti mask after 4 min etching at 700 W ICP power, 100 W HF power and an O_2 pressure of 1.3 Pa.

As redeposition is a result of mass transport, it will be related to the energy of the bombarding ions in the plasma. Therefore, lowering the ICP power is expected to curb

the mask redeposition. **Figure 2-9** shows a column etched under 500 W ICP power and 100 W HF power for 4 min with a mask size of 250×250 nm^2. Although a trench is still visible, there is no secondary wires presented, and the redeposition is hardly visible.

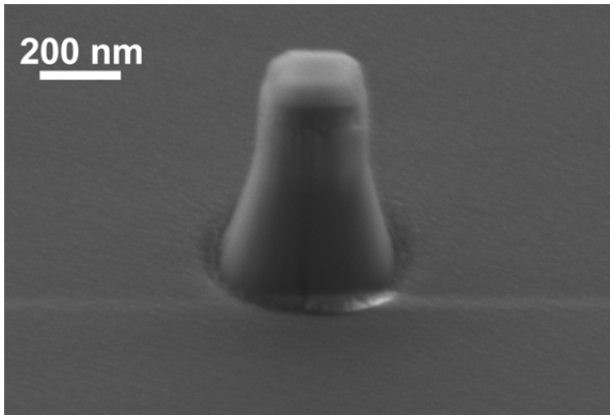

Figure 2-9: Side view of a 250×250 nm^2 Ti mask after 4 min etching at 500 W ICP power, 100 W HF power and an O_2 pressure of 1.3 Pa.

In order to ascertain the relation between redeposition and the bias voltage (HF power), 150 W HF power was used with the rest parameters being the same as the sample in **figure 2-9**. A higher HF power enhances the bias voltage and therefore enhances the sputtering effect. In this case, the secondary wires appear again with evidence of redeposition also in the trench (**figure 2-10**). The mask size shrinks to 157 nm compared to 236 nm in **figure 2-9**. Similar to the situation in **figure 2-7**, the longer secondary wires stick close to the primary column. The lengths of these wires range from 400 to 450 nm. From the top-view, it is confirmed that the redeposited particles (secondary masks) can be transported over 100 nm away from the original position.

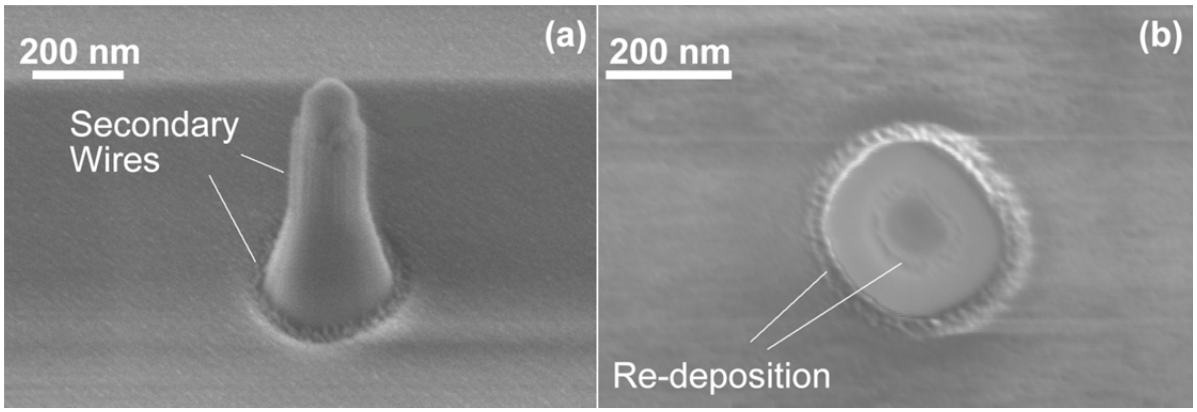

Figure 2-10: Top- and side view of a 250×250 nm^2 Ti mask after 4 min etching at 500 W ICP power, 150 W HF power and an O_2 pressure of 1.3 Pa.

Please note that for both samples in **figure 2-9** and **2-10**, the starting masks are square. However, after etching (especially with higher HF power) the corners disappear and the particles become dome-shaped. Also, as a result of this, the resulting wires are

also conical rather than prismatic. This effect shows that the sharp edges and corners are more susceptible to the etching. If we consider a bulk mask, as we used to measure the etching rate, this edge effect can be neglected. In the case of metal nanoparticle, however, most of the mask is edge. Therefore, it is understandable that why the bulk etching rate failed to predict the duration of the metal particles.

2.2.3 Sidewall-Shape Discussion

In the **section 2.2.2**, the edge effect of an etching mask is discussed, and given sufficient time, faster etching at the edge turns a square mask into a dome one. Here, a theory is built upon this fact, and the tapered shape of the resulting wire is explained. In the following discussions, isotropic etching is neglected, i.e. the velocities of the reactive ions are purely in z-direction. Also, in order to describe the etching process, the following two assumptions are made:

1) Etching is a result of collision between ions and the substrate.
2) The etching rate is proportional to the normal fraction of the kinetic energy of the ions. In another word, the energy fraction parallel to the slop will lead the ions to "slip" down, and this will not change the slop of a sidewall.

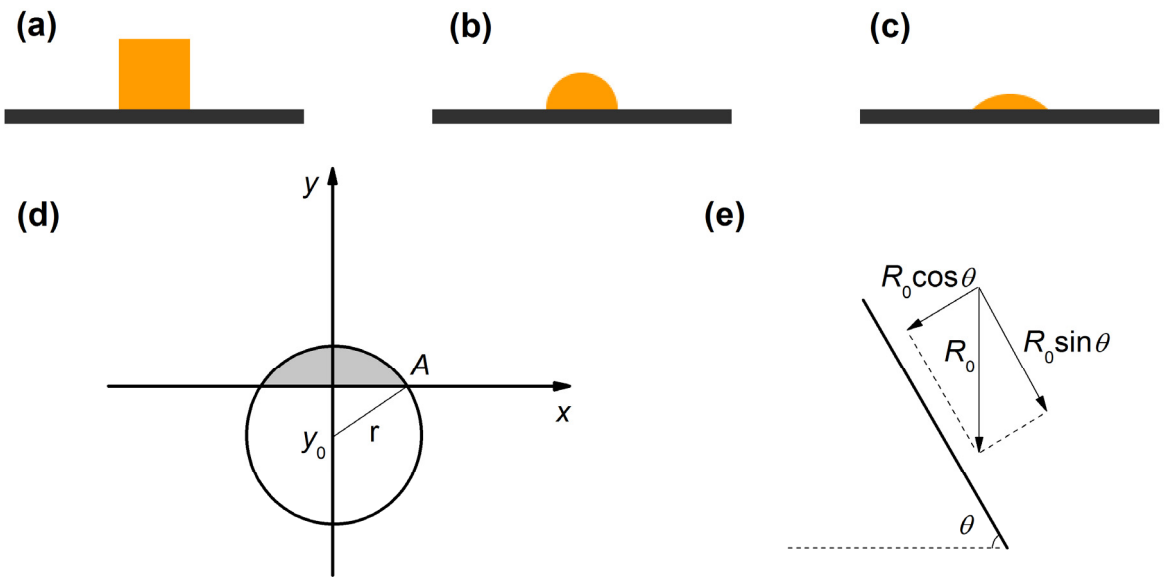

Figure 2-11: Three different shapes of particles: cubic (a), hemispherical (b), and spherical dome (c); (d) the coordinate system used for the calculation; y_0 is the y-coordinate of the center of the dome; (e) the decomposition of etching speed on a slope with elevation angle θ.

Figure 2-11 (a) to **(c)** shows three different shapes of particles as etching masks: cubic, hemispherical, and spherical dome. For the cubic case, it is apparent that the sidewall of the particle is vertical, and the normal fraction is 0. Therefore, the particle will not undergo horizontal etching, and the particle size will not shrink on the horizontal di-

rection. For the latter two cases, we can write the function of the particle outline with the function of a circle (**figure 2-11 d**):

$$y = y_0 + \sqrt{r^2 - x^2} \quad , \tag{2-4}$$

In the case of semispherical particle, y_0=0. The slope of the outline is then expressed as:

$$y' = -\frac{x}{\sqrt{r^2 - x^2}} \quad . \tag{2-5}$$

At the intersection of the particle outline and the substrate (coordination (*A*, 0)), the slop is:

$$\tan\theta = {y_A}' = -\frac{\sqrt{r^2 - {y_0}^2}}{y_0} \quad , \tag{2-6}$$

and

$$\cos\theta = \frac{\sqrt{r^2 - x^2}}{r} \quad . \tag{2-7}$$

From **presumption 2)**, the time varied outline function of the particle is:

$$y(t) = y_0 + (1 - \frac{R_m}{r}t)\sqrt{r^2 - x^2} \quad , \tag{2-8}$$

where R_m is the etching rate of the mask material. Here the time is $t < (r - y_0)/R_m$.

In the case of a semispherical particle, $y_0 = 0$, the outline is an ellipse with a constant semi-major axis value $A = r$, which means the particle will not shrink in the *x* direction. From the expression of the slope we can also get this conclusion: when $y_0 = 0$ the slop is infinite, so the etching will not happen horizontally at this point. Therefore the situation is the same as the cubic particle.

When $y_0 > 0$, which corresponds to a doom shape, the coordinate *A* is not a constant any more. The time-dependent expression of *A* is:

$$A(t) = \sqrt{r^2 - (\frac{y_0}{1 - \frac{R_m}{r}t})^2} \quad , \tag{2-9}$$

showing the particle will shrink over time. The tip of the wire is always equal to the size of particle; therefore, the tip of the particle will also shrink, resulting in a tapered wire. This is similar to the effect of isotropic etching, but is originated from the shape of the etching mask. Also, as can be calculated from **equation 2-9**, the life time *t* of a dome-shaped particle is (i.e. when *A*=0):

$$t = \frac{r - y_0}{R_m} \quad , \tag{2-10}$$

which is smaller than the life time of a hemispherical mask (r/R_m).

Now, let us deduce the shaped of the wire under a dome-shaped mask. Supposing the 2-dimensional sidewall function is $y = f(x)$, and the etching rate on a flat diamond surface is R_0. On the sidewall surface, the local etching rate is:

$$R(x) = R_0 \cos\theta \quad , \tag{2-11}$$

,where θ is the elevation angle, which is a function of x. Since $\tan\theta$ equals to $f'(x)$ which is the local slope of the sidewall function, we have:

$$\cos\theta = [1 + f'^2(x)]^{-\frac{1}{2}} \tag{2-12}$$

and

$$R'(x) = -\frac{f'(x)f''(x)}{[1 + f'^2(x)]^{-\frac{3}{2}}} \quad . \tag{2-13}$$

Due to the shrinking of the particle, the sidewall of the wire should be tilting inwards, i.e. $f'(x) < 0$. Therefore, the sign of $R'(x)$ depends on the sign of $f''(x)$. $f''(x) > 0$ and $f''(x) < 0$ stand for two different wire types (**figure 2-12 a**).

1) If $f''(x) < 0$, indicating $f(x)$ is a concave function, then $R'(x) < 0$. The physical meaning is that the etching rate decrease with increasing x. However, this is not possible because the etching rate at the point infinitely close to the wire/mask interface is zero which is already the minimum, and etching rate cannot be negative.
2) If $f''(x) = 0$, meaning the sidewall is linear. Given a constant slop, the etching rate at each point of the sidewall (including the point infinitely close to the wire/mask interface) is a constant. This is contradicting with the previous expression of the shrinking of the mask which is not a linear function. Also, this shows clearly that the wire cannot be exactly cone-shaped.

Therefore, $f''(x) > 0$, indicating $f(x)$ is a convex function. Also, this means $R'(x) > 0$ (**equation 2-13**), meaning that the etching rate decrease with increasing x. In this way, the part on the sidewall with smaller slopes will have higher etching rates, while the steeper part will be less etched, leading to an almost vertical tip and a widening base. This predicted shape is confirmed from experimental observations (**figure 2-8** to **2-10**).

Finally, it is necessary to go back to the starting presumption and discuss several related phenomena. Firstly, not every collision triggers a reaction. However, the first assumption will still likely to lead to the right conclusion because for a given reaction the total amount of effective collision is proportional to the amount of collision given by Arrhenius equation [46]:

$$k = N_C e^{-\frac{E_a}{k_B T}} \quad , \tag{2-14}$$

where k is the rate constant, N_c is the total number of collision, E_a is the activation energy of a reaction, T is temperature, and k_B is Boltzmann constant. In the second as-

sumption, the parallel fraction of the ion kinetic energy ($R_0 \cdot \sin\theta$) is neglected. However, in reality, this fraction will accumulate and etch a "trench" [5, 38] at the bottom of the wires and widening the bottom of the wires, as are always seen in **figure 2-8** to **2-10**. When only one wire is considered this force will widen the trench, making the wire longer and the base of the wire wider at the same time (**figure 2-13 b**). This effect is clearly seen in **figure 2-9** and **2-10**. The bottom widths of the two wires become 475 and 308 nm, respectively. Both of the widths are larger than the original mask size. However, if two wires are closely located the situation will change, as is shown in **figure 2-12 (c)**. The ions reflected by the slope will counteract with each other. As a result, the wire elongation via trench deepening is curbed. Also, if this situation happens, the etching rate will slow down to $R_0 \cdot \cos\theta$ **(equation 2-11)** because of the sidewall effect shown by **figure 2-12 (d)**. This explains the slower than expected etching rate measured in **figure 2-7**.

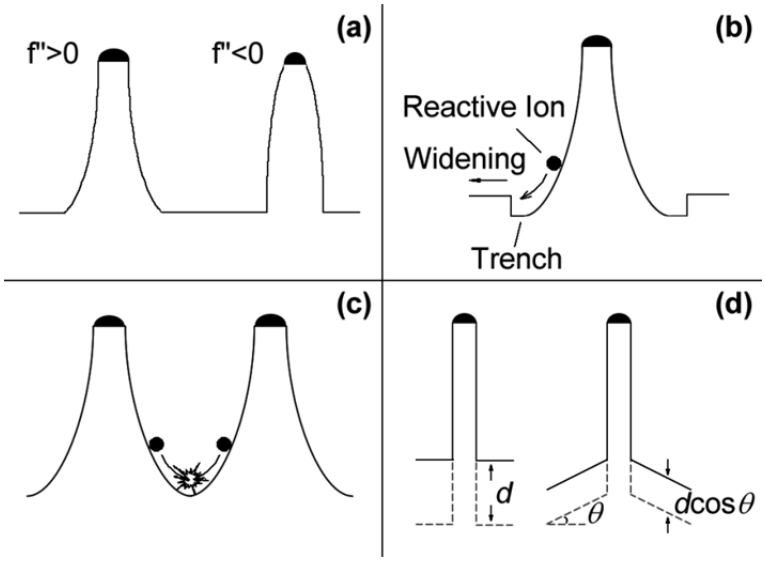

Figure 2-12: Schematic drawings: (a) illustration of two kind of sidewalls, with different curvatures *f''*; (b) the formation of the trench and the trench widening effect; reactive ions colliding with the tilted sidewall will slip down with a horizontal kinetic energy fraction, and this energy forms the trench; (c) if two wires are close to each other, the ions reflected by the sidewall may collide and the kinetic energy is cancelled out; (d) wires with widening bottom will be etched slower as shown in **equation 2-10**.

2.3 Surface Enlargement Optimization

2.3.1 Estimation of Surface Enlargement

After all the discussion above, we know that the estimation in **section 2.1.1** is overestimated in three aspects. First of all, the supposed closed pack of wires cannot be achieved. As is calculated previously, the Ti particles have an average size of 52.3 nm with a density of 1.6×10^{10} cm^{-2}. These data should be used. Secondly, we should always expect conical shape wires. The surface area is then given by:

$$A = D \times \pi r \times \sqrt{L^2 + r^2} \quad , \tag{2-15}$$

where *D* is the wire density, *r* is the wire diameter and *L* is the length of wires. According to the experimental data, *L* is ~ 300 nm. The total surface area can be estimated to be 11.8 times of a planar surface.

From **equation 2-14**, either raise the density of wires or improving the wide wall straightness is helpful for enhancing the surface area. However, controllability of particle distribution via thermal dewetting is poor. As is shown by **figure 2-2**, the dewetting is very sensitive to the thickness of the film, and it failed at 4 nm of Ti. On the other hand, micrometer-long wires are only fabricated with thick masks fabricated via photolithography. With small particle masks of ~ 50 nm diameter, further elongation of wires is not yet achieved. Therefore, the key to enhance the total surface area is to increase the density of wires. Here, a convenient in situ method will be introduced.

2.3.2 In situ Wire Density Multiplication via Mask Redeposition

Enlightened by the high density of secondary wires in **figure 2-8**, the sputtering is intentionally used to achieve a high wire density. Instead of the mild etching conditions which will protect the metal mask, an intensive etching parameter set was used, i.e. 1200 W ICP power and 300 W HF power. In this way, an enhanced mask redeposition is expected. Also, even if the original mask redeposits, the high anisotropy brought by the more intensive etching parameters still leads to a higher aspect ratio of individual wires. According to **equation 2-2**, a high density of wires together with a high aspect ratio will provide an optimized surface enlargement.

As is shown in **figure 2-13 (a) and (d)**, the metal particles disappear during the very first minute of etching, and the mask will redeposit in the nearby, leading to the growth of numerous secondary thin wires around the original masks. After 3 min etching, the original masks are completely redistributed and from the morphology of the wires no trace of the metal masks can be found (**figure 2-13 c and f**). The evolution of particle size and density are listed in **table 2-3**. During the etching, the density of wires increases in situ from 1.8×10^{10} to 4.0×10^{10} cm^{-2}, confirming the effectiveness of in situ density enhancement.

Time (min)	Size (nm)	Density (cm^{-2})
1	37.6±4.6	1.8×10^{10}
2	27.4±3.4	2.5×10^{10}
3	20.5±2.5	4.0×10^{10}

Table 2-3: Size and density calculated from Fourier transformation of SEM pictures (insets of **figure 2-13**); the size (wire diameter) decrease and density increase as a result of in situ mask redeposition and secondary wire formation.

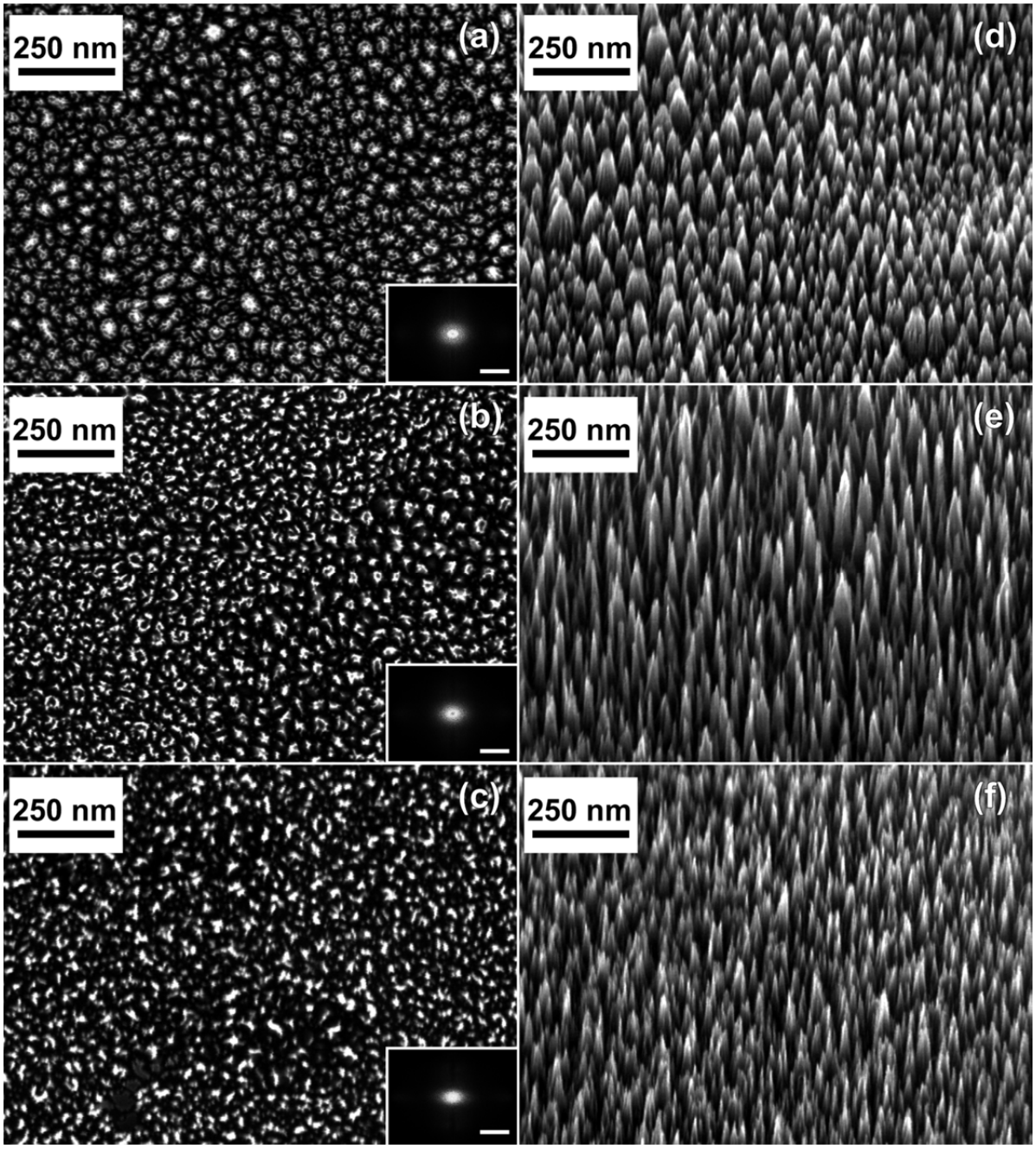

Figure 2-13: Top (a, b, c) and side (c, d, e) views of diamond nanowires fabricated under 1200 W ICP power 300 HF power and 3 Pa at 1 min (a, b), 2 min (c, d), and 3 min (e, f); insets show the Fourier transformation of corresponding images, scale bars: 100 μm^{-1}.

2.3.3 Surface Enlargement Measurement

A typical comparison between a nanowire sample and a planar diamond sample is shown in **figure 2-14 (a)**. The surface enlargements are shown in **figure 2-14 (b)**. From the results it is observed that mild etching condition (700 W ICP power, 100 W HF power, O_2 Pressure 1.3 Pa) gives 10 times surface enlargement, which is in accordance with the calculation in **equation 2-15**. However, this surface enhancement value is ~ 50% lower in comparison to redeposition enhanced etching parameters (1200 W

ICP power, 300 W HF power, O_2 Pressure 3 Pa). With these parameters the highest surface enlargement reaches 20 times, which is in accordance with the previous discussion on the aspect ratio and the help from particle splitting/redeposition. For the samples fabricated with intensive etching condition, the surface enhances almost linearly with etching time for the first two minutes, and then slows down for longer etching durations. Because of the complex nature of the actually etching process, this phenomenon can only be discussed quite qualitatively. It is believed that during the first 2 min, the redeposition is the main behavior of the metal particles. Therefore, the surface area enhances with re-deposited particles as masks. However, with longer etching time, the re-deposited parts start to vanish, and the surface enlargement slows down, and stops when there is no mask left.

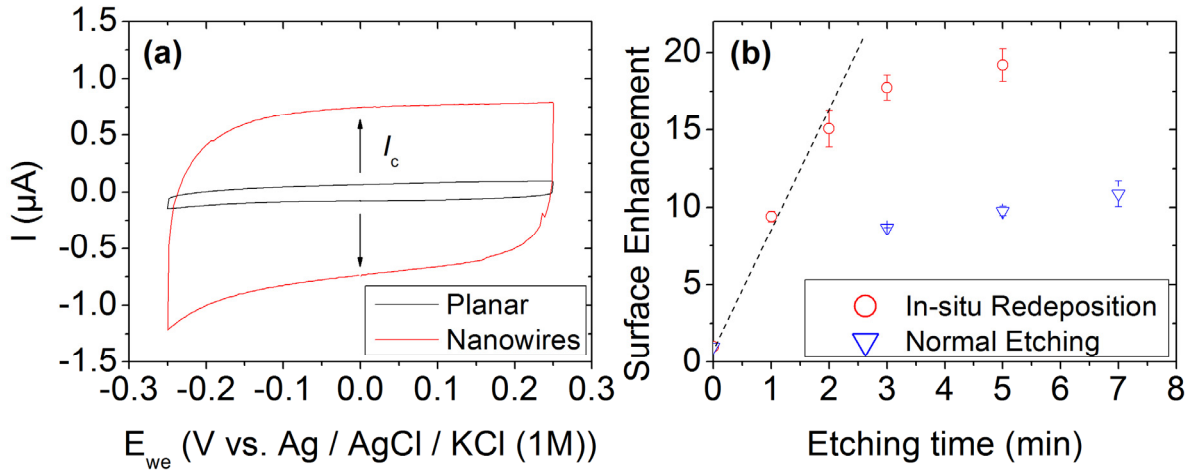

Figure 2-14: (a) Surface enlargement measured from cyclic voltammetry, showing enlarged capacitive current compared to a planar diamond electrode; (b) summary of surface enlargements for nanowires fabricated with and without in situ mask redeposition.

2.4 Summary and Conclusion

In this chapter different etching conditions are investigated, and the surface enlargement factors are measured. The results are analyzed both experimentally and theoretically. Compared with the already abundant results in literature, this chapter describes non-ideal etching effects such as isotropic etching and mask shrinking. Via in situ mask redeposition, a high surface area is achieved. The surface enlargement is improved from state of the art 10 times [6] to 20 times.

However, even with these improvements, a surface enlargement of 20 times is still insufficient for practical electrochemical energy storage. Compared to the state of art double layer micro-supercapacitors [47], the capacitance should reach at least 1 mF/cm^2 (or ~ 100 times surface enlargement). Moreover, this specific capacitance is not scalable, i.e. one cannot multiply it by making the wire infinitely long. However, for traditional sp^2 carbon, it is easy to do so by adding a thicker layer of active material to enhance the specific capacitance per cm^2.

Therefore, although diamond nanowires electrode has proved a successful platform for catalysts [48] and sensors [9], it cannot enlarge the diamond surface to be comparable to state of the art technology based on activated carbon. A new concept to enlarge the diamond surface is therefore needed.

Chapter 3: Diamond-Coated Wires and Diamond Foam

As discussed in the last chapter, diamond nanostructures from top-down etching methods fail to provide large surface areas for high capacitance requirements. In addition, top-down etching methods on bulk diamond waste large quantities of diamond. Therefore, bottom-up growth, or templated-growth, will be investigated as an alternative approach in this chapter. Two kinds of templates, i.e. silicon nanowires and silica spheres, will be applied as growth templates.

3.1 Diamond-Coated Silicon Wires

3.1.1 Silicon Nanowires

Templated-growth methods are widely applied for the creation of uniform porous structures with a large variety of morphologies [49]. In this method functional materials, like activated carbon [50-53] or metal-oxides [54], are synthesized within a matrix of porous templates, typically silica [51], zeolite [50], polymer [52], and biomaterials [53]. These templates are then selectively removed after growth. The porosity of the resulting material will be inherited from the porous template. Therefore, templated growth techniques are typically used to fabricate surface enlarged materials.

Template growth has also been applied for the growth of surface-enlarged diamond. silicon nanowires have been used as a growth template. These diamond-coated wires have been reported to be applied in field emission [23, 24] and sensor applications [16]. However, the growth on other templates is seldom reported. There are several possible reasons for the lack of references. Firstly, CVD diamond growth takes place at high temperatures (typically 500 – 1200 °C [55]). Therefore, organic based templates can hardly be used. Secondly, CVD methods require that reactive species can diffuse to the site where they should be deposited. As a result, the template cannot have too small pore size (like zeolite). Thirdly, hydrogen rich plasma will etch sp^2-carbon [56]. Therefore, activated carbon-based materials cannot be applied as templates. On the other hand, silicon has been used as a conventional substrate for diamond growth [55]. Its carbide formation provides good adhesion between the sample and substrate; comparing to other materials it has a low thermal expansion (~ 3×10^{-6} K^{-1} at 298 K) [57]; also, its melting temperature is sufficiently high (~ 1700 K). Besides all these advantages, the fabrication techniques for silicon nanowires have been extensively investigated [58]. Therefore, silicon nanowires are promising for bottom-up diamond overgrowth technologies.

For the fabrication of Si nanowires there are top-down and bottom-up approaches. The application of the top-down method is based on the processing of silicon wafers by dry etching using a shadow mask [59] (similar to the fabrication of diamond nan-

owires as discussed in **chapter 2**); alternatively, wet-chemical etching with $AgNO_3$/HF [60-63] can be applied by the following chemical reaction:

$$\mathrm{Si}(s) + 4\mathrm{Ag}^+ + 6\mathrm{HF} \rightarrow 4\mathrm{Ag}(s) + \mathrm{H_2SiF_6} + 4\mathrm{H}^+ \quad , \tag{3-1}$$

The silver particles generated by this reaction will be deposited on the silicon substrate and act as anode. Under the silver particles silicon will be oxidized and dissolved subsequently by HF. The silver particles then etch into Si leaving textured structures which ultimately become wires.

In the bottom-up growth or the vapor-liquid-solid (VLS) method [64, 65], catalyst (like Au) particles are formed on a silicon substrate by lithography or self-assembly. During deposition these particles are heated above the Au-Si eutectic point under silicon precursor atmosphere. Then the Au droplets become oversaturated with Si atoms, and nanowires of Si grow under the catalyst particles.

In this work, silicon nanowire samples were grown at CEA France with the VLS method. With this method, the doping and morphologies can be adjusted [66-68]. The wires are p^{++} doped with $N_A = 4\times10^{19}$ cm^{-3} [69]. The nanowires show typical diameters of 50 – 100 nm and lengths of up to 30 µm. The density of the nanowires is estimated by counting the number of gold particles per cm^2 using SEM images, which results in a density about 3×10^8 cm^{-2} [67].

3.1.2 Diamond Growth on Silicon Wires

The diamond growth follows conventional "seeding-overgrowth" approaches [70]. The intrinsic oxide layer on the silicon surface provides a negative dipole. H-terminated nanodiamond seeds with a positive dipole can then self-assemble on such a surface forming a dense seeding layer [70]. The subsequent overgrowth of diamond was performed using a microwave chemical vapor deposition (MWCVD) system and hydrogen/methane gas mixtures. To realize boron doping trimethylborane was added to the H_2/CH_4 mixture. The growth parameters are listed in **table 3-1**. The overgrowth duration was 100 min which resulted in a film thickness of 240 nm as measured on a planar reference sample.

Parameter	Values
Methane (% in H_2 mixture)	4
Microwave Power (W)	2750
Gas Pressure (mbar)	40
Temperature (°C)	675±10
[B]/[C] ratio	4000 ppm

Table 3-1: Summary of growth parameters for the diamond coating of silicon nanowires.

After overgrowth, the samples were cleaned wet-chemically in a mixture of H_2SO_4 and HNO_3 in a 3:1 ratio and boiled for 1.5 hours at 250 ℃ to remove hydrocarbon residues.

Then the electrodes were rinsed in deionized water (DI) and methanol before being blown dry under N_2 atmosphere.

Figure 3-1 shows SEM images of a) the bare Si NWs, b) the seeded sample, c) the sample after diamond overgrowth and d) an overview of the diamond-coated silicon wire (DiaSiW) sample. After seeding, nanodiamond seeds can be detected to cover the entire sample surface homogenously. The seeding density is close to 10^{11} cm^{-2} which is similar to previous results [56]. Most importantly, the seeds are distributed on the substrate as well as on the wires (**figure 3-1 b**). After overgrowth, the diameter of the wires was enlarged from to 50 nm to approximately 200 nm (**figure 3-1 c**).

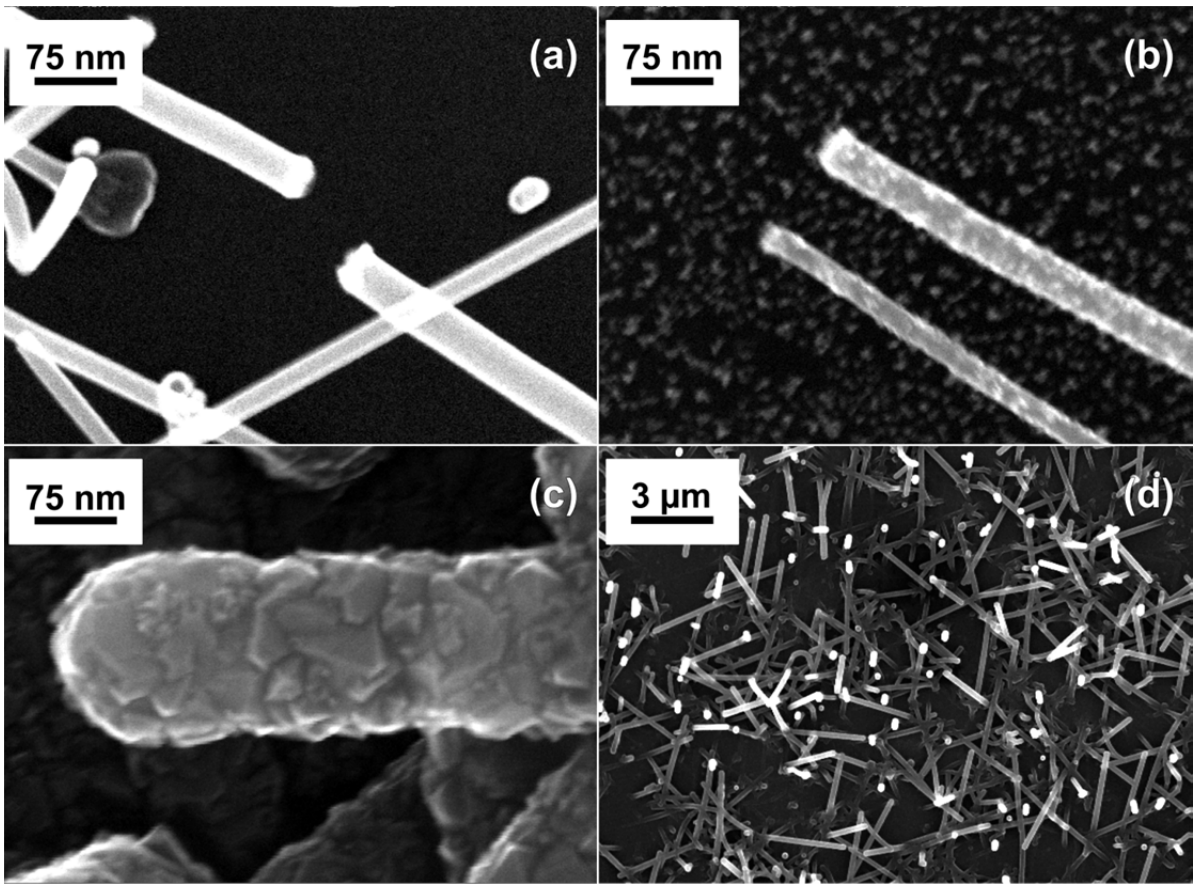

Figure 3-1: SEM images of (a) bare silicon nanowire, (b) silicon nanowire after seeding process, (c) diamond-coated silicon wires, (d) a large scale picture of (c) showing the density and uniformity.

Raman spectroscopy is used to detect the quality of diamond and to estimate the dopant density in the wavenumber range from 526 to 2100 cm^{-1} at an excitation wavelength of 457.94 nm using an Ar^+ laser. **Figure 3-2 (a)** shows Raman spectra of DiaSiW as compared to intrinsic single crystalline diamond. A clear diamond Raman peak is detected at 1301 cm^{-1} in DiaSiW compared to 1332 cm^{-1} in intrinsic single crystalline diamond [71]; the peak around 1150 cm^{-1} is related to the trans-polyacetylene in the grain boundaries; the peak around 1350 cm^{-1} and the broad band between 1400 and 1600 cm^{-1} are attributed to amorphous/graphitic carbon (D and G bands) [71, 72]. The

non-diamond content (trans-polyacetylene, D, and G bands) are likely from grain boundaries and is typical for NCDs because of the high proportion of grain boundaries [73]. The shift of the first order diamond Raman peak is attributed to the Fano resonance which is a result of an interference between a continuum of electronic states generated by the acceptor atoms and the discrete zone-center phonons [74]. This shift shows a logarithmic dependence on the boron concentration [70]. Therefore, the boron concentration for our sample can be calculated to be about 4×10^{21} cm^{-3}, leading to metallic conductivity at room temperature [75]. Therefore, the DiaSiW sample is suitable for electrochemical applications.

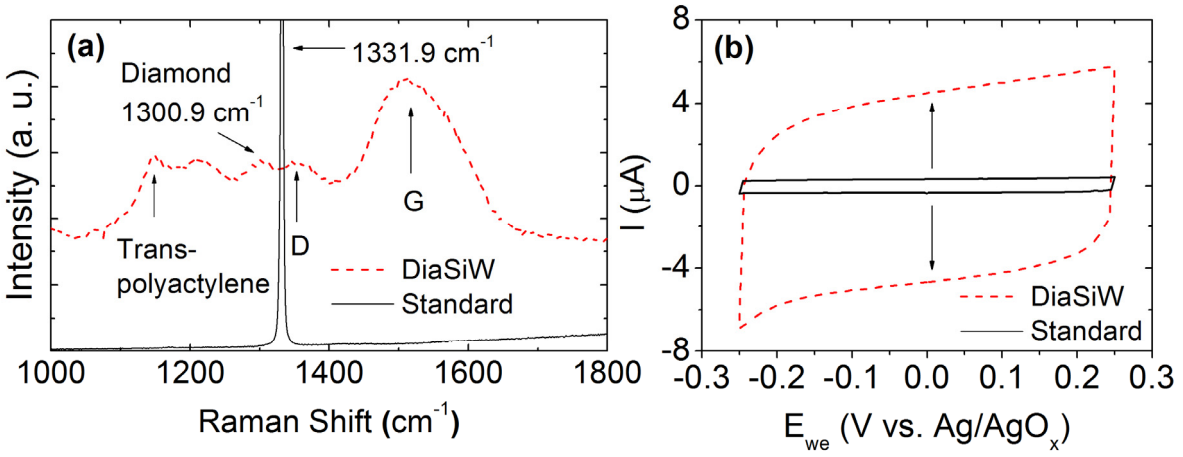

Figure 3-2: (a) Raman spectra between 1000 and 1800 cm^{-1} at an excitation wavelength of 457.94 nm of DiaSiW in comparison to an intrinsic single crystalline diamond; (b) CV comparison between a DiaSiW sample and a planar boron-doped diamond planar electrode between −0.25 and 0.25 V in 40 vol% PMPyrrBTA in PC (scan rate 100 mV/s), demonstrating a capacitive current enhancement.

The surface area can be measured using capacitive current measurements in cyclic voltammetry. We applied a scan rate of 100 mV/s in an ionic liquid solution (40% PMPyrrTFSI in PC). The capacitive current is proportional to the surface area exposed to the electrolyte solution by [6]:

$$I_C = C_n A v \qquad (3\text{-}2)$$

where I_c is the capacitive current from the charging of the interfacial capacitance C_n (F/cm^2); v is the scan rate and A the electrode surface area. As shown in **figure 3-2 (b),** the capacitive current is about 13 times larger than measured on a planar boron-doped polycrystalline diamond electrode, with a capacitance value of 110 µF/cm^2.

The surface enlargement of DiaSiW electrodes is dependent on the density and geometry of Si wires by:

$$F_{SE} = \pi d l \times D_w \quad , \qquad (4\text{-}3)$$

where d and l are the average diameter and length of the wires, respectively; and πdl gives the sidewall area of each wire; D_w is the density of the wires. By increasing the

wire length and density, a higher surface enlargement can be expected [68]. Among all the samples we received from French partners, the samples showing the best capacitance are the samples with ~ 15 μm Si wires, with the catalyst Au particles deposited via thermal dewetting of a 4 nm Au film. After coated with diamond, these samples show capacitance values of around 1.3 mF/cm^2 (or 150 times surface enlargement). Evaluated from **equation 4-3**, the density of the wires is calculated in the level of 1×10^{10} cm^{-2}. **Figure 4-3** shows the SEM images of these samples. Although the length and density are much higher than the sample shown in **figure 4-1**, the diamond coating still manages to cover the surface completely. In fact, in another attempt (not shown here), 27 μm long silicon nanowires with 100 nm diameter are successfully coating by nanocrystalline diamond. In the last chapter, the aspect ratio of the wires is limited to ~ 30 by the etching selectivity between the metal and diamond (**table 2-1**). With templated growth method, however, the aspect ratio can reach ~ 300. Limited by the number of samples provided by our French partner, the largest aspect ratios which can be coated with diamond have not been ascertained. However, there is a clear indication that CVD diamond is capable of coating vertical structures with high aspect ratio.

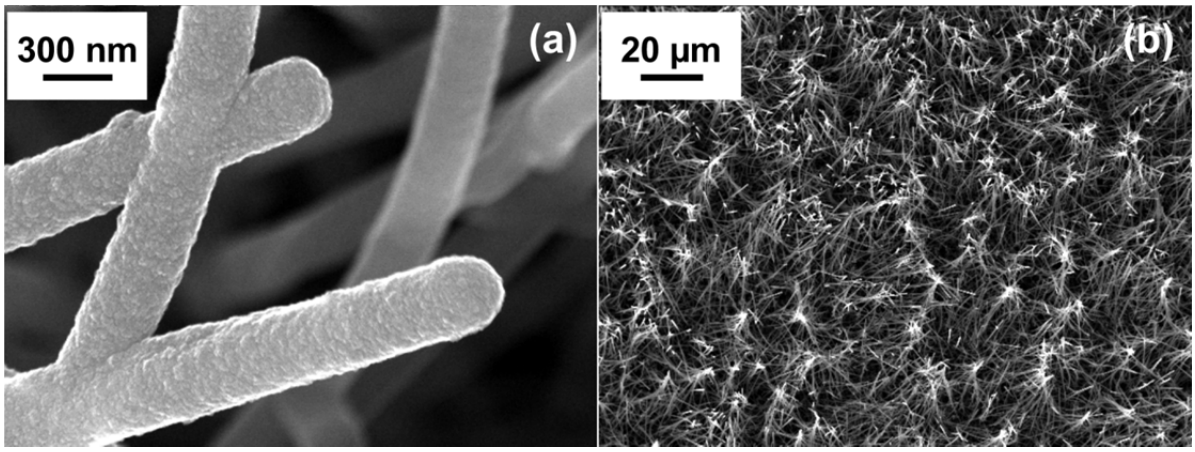

Figure 4-3: SEM images of diamond coated silicon wires with 15 μm long at different magnifications. The Au particles were deposited via thermal dewetting of a 4 nm film; the density of wires estimated from surface enlargement is ~ 10^{10} cm^{-2}.

3.2 Diamond Foam

3.2.1 General Considerations

Monodispersed silica spheres have been successful synthesized since 50 years by means of hydrolysis of alkyl silicates and subsequent condensation of silicic acid in alcoholic solutions [76]. They are commercially available in different sizes and have been widely used as easily removable templates for the fabrication of porous materials [51, 77-79]. The insertion of spherical template creates "bubbles" in the material, making it comparable to "foam".

However, there is no previous report about diamond growth on such templates. The reason is that for CVD there is no easy way of template-growth. Normally, in the growth of porous sp^2 carbon materials, the liquid precursor can be uniformly mixed with the template materials (beads, fibers, etc.) before carbonization (**figure 3-4 a**). However, CVD growth, the reactive radicals in the gas phase suffer from a diffusion limitation [80, 81]. For instance, in the case of diamond growth, both atomic hydrogen and hydrocarbon radicals are important to trigger the diamond growth. The chemical reactions involved in the growth of diamond can be described as follows:

$$C_D H + H^{\cdot} \leftrightarrow C_D^{\cdot} + H_2 \qquad (3\text{-}4)$$

$$C_D^{\cdot} + CH_3^{\cdot} \leftrightarrow C_D CH_3 \qquad (3\text{-}5)$$

Reaction 3-4 represents the activation of a surface hydrogen vacancy site by removal of a hydrogen atom from an H-terminated diamond surface carbon ($C_D H$). This site is then activated for the addition of hydrocarbon radicals (e.g. $CH_3^{\cdot}$), shown in **reaction 3-5**.

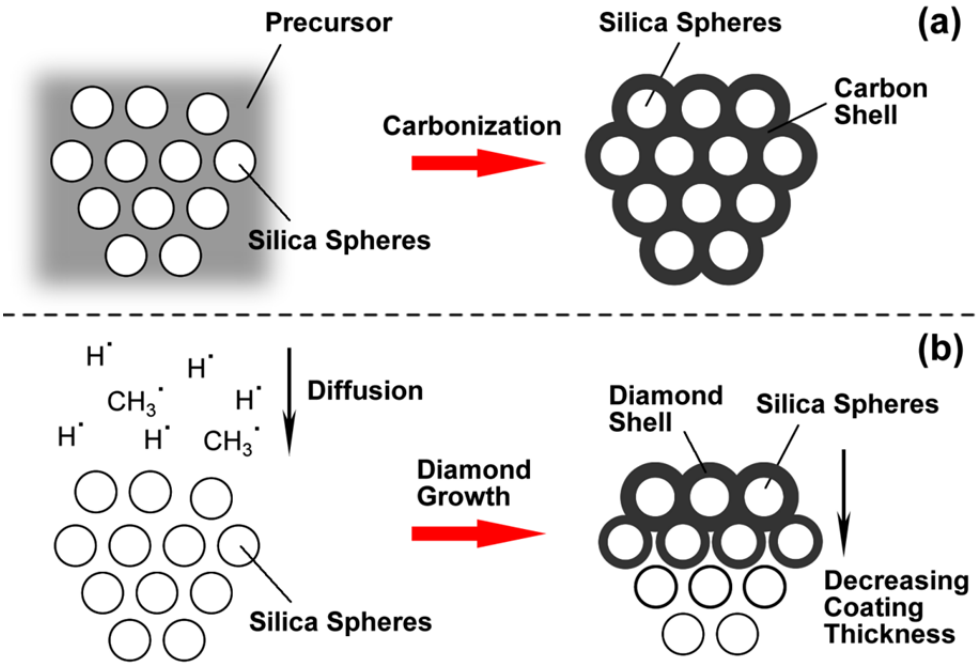

Figure 3-4: Schematic illustrations showing the difference between templated-growth of porous sp^2 carbon (a) and the template-growth of diamond (b).

In the templated diamond growth, however, the diffusion of reactive species into the complex 3D porous structures is hindered. When reactive radicals collide with the template they lose the kinetic energy which is necessary to trigger **reaction 3-4** and **3-5**. Therefore, most radicals can only reach the upper part of the template, and the amount of diamond deposited decreases with the increasing depth into the template (**figure 3-4 b**).

3.2.2 Optimization of Fabrication Method

To analyze this diffusion problem mathematically, Fick's second law of diffusion is applied. For the diffusion of a certain species into a medium, the time-dependent concentration distribution $N(x, t)$ follows:

$$\frac{\partial N}{\partial t} = D\frac{\partial^2 N}{\partial x^2} \quad , \tag{3-6}$$

where N is the concentration of the species, D the is diffusion coefficient, t is the time, and x the distance from the surface. Because the amount of reactive species in the plasma is constant during the growth, we can regard this diffusion problem as a constant-surface-source diffusion. The solution to **equation 3-6** is given by:

$$N(x,t) = N_0 erfc(\frac{x}{2\sqrt{Dt}}) \quad , \tag{3-7}$$

where *erfc* is the complementary error function. The schematic plot of the solution is shown in **figure 3-5**. As the distance away from the surface increases, the concentration of the reactive species decreases. Therefore, one solution to this problem is to minimize x by using only one layer of silica particles. We need to notice that the concentration difference between the surface and a certain point inside the medium is lowered by a longer diffusion time (larger t) and a lower surface concentration (smaller N_0). Therefore, a low methane concentration and slow growth over longer time is a potential solution to CVD diamond growth on 3D templates.

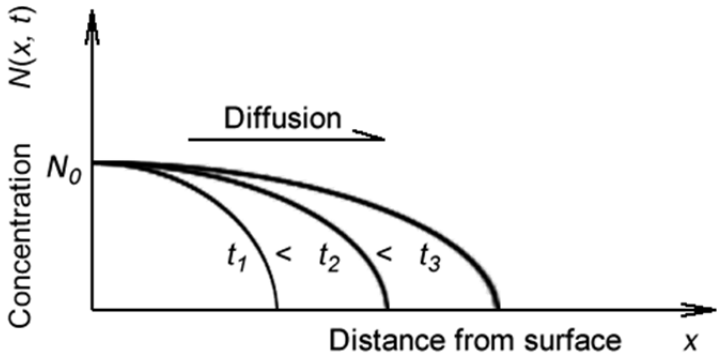

Figure 3-5: Schematic illustration of the concentration profile with a constant surface source; t_1, t_2 and t_3 show the concentration profiles at different time.

Figure 3-6 (a) shows the growth of diamond on three layers of silica spheres. It can be observed that only the first layer is fully covered by diamond and the second layer is only covered by half; the third layer, however, is not covered by diamond. Therefore, only a monolayer of spheres should be used as template for diamond deposition and then this process is repeated to accumulate a thick layer.

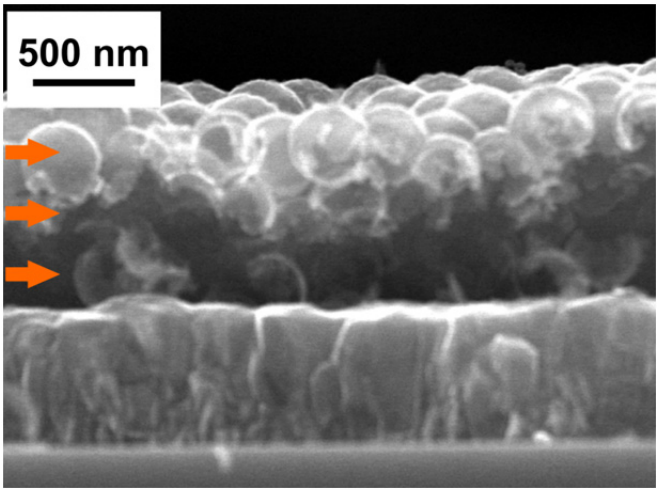

Figure 3-6: SEM images showing the inhomogeneous diamond coverage on a three-layer silica sphere template (after template removal). The diamond coverage decreases as the distance from the top increases.

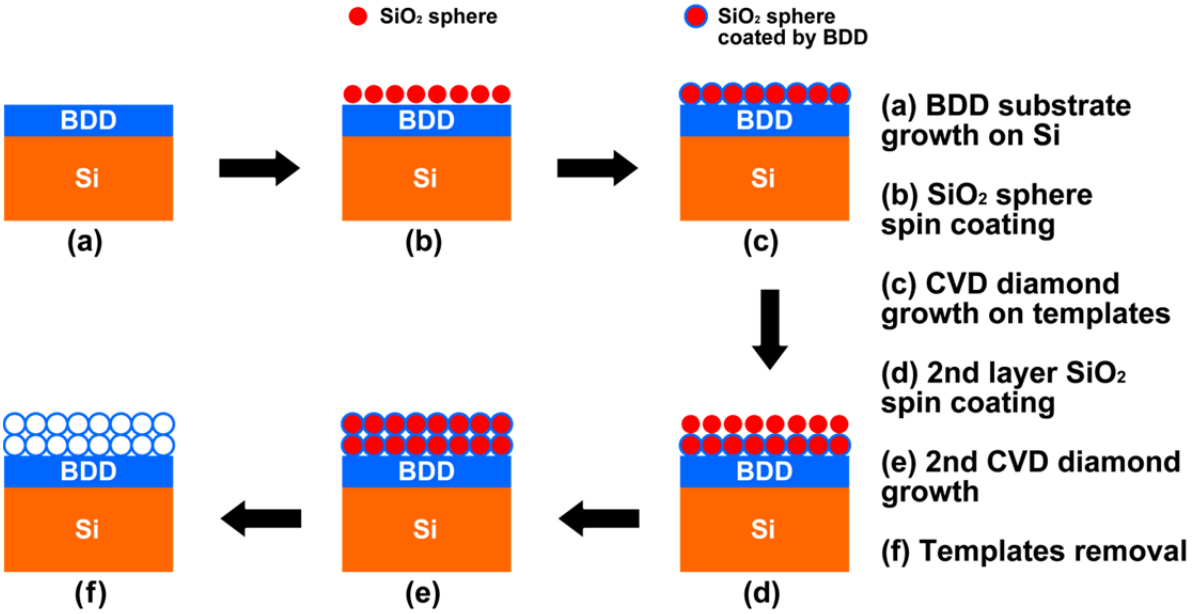

Figure 3-7: Schematic illustrations showing the procedures for diamond foam growth.

Therefore, the growth of diamond foam is designed as drawn in **figure 3-7**. Each diamond foam sample is composed of 3 layers [17]. The first layer from bottom is a Si (100) substrate on which a heavily boron-doped diamond current-collecting layer is grown. The diamond foam layer is then deposited on top.

To achieve large surface enlargement, a close-packed monolayer of SiO_2 particles will be preferred as template for the following diamond growth. In order to enhance the uniformity of the particle and improve the reproducibility of the method, low-speed spin coating is used to disperse the particles on the surface. 0.5 mL isopropanol suspension containing 50 mg/mL silica particles is coated onto the wafer at 300 rpm. The dependency of the sphere density on the sphere diameter is investigated and shown in

figure 3-8. For a sphere diameter of 0.5 µm, a uniform coverage is achieved (**figure 3-8 a**) with a density of 4.7×10^{8} cm^{-2} which is close to a theoretical monolayer (**figure 3-8 d**). When the diameter increases to 1.5 and 3.0 µm, however, the density decreases to less than 50% of a monolayer. During spin coating, the centrifugal forces for larger particles are also larger, resulting in a decreasing amount of remaining spheres. Therefore, particles with a diameter of 0.5 µm are chosen to form the template.

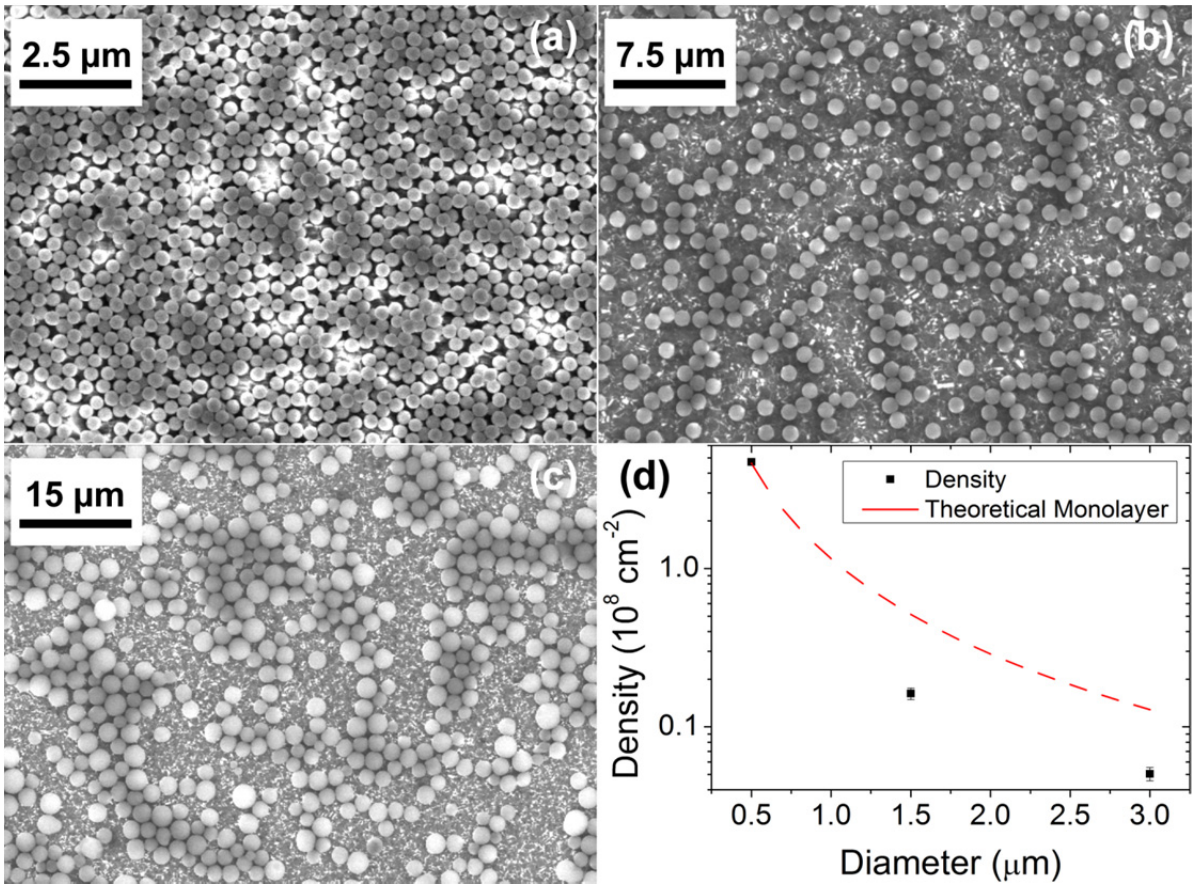

Figure 3-8: SEM images of SiO_2 sphere layers deposited via spin coating with diameters of 0.5 µm (a), 1.5 µm (b), and 3 µm (c); (d) statistics of the density of spheres; the red dashed line shows the theoretical density of a close packed monolayer.

The next question concerns the substrate for the growth. While silicon is a good substrate for diamond growth, it is not a satisfactory substrate for diamond foam fabrication. Foam samples grown on silicon samples easily collapse during acid cleaning, showing weak adhesion between foam and Si (**figure 3-9 a**). A schematic visualization of the situation is depicted in **figure 3-9 (b)**. The diamond growth at the base of the foam spheres is limited by the Si substrate. In the case of a diamond substrate, as the diamond sphere shell grows, so does the substrate, stabilizing the base of the shell. As a result, when the foam is grown on diamond, it is mechanically more robust than when it is grown on a Si substrate.

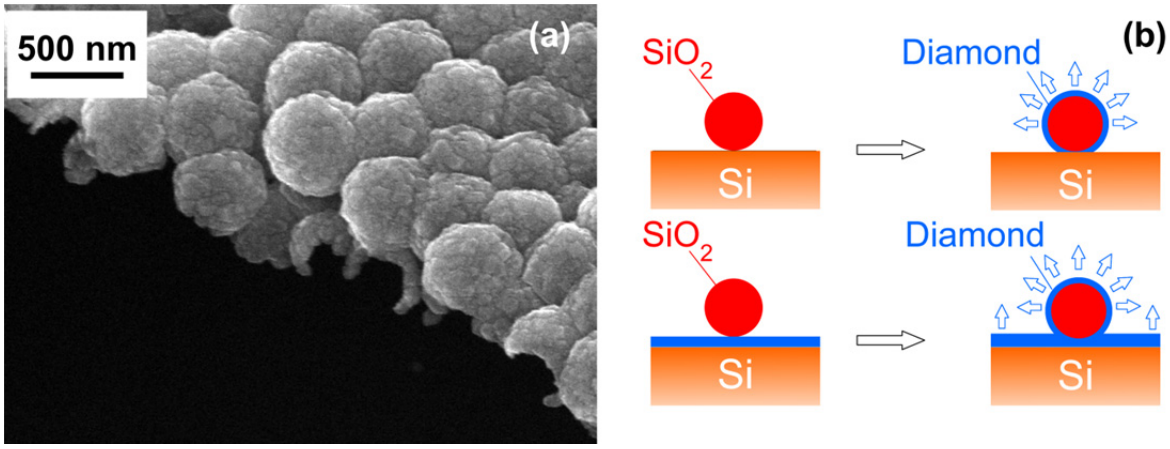

Figure 3-9: (a) A fraction of foam which was grown on a Si substrate but peeled off after acid cleaning; (b) mechanism explaining the enhanced adhesion for foam grown on a diamond-coated Si surface.

The 3-inch boron-doped polycrystalline diamond substrate for diamond foam is synthesized with our microwave CVD system on Si (100) substrate. The basal diamond synthesis uses standard electrochemistry grade diamond CVD parameters (**table 3-2**). The growth parameters are chosen after the following considerations: 1) the growth rate should be low so that the interstitial space between SiO_2 spheres will not be closed before a complete diamond shell forms. Therefore, the methane concentration and temperature should be low to slow the growth rate. In addition, a low methane concentration would enhance the diamond quality. 2) In order to metallically dope diamond, a sufficiently high boron concentration should be added. Based on the results from Hees [70], the growth parameters are chosen as listed in **table 3-2**.

Parameter	Basal Diamond	Diamond Foam
Methane (% in H_2 mixture)	2	1
Microwave Power (W)	3200	2200
Gas Pressure (mbar)	50	40
Temperature (°C)	750±10	650±10
[B]/[C] ratio	4000 ppm	12000 ppm

Table 3-2: Summary of the growth parameters for the diamond foam and the underlying diamond film on top of the Si substrate.

As is stated in the first chapter, diamond is much more expensive than activated carbon. Therefore, the amount of diamond needed should be minimized, and in order to achieve a thin diamond film, a high initial seeding density should be achieved [70]. The standard seeding procedure for polycrystalline diamond wafer growth includes 5 min ultrasonication in H-terminated diamond seeding solution and a DI-water rinsing afterwards. The rinsing is to remove excessive seeds and agglomerates. This method is however not suitable for the growth of foam, because the ultrasonication will remove all the silica particles. Therefore, dip-coating is used instead. **Figure 3-10** shows results from a short overgrowth (0.5 h) of two samples seeded by dip-coating. The sample (a) was rinsed with DI water while the sample (b) is not rinsed after one dip in the dia-

mond seeding solution. Both samples were dried in a fume-hood without further treatment. After the overgrowth, the sample (a) had not reached a closed film, while in sample (b) a closed film is already formed. From this result, we can see that although the rinsing probably removes unwanted agglomerates, it also reduces the seeding density. For the growth of an ultrathin shell of diamond, a rinsing is not helpful.

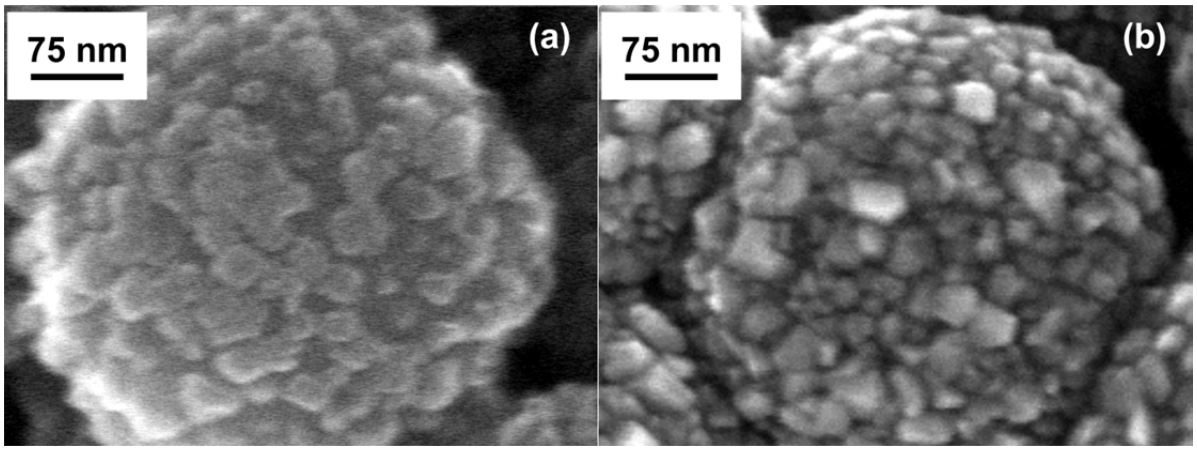

Figure 3-10: Diamond overgrowth on silica spheres with different seeding methods: (a) with and (b) without DI water rinsing after seeding; overgrowth time 0.4 h.

Because double layer capacitance is a surface effect, a thick diamond shell will not contribute to the capacitance but will waste material. Therefore, the growth time has to be optimized to find the minimum required growth time. Diamond foam samples are grown for 0.4, 0.7, 1.0 and 1.3 h. SiO_2 spheres are removed by hydrofluoric acid leaving diamond shells. The samples are characterized by SEM (**figure 3-11**). From a short overgrowth of 0.4 h, closed diamond shells have already been formed. None of the samples collapse after removing the templates, indicating that the shells are stably connected. When the growth time increases, the shells become thicker and grains grow larger. However, the total surface area decreases as the inter-sphere space will be filled by diamond.

To investigate the optimized growth time, capacitive current of monolayer foam samples with different growth time are measured according to **equation 2-3**. Since capacitance is an interfacial property, the thickness of diamond shell will not directly affect this value. With geometric relations, the surface enlargement for *N* layers of close-packed hollow spheres is given by:

$$f_{SE} = \frac{4\pi}{\sqrt{3}} N \quad , \tag{3-8}$$

where f_{SE} is the surface enlargement factor. That is to say, each layer of the close-packed hollow spherical shell provides a surface enlargement of 7.26 times. Taking into account the specific capacitance of diamond (~ 8 μF/cm^2), each layer of close-packed hollow diamond spheres provides a capacitance value of 57.5 μF/cm^2.

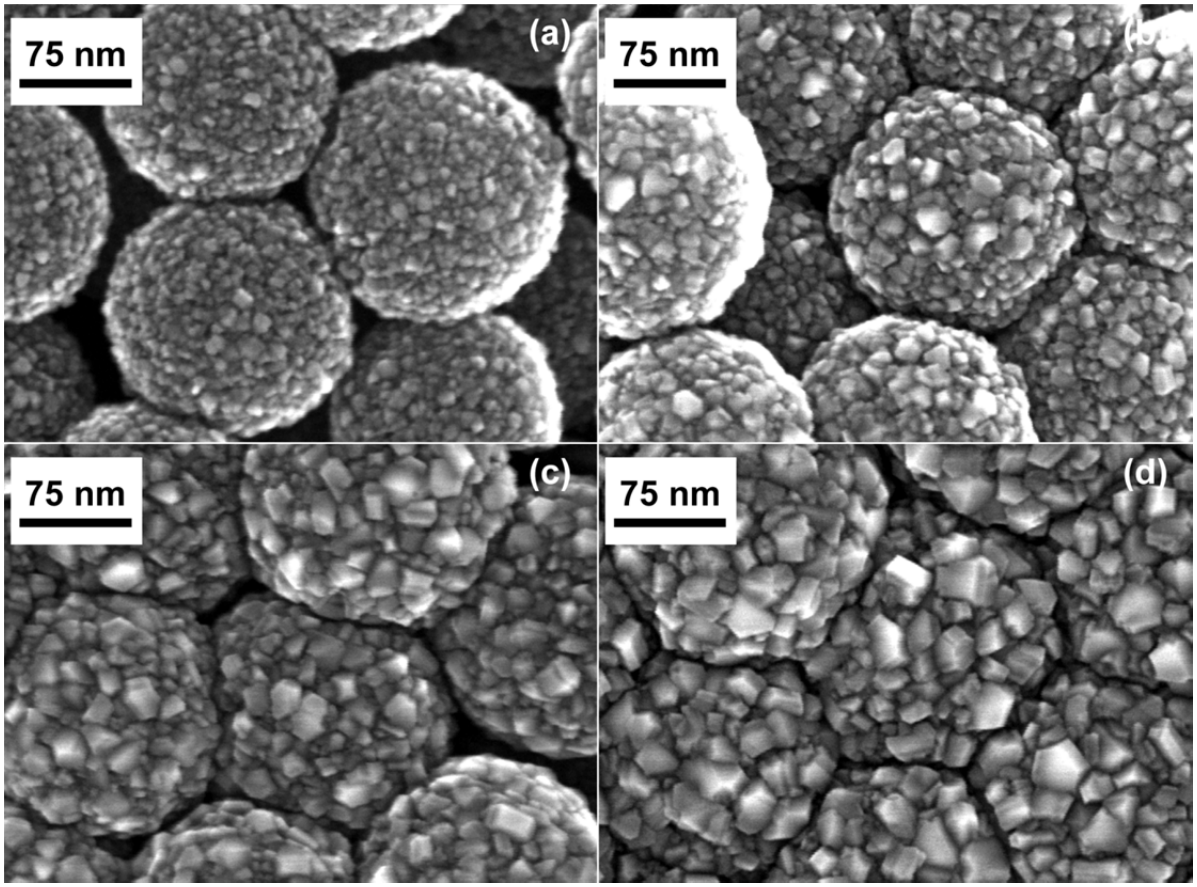

Figure 3-11: SEM images of diamond foam grown for 0.4 h (a), 0.7 h (b), 1.0 h (c) and 1.3 h (d); SiO_2 templates have been removed in these images.

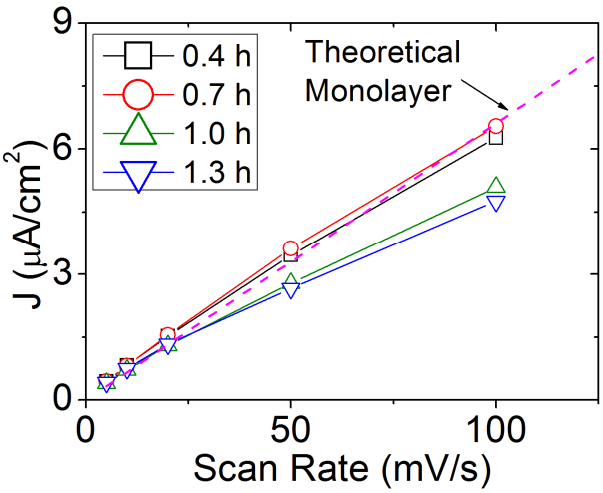

Figure 3-12: Capacitive current vs. scan rate of four monolayer foam samples with different growth time. The dashed line shows the theoretical value of monolayer foam for comparison.

Figure 3-12 shows the capacitive current at a scan rate of 100 mV/s in 0.5 M $NaClO_4$ with different growth time. The capacitive currents of all the samples are close to the theoretical value of a monolayer of hollow diamond spheres. With 75% more growth time, the 0.7 h sample shows only 10% more capacitive current than the 0.4 h sample,

showing the film after 0.4 h growth is already of good quality and further growth is not necessary. The decrease in the capacitive current for 1.0 and 1.3 h sample is the effect of filling the interstitial space between the diamond shells.

3.2.3 Characterization of Diamond Foam

With the above mentioned method, a uniform diamond foam (DF) electrode is obtained (**figure 3-13**). The DF wet-chemical oxidation in 200 °C mixed acid (1:3 HNO_3:H_2SO_4) achieves oxygen termination and thus better wetting for aqueous solutions [82]. The thickness of such a DF sample measured from **figure 3-13 (a)** is ~ 2.6 µm. For the packing of spheres, simple cubic packing has the lowest density, while the densest packing is face-centered cubic. For these two structures, the relationship between the film thickness and number of layers is given by:

$$T_f = [\frac{\sqrt{6}}{3}(N-1)+1]d \tag{3-9}$$

for face-centered cubic, or

$$T_f = Nd \tag{3-10}$$

for simple cubic.

Here, T_f is the film thickness; $N \geq 2$ is the number of layers; d is the diameter of the spheres. For face-centered cubic packing, T_f is the height of the tetrahedral unit composed of four spheres, while for simple cubic packing; T_f is obtained by calculating the height of the cubic unit of four spheres. Because these two situations stand for the two extremes of packing, an experimental thickness of 2.6 µm equals to 5.2 to 6.1 layers. From **equation 3-8**, a six-layer DF will provide 43.5 times surface enlargement.

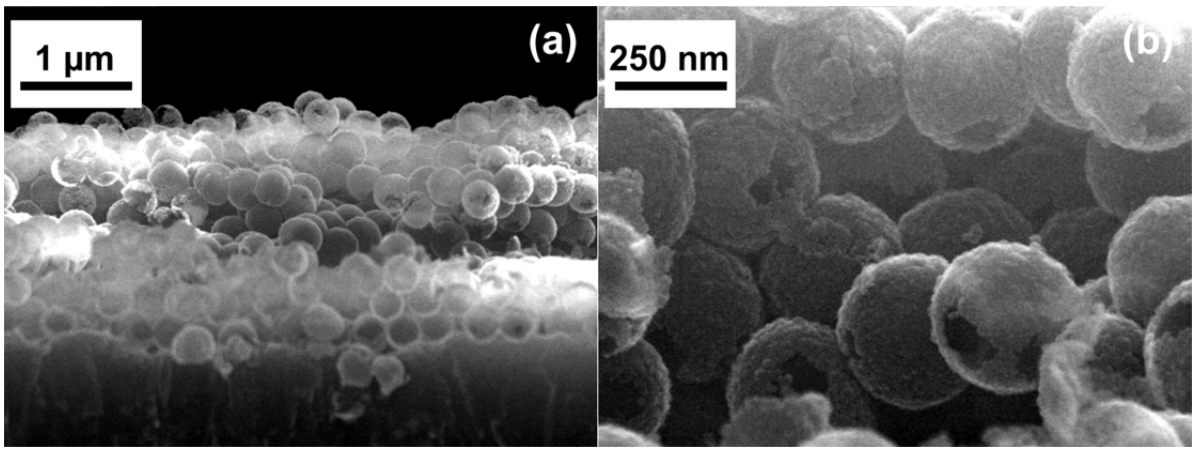

Figure 3-13: Cross-section images of diamond foam at different magnifications.

The diamond quality of the film in terms of non-diamond carbon content is characterized by Raman scattering (**Figure 3-14 a**) [71]. A clear first order diamond peak is detected at 1328 cm^{-1} in DF which shifted 4 cm^{-1} compared to 1332 cm^{-1} in intrinsic sin-

gle crystalline diamond [71] due to Fano resonance [74]; with boron concentrations above 10^{20} cm^{-3}, the first order diamond peak starts to shift to lower wavenumbers [75]. However, this shift is small here. It is only possible to estimate the boron doping to be around 10^{20} cm^{-3}. Some non-diamond carbon incorporation is also seen from the spectrum: the peak around 1150 cm^{-1} and a hump at 1430 cm^{-1} are related to trans-polyacetylene; the shoulder around 1350 cm^{-1} and the broad band between 1400 and 1600 cm^{-1} are attributed to amorphous and graphitic carbon (D and G bands), respectively [71, 72]. These non-diamond carbon is probably located in grain boundaries and is typical for NCDs where the high proportion of grain boundaries are unavoidable [73].

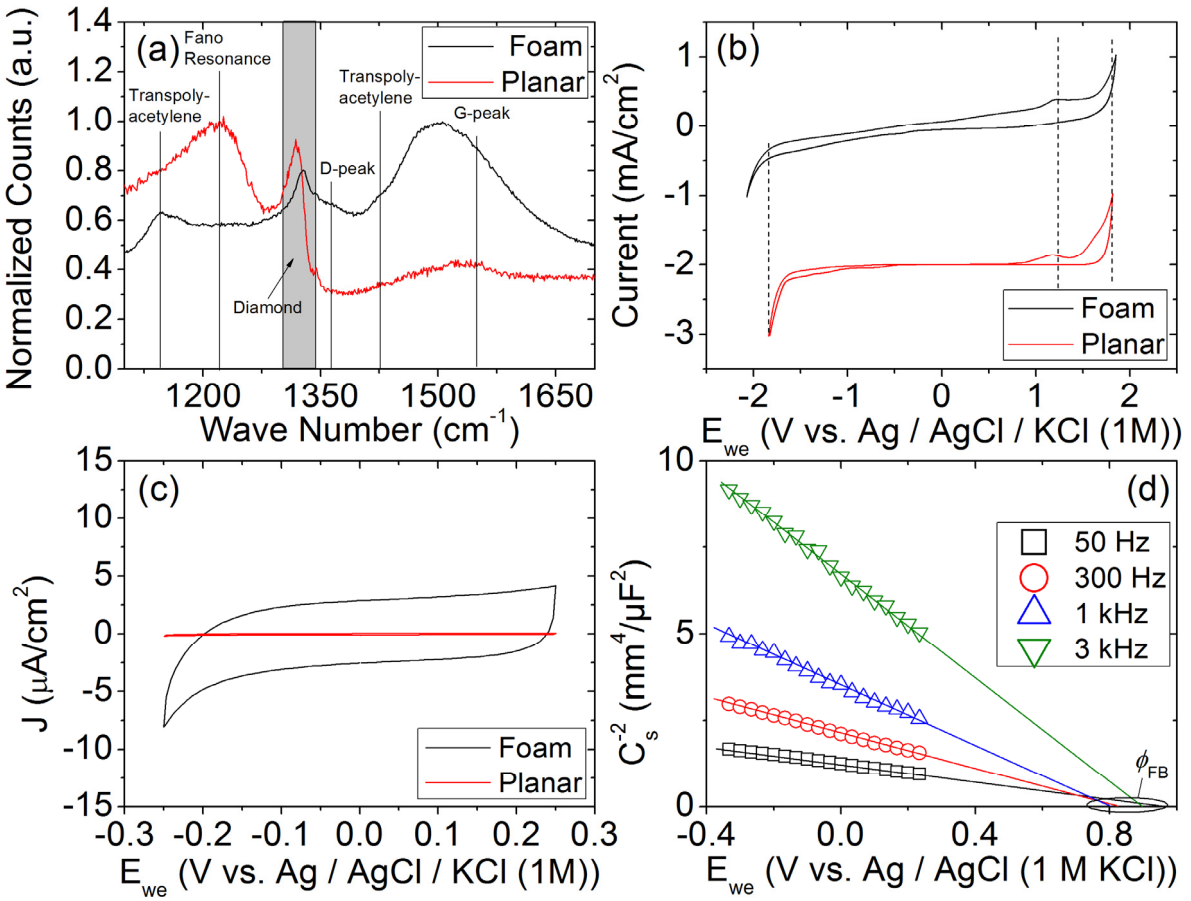

Figure 3-14: (a) Raman spectroscopy between 1000 and 1800 cm^{-1} for a DF sample and the diamond substrate; (b) ECW comparison between a DF electrode and a planar diamond electrode in 3 M $NaClO_4$ at 100 mV/s; (c) background current comparison between a DF electrode and a planar diamond electrode in 3 M $NaClO_4$ at 5 mV/s; (d) Mott-Schottky measurements on diamond foam and linear fittings (Φ_{FB} is the flat band potential) at 50, 300, 1000 and 3000 Hz over potential range of ± 0.5 V in 3 M $NaClO_4$.

The diamond-dominating behavior is also confirmed from electrochemistry measurements. A wide electrochemical window (ECW) of DF is confirmed using cyclic voltammetry and compared with a planar boron-doped diamond electrode shown in **figure 3-14 (b)**. Typical diamond background current profiles are obtained for DF compared to planar samples, showing that the non-diamond carbon is not affecting the electro-

chemical performances of the DF electrode. The diamond surface oxidation peak appears on both samples at 1.2 V showing no potential shift between the two CV curves. Moreover, the ECW of DF is even 0.5 V wider at the hydrogen evolution side, which is likely to be the result of lower doping level (as will be discussed later). In order to estimate the surface enlargement factor of DF electrodes, CV measurements at 5 mV/s were performed on both DF and planar electrodes. Within the range of –0.25 – 0.25 V, double layer capacitance currents are recorded (**figure 3-14 c**). The double layer capacitance of a DF electrode is 497 μF/cm^2, which is 61.1 times larger than that measured on planar diamond.

With the measurement of surface enlargement, the carrier density can be calculated from Mott-Schottky measurements (**figure 3-14 d**). The electrode surface area was calculated using 61.1 (surface enlargement) times the geometric area (0.384 cm^2). By extrapolating the linear fit of Mott-Schottky plot, the *x*-interception is the flat band potential (Φ_{FB}). The Φ_{FB} measured at different frequency shows a similar value of (0.875 ± 0.065 V). The results are listed in **table 3-3**. In accordance with Raman measurement, the acceptor density is below 1×10^{20} cm^{-3}, resulting in the absence of Fano resonance. However, this doping level corresponds to a conductivity of ~ 0.1 Ω^{-1}cm^{-1} [75, 83, 84], which is sufficient to conduct electrochemical measurements [85, 86]. The measured acceptor density is frequency dependent because at higher frequencies the ions in the electrolyte cannot follow the changing bias, then the effective acceptor density decreases.

Frequency (Hz)	Acceptor Density (10^{19} cm^{-3})	Flat Band Potential (V)
50	7.4	0.94
300	3.8	0.82
1000	2.3	0.81
3000	1.3	0.88

Table 3-3: Acceptor density and flat band potential calculated from Mott-Schottky measurements at 50, 300, 1000 and 3000 Hz over potential range of ±0.5 V; the electrolyte used was 3 M $NaClO_4$.

In order to investigate the reason for the lower doping, a planar diamond wafer was grown with the same parameter as the foam, with ~ 4 μm thickness. Then a five-layer foam was grown on it. Secondary ion mass spectroscopy (SIMS) is applied this sample (**figure 3-15 a**). For the foam, a boron concentration of 8.5×10^{19} cm^{-3} was measured which is in good agreement with the Mott-Schottky measurement; for the underlying planar diamond, however, the boron concentration is detected to be over one order of magnitude higher (1.5×10^{21} cm^{-3}). The lower boron-incorporation is believed to be related to the short growth time. For boron incorporation during diamond growth, (111) facet is easier to incorporate boron than (100) and (110) facets [87]. With our low methane growth atmosphere, planar diamond with long enough growth time will have a majority of (111) surface [88]. Therefore, the boron incorporation is higher than a diamond film with a smaller (111) proportion. However, the facets of diamond seeds

are randomly oriented leading to a less boron incorporation during the initial growth. Also, because of the 3D templates the diffusion of boron precursor into the site of growth may be hindered. This can also cause a doping level lower than expected.

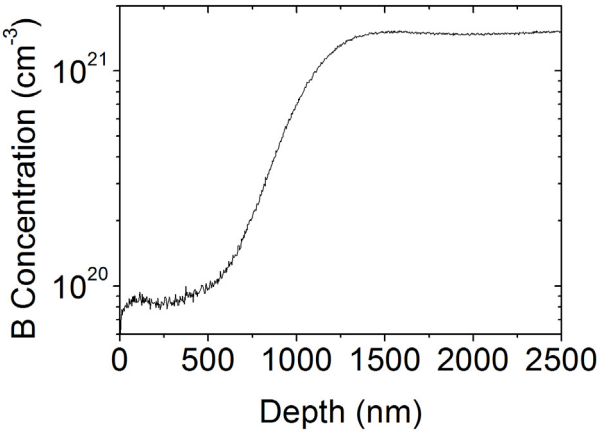

Figure 3-15: SIMS measurement on a diamond foam sample in which the 4 μm basal diamond and the foam are synthesized with the sample parameters (i.e. 650 °C, 1% methane, B/C=12000 ppm). The foam shows less boron incorporation than the basal diamond.

3.3 Summary and Conclusion

In this chapter, the growth of diamond on 3D substrate is investigated. Both silicon nanowires and silica spheres are used as templates. The work in this chapter proves that with CVD techniques, diamond coverage can be achieved even on complex 3D structures. Also, diamond foam, which is a new material, has been successfully fabricated. Growth techniques have been optimized regarding the template formation, seeding, and doping. Unlike diamond nanowires of which the surface enlargement is limited to ~ 20 times, the surface area of diamond foam can be enhanced by adding more layers to the electrode. Each layer provides ~ 7 times of a planar surface. Although the layer-by-layer growth is laborious, this material provides a new route for diamond surface enlargement.

Chapter 4: Introduction to Diamond-Based Supercapacitors

After the development on the surface enlargement of diamond electrode, the rest part of the thesis will be application-oriented. From this chapter on, **chapters 4 – 7** will focus on diamond based supercapacitors. This chapter will provide some basic knowledge about supercapcitors. Detailed discussions and complex theories are avoided; instead, they will be included later in the individual chapters when necessary.

In this chapter, the following questions will be answered:

1) What is a supercapacitor and what are the main parameters affecting its performance?
2) What are the materials used in this device?
3) What are the pros and cons to use diamond for such a device?

4.1 General Principle for Supercapacitors

A supercapacitor, or electrochemical capacitor, is an energy storage device that stores energy at the electrode/electrolyte interface. The research interest of supercapacitors arises from the need to renewably store energy from nature sources such as sun and wind, and then use it on demand [32]. Actually, for the purpose of high energy storage, Li-ion batteries have been extensively studied since early 1990s [89], but supercapacitors are receiving increasing amount of attention. Generally speaking, supercapacitors bridges the gap between electrolytic capacitors and batteries [32, 90]: it differs from Li-ion batteries as that the power density is much higher, i.e. faster charging and discharging during use; at the same time, it can store much more energy than traditional electrolytic capacitors.

In order to understand the working principle of a supercapacitor, it is helpful to first introduce the idea of an electrochemical double layer. From the view point of an electrical engineer, it is also helpful to compare it with a metal-oxide-semiconductor (MOS) structure, as is shown in **figure 4-1**. When an electrode is biased, the free ions in the electrolyte solution will accumulate at the liquid side of the interface, just like the accumulation of carriers at the semiconductor side with a MOS capacitor. As long as there is no faradic reaction taking place, the accumulated charge will not go across the interface. This situation is similar to the case of a MOS capacitor where the gate dielectric layer prevents the recombination of the accumulated carriers. However, this capacitor formed at the electrolyte electrode interface is considerably larger due to the small distance between the electrode and the first layer of ions (or the Helmholtz layer). Taking into account the thickness (d) of 0.5 to 1 nm of this Helmholtz layer and the dielectric constant ε_r = 10 for water in the Helmholtz layer [91], the specific capacitance value (C, F/cm^2) for such a capacitor can be estimated to be 10 – 20 μF/cm^2 using the following formula for parallel plate capacitors:

$$C = \frac{\varepsilon_0 \varepsilon_r}{d} \quad . \tag{4-1}$$

Therefore, it is very tempting to build capacitors using this mechanism. In a supercapacitor, two of such electrodes compacted face-to-face are needed. A suitable porous separator is needed to prevent any short circuit between these two electrodes. The structure of a supercapacitor device is schematically drawn in **figure 4-2**.

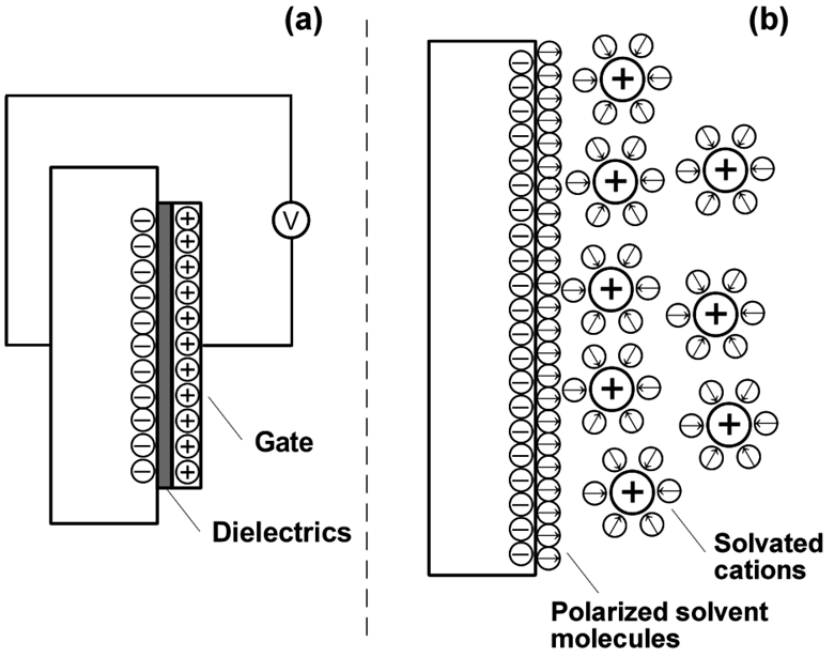

Figure 4-1: Schematic drawings of a MOS capacitor (a) and a double layer capacitor (b).

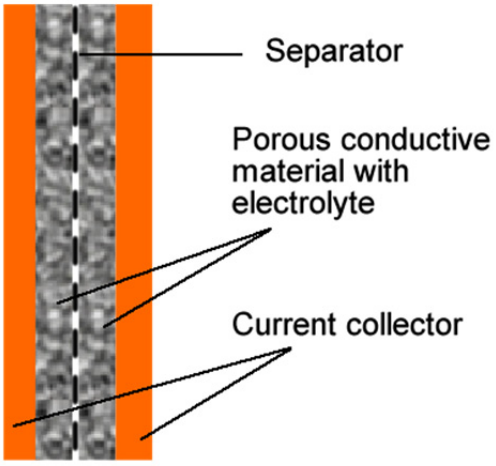

Figure 4-2: Schematic drawing of a supercapacitor device. Each supercapacitor device are consist of two pieces of current collector (usually metals), porous materials (*e.g.* activated carbon) immersed in electrolyte and a thin porous membrane as separator between the anode and cathode.

From the above principal, we can deduce two parameters which are important for the supercapacitor. The first and most obvious one is the total surface area. The capaci-

tance value will be linearly proportional to the total surface area of the electrode. Therefore, nanostructured, surface enlarged electrodes will be necessary. Secondly, the opposite charge at the two sides of the interface must not recombine, i.e. no faradic reactions are allowed for this device. In electrochemistry, the potential range in which there is no electron transfer across the electrode/electrolyte interface is called the potential window of such a system. Although the potential window has nothing to do with the capacitance value, it decides the energy storage of a supercapacitor device by:

$$E = \frac{1}{2} C {V_{ECW}}^2 \quad , \tag{4-2}$$

where V_{ECW} is the electrochemical window. The energy stored in the electrode is proportional to the square of the potential window. Therefore, a small potential window will severely limit the energy storage.

As mentioned, the Helmholtz layer thickness *d* in **equation 4-1** is affecting the capacitance. This problem will rise once salts with large ions are used. In fact, organic salts are typically used to enhance the potential window [92, 93]. However, the side effect is the larger ion size and thus the lower specific capacitance [94-96].

4.2 Electrolytes for Supercapacitors

There are two electrolyte systems for supercapacitors: aqueous and organic solutions. Aqueous solutions are usually concentrated acids, bases or salts. These solutions have very high conductivity (typically 500 - 700 mS/cm [97]), however, the potential window is limited by the thermodynamic limit of 1.23 V for water splitting. In order to overcome this limit, non-aqueous or organic solutions such as acetonitrile solution of tetraethylammonium tetrafluoroborate [34] have been applied. With these electrolytes, the potential window can be enhanced to 2 – 3 V [47, 98]. More recent developments of organic electrolyte systems include the application of room temperature ionic liquids [97], or room temperature molten salts, as solvent-free electrolytes for supercapacitors. With these liquids the potential window can be further enhanced to 4.5 V [93]. Besides the wide potential window, these ionic liquids are non-flammable, and easy to recycle [99]. However, one prominent problem for organic based electrolytes is the low electrical conductivity (typically 0.1 – 14 mS/cm [97]). Lower conductivity induces large series resistance and limits the operation speed of supercapacitors [90]. Also, the synthesis and purification of these electrolytes are still challenging [99]. Moreover, as a result of the large ion sizes of organic electrolytes (larger *d* in **equation 4-1**) the specific capacitance of activated carbon is ~ 50% smaller in organic electrolytes than in aqueous solutions [34]. In the next chapter, a detailed discussion will be given on the comparison between aqueous and organic electrolyte for diamond-based supercapacitor.

4.3 Materials for Supercapacitors

Currently, the predominating materials for commercially interesting supercapacitors are activated carbons because they are cheap, abundant, and easy to fabricate. The typical gravimetric capacitance reaches 100 – 200 F/g in aqueous solutions. However, using activated carbon materials there are several drawbacks:

1) Activated carbon electrode formation is powder- or slurry-based technology, i.e. the active material is usually pasted on macroelectrodes. However, the integration of such technologies in micro- or nanofabrication is difficult.

2) The typical potential window for activated carbon in aqueous electrolytes is 0.8 V; by using organic based electrolytes it can be enlarged to 4 V [34].

If fast, reversible, surface redox reactions are involved during charging and discharging processes, supercapacitors will become pseudocapacitors [37, 100-141]. They differ from typical double layer capacitors as the energy is not only stored electrostatically, but also chemically. Typical materials used in this category are usually metal oxides [37, 118, 136] and conductive polymers [110]. The pseudocapacitors work like batteries. Therefore, their performance is also closer to batteries with a theoretical specific capacitance as high as ~ 2500 F/g (nickel oxide) [113], with energy densities approaching that of batteries. However, the operation speed is not only dependent on ion diffusion, but also on the reaction kinetics. Therefore, the operation is slower than that of double layer capacitors. Typical pseudocapacitance reactions include [142]:

$$\mathrm{RuO_2} + \delta\mathrm{H^+} + \delta\mathrm{e^-} \leftrightarrow \mathrm{RuO_{2-\delta}(OH)_\delta} \quad , \tag{4-3}$$

$$\mathrm{NiO} + z\mathrm{OH} \leftrightarrow z\mathrm{NiOOH} + (1-z)\mathrm{NiO} + \mathrm{ze^-} \quad , \tag{4-4}$$

$$\mathrm{MnO_2} + \mathrm{X^+} + \mathrm{e^-} \leftrightarrow \mathrm{MnOOX} \quad , \tag{4-5}$$

where $0 \leq \delta$, $z \leq 1$, X^+ is H^+, Li^+, Na^+ etc.

In order to reduce the use of metal oxides and enhance the capacitance, hybrid systems are often used. The idea is to deposit thin films of pseudocapacitance materials onto high surface area support such as carbon nanotubes and graphene [100, 110, 134, 139]. Also, the carbon substrate will act as current collector which enhances the speed of the device by reducing the resistance of the semiconductive metal oxide layer. However, the charging-discharging rate is still typically lower than 100 mV/s [130, 139, 140].

Boron-doped diamond has been introduced as an electrode material due to its low background current, chemical/physical stability and wide potential window in aqueous solutions [143]. From **equation 4-2**, we know that a wide potential window will be preferred for high energy storage in supercapacitors. High overpotential on diamond electrodes for inner sphere electron transfer processes which require adsorption of

reaction intermediates such as water splitting and halides oxidation is known since 1990s [40]. Therefore, the diamond electrode provides an inert surface for electrochemical processes [144], and this inertness is beneficial for supercapacitor applications. Although there have been wide applications such as electrochemical sensors [3, 9] and robust support for catalysts [145-147], the application of diamond based materials for supercapacitors was limited to only a few attempts around 2000 by Fujishima *et al* [4, 10]. They used diamond honeycomb structures etched by oxygen plasma with anodized alumina masks to enlarge the surface area of diamond electrodes. However, although a wide potential window was confirmed, their general conclusion was negative because of the small specific capacitance. After that this topic was not mentioned for more than a decade. Therefore, an in-depth investigation on diamond-based supercapacitor is of scientific interest.

Chapter 5: Characterization of the Electrolyte Interaction with Diamond

A supercapacitor consists of electrode and electrolyte. Since the electrode materials have been discussed in **chapters 2** and **3**, this chapter elaborates on the electrolyte. The discussion on the electrolyte for diamond supercapacitors can be divided into three parts:

1) Potential window: boron-doped diamond has the widest reported potential window in aqueous solutions [143]. In this chapter, the potential window of diamond in aqueous solutions is measured; for comparison, eight kinds of representative ionic liquids are investigated regarding the potential window.
2) Conductivity: a low conductivity was already known for organic based electrolyte. The conductivity of ionic liquids can be 1 - 2 magnitudes lower than aqueous ones [97]. In this part we developed a systematic method and a theory to enhance the conductivity of ionic liquids by dilute it with organic solvents.
3) Specific capacitance: specific capacitance in terms of μF/cm^2 can vary on different electrolytes [34]. For diamond, the value is dependent on ion size and depletion layer capacitance. Experimentally, capacitance values in both aqueous and ionic liquids are measured and discussed.

5.1 Aqueous Electrolytes

5.1.1 Electrochemical Window of Diamond in Neutral Aqueous Solution

The electrochemical window (ECW) of an electrode in a certain solution gives the potential range in which the solvent and electrolyte remain stable. It is a critical parameter because it defines the applicable potential range of such an electrode in electrochemistry applications. It has been long established that boron-doped diamond (BDD) has a wide ECW in aqueous solutions because of its large overpotential towards the hydrogen and oxygen evolutions [143]. This overpotential can be observed by comparing the potential window of diamond and other commonly used electrodes. **Figure 5-1** gives the ECW profile of different commonly used working electrodes in a neutral aqueous solution. For metal electrodes like Pt or Au, the overpotential for hydrogen/oxygen evolution is small. Therefore, the ECW is limited by the theoretical value of 1.229 V arising from the following two equations [148] (E^0 is the standard electrode potential):

$$2H^+ + 2e^- \leftrightarrow H_2(g) \quad E^0 = 0.000\,V \tag{5-1}$$

and

$$O_2(g) + 4H^+ + 4e^- \leftrightarrow 2H_2O \quad E^0 = +1.229\,V \quad . \tag{5-2}$$

Glassy carbon (GC) electrode, however, has a high overpotential towards hydrogen evolution [149]; therefore, the reduction edge of the ECW appears about 1 V more negative in comparison to Pt or Au. The situation for BDD is similar with glassy carbon but with even higher overpotential towards oxygen evolution, and the onset of oxidative decomposition of water is even 0.5 V larger than that of GC.

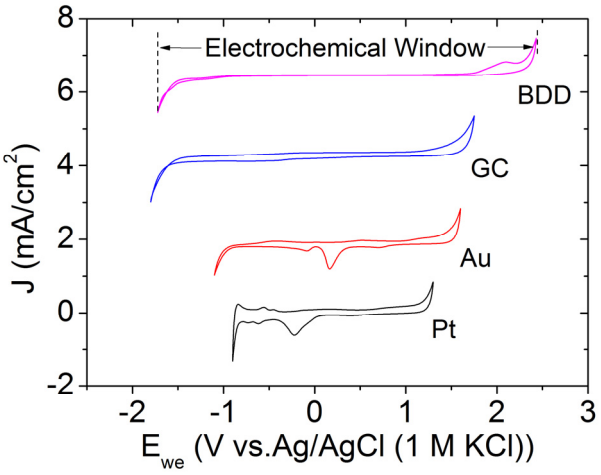

Figure 5-1: Electrochemical windows of (bottom to top) platinum (Pt), gold (Au), glassy carbon (GC), and boron-doped diamond (BDD) in an aqueous solution (3 M $NaClO_4$) with a cut-off current density of ± 1 mA/cm^2.

The fundamental difference between diamond and metal electrodes can be explained by the electron transfer model developed by Gerischer [150]. As is shown in **figure 5-2 (a)**, in equilibrium with a redox pair, the Fermi level (E_F) of a metal electrode is aligned with the standard potential (E^0) of the redox pair Re/Ox. In the case of water splitting, this redox pair corresponds to either H_2/H_2O or O_2/H_2O. For a positive bias (**figure 5-2 b**), the Fermi level is lowered and the electron energy in Re species become higher than the unoccupied states on the metal electrode. Electron transfer is therefore from Re to the electrode, and oxidation reaction happens. On the other hand, when a metal electrode is biased negatively, the Fermi level is raised up enabling electrons to escape the electrode (**figure 5-2 c**). In this case, unoccupied state on species Ox will be reduced by accepting electrons. When a semiconductor is considered, however, the situations are different. In semiconductors, a band gap is present, which means adjacent to semiconductor Fermi level there is no allowed state (**figure 5-2 d;** here a p-type semiconductor is discussed and the initial band banding is neglected for convenience). When a positive bias is applied, the Fermi level is moved below E^0. Because there are no available empty states above E_F, electron transfer is not immediately allowed. This causes an overpotential to oxidation reaction. Oxidation reaction will happen only if the E_F is lowered below the valence band maximum (VBM) and unoccupied states start to generate in the valence band (hole accumulation) (**figure 5-2 e**). Even if the electron transfer is enabled the transfer rate is not comparable to that of metal because of the density of accumulated carrier is related to the bias potential.

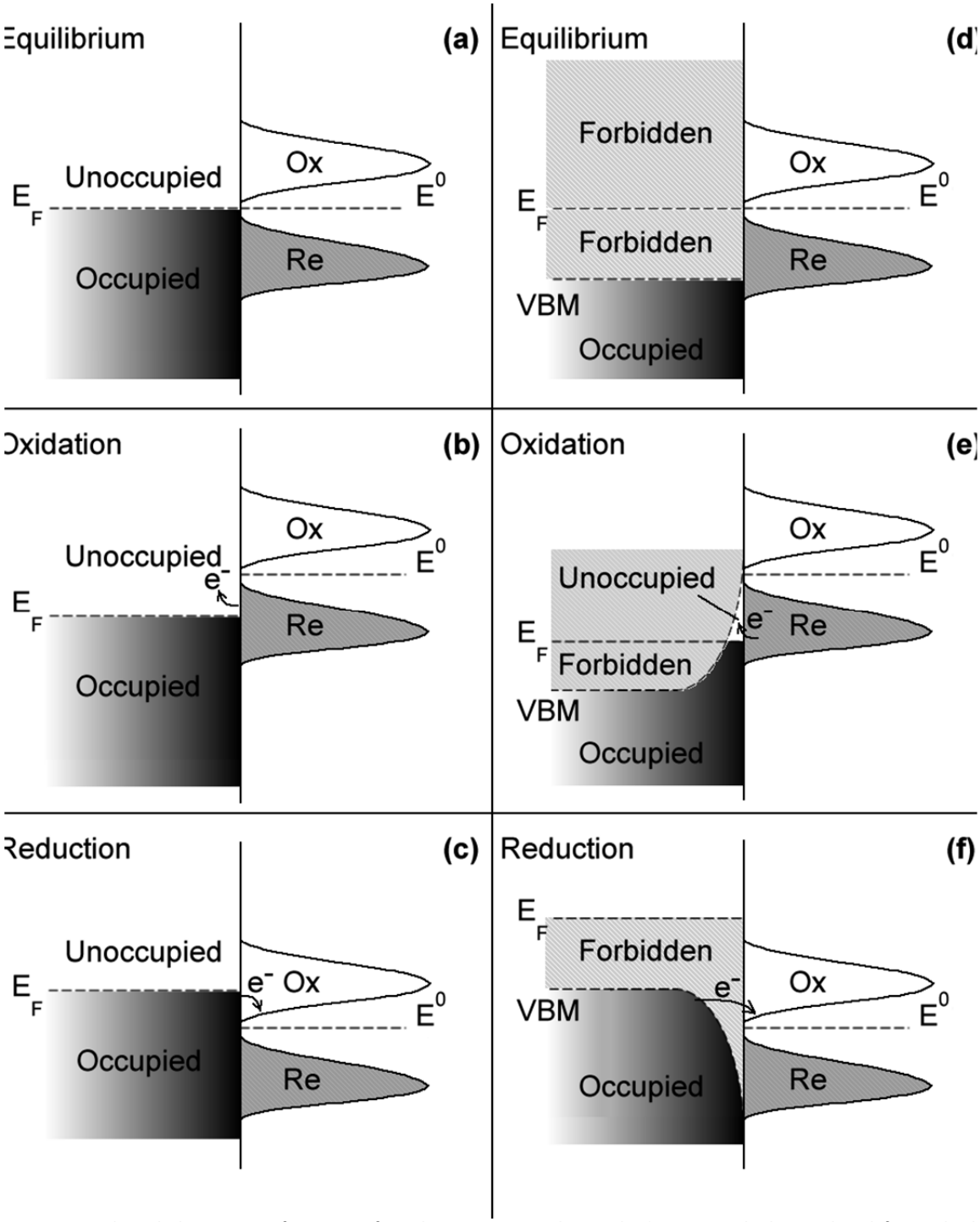

Figure 5-2: band diagrams of an interface between an electrode (a-c: metal electrode, d-f an ideal semiconductor electrode) and an electrolyte solution containing a redox pair at equilibrium (a, d), oxidation reaction (b, e) and reduction reaction (c, f). The initial band bending is neglected in (d), but this will not change the situations in (e) and (f).

When the accumulation starts the hole density is much lower than density of empty states in a metal. For reduction, there is again an overpotential (**figure 5-2 f**): the electron transfer is possible only when VBM is raised higher than E^0, and in this situa-

tion the electrons need to tunnel through a depletion layer. Therefore, the electron transfer is again slower than on a metal electrode.

5.1.2 The pH Dependence of Electrochemical Window of Diamond

For a given electrode, the potential window should not vary with different pH, as is defined by the Nernst equation:

$$E = E^0 - \frac{0.05916\ \mathrm{V}}{z} \log_{10} \frac{a_{\mathrm{Red}}}{a_{\mathrm{Ox}}} \quad , \tag{5-3}$$

where E^0 is the standard half-cell reduction potential; z is the number of moles of electrons transferred in the cell reaction or half-reaction; a is the chemical activity for the relevant species, where a_{Red} is the reductant and a_{Ox} is the oxidant. Therefore, the reduction potential of the reactions described by **equation 5-1** and **5-2** will both shift 59.16 mV per pH, i.e. the theoretical electrochemical window, which is limited by these two reactions, will not change with changing pH value of the solution, and remains 1.229 V.

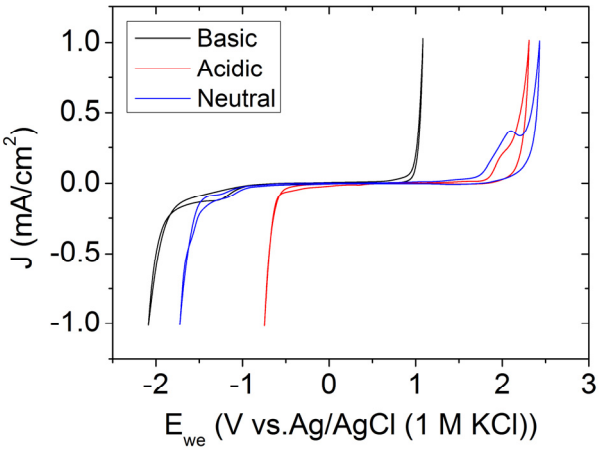

Figure 5-3: The electrochemical window measurements of a polycrystalline diamond electrode in acidic (2 M H_2SO_4), basic (3 M NaOH), and neutral (3 M $NaClO_4$) solutions. Cyclic voltammogram traces were taken within current densities between ± 1 mA/cm^2.

However, it is not the case in reality. **Figure 5-3 (a)** and **(b)** show the ECW measurements in 3 M NaOH and 2 M H_2SO_4. For acidic solution, the 1 mA/cm^2 cut-off on the oxidation side was 2.41 V which is similar to 2.45 V of the neutral solution, while on the hydrogenation side the cut-off was reached much earlier than in neutral solution at – 0.75 V. As is predicted by **equation 5-3**, the oxidation edge and reduction edge should move equally with changing pH, remaining the width of potential window constant. However, experimentally, this is only half true, i.e. for basic solution only oxygen evolution starts early, and for acidic solution only hydrogen evolution starts early.

In order to explain this, we take into account the capacitive charge accumulation. In **figure 5-4**, ion distributions in the double layer in six different situations are drawn

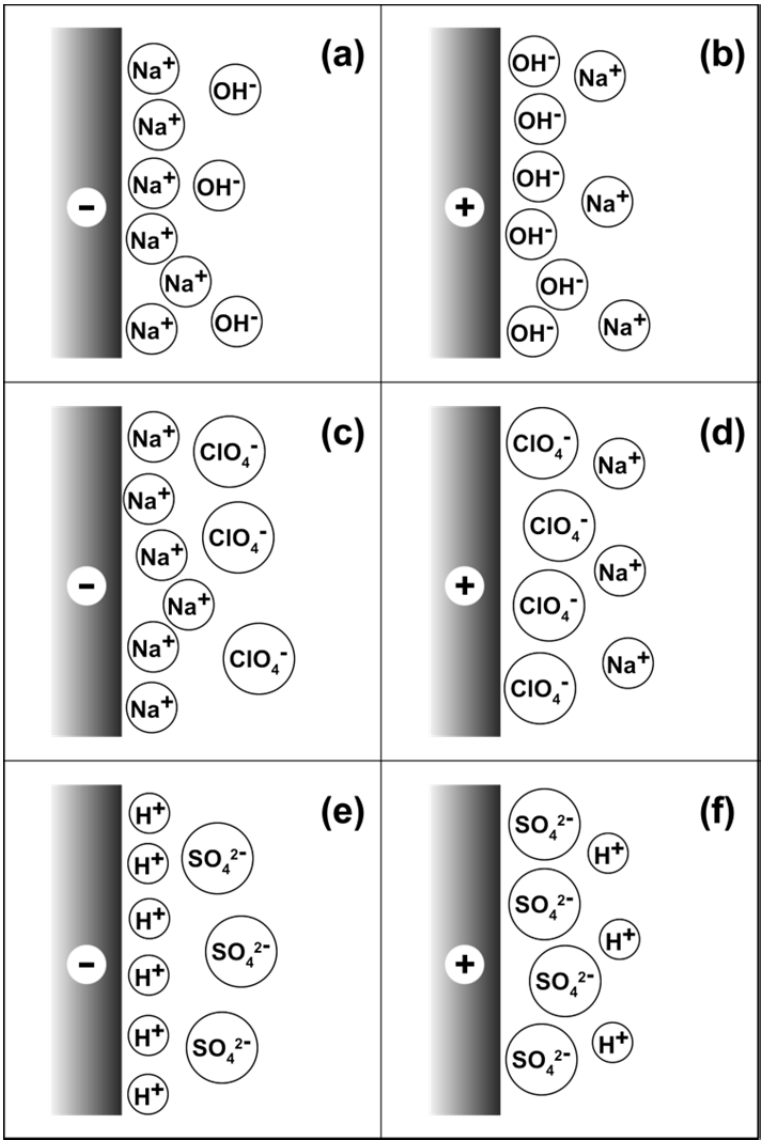

Figure 5-4: Schemes showing the ion distributions before hydrogen (a, c, e) and oxygen (b, d, f) evolution in basic (a, b), neutral (c, d) and acidic (e, f) solutions. In this figure, the basic solution is represented by NaOH; the neutral solution is represented by $NaClO_4$; and the acidic solution is represented by H_2SO_4.

schematically, i.e. under a negative bias (a, c, e) and under a positive bias (b, d, f) in basic (a, b), neutral (c, d) and acidic (e, f) solutions. In the situation of a neutral solution, depending on the bias, either Na^+ or ClO_4^- will be accumulated (**figure 5-4 c and d**). However, these two ions will not change the local pH; therefore, the onset for hydrogen and oxygen evolution will not be affected. Similar are the situations in acidic solution with a positive bias (**figure 5-4 f**) and basic solution with a negative bias (**figure 5-4 a**). However, in the cases of **(b)** and **(e)** of **figure 5-4**, the situations are different. In a basic solution at a positive biased electrode, OH^- will be accumulated, enhancing the local pH. Therefore, the onset of oxygen evolution will be shifted to lower potential than predicted by **equation 5-3**. Similarly, in an acidic solution with negative

bias (**figure 5-4 e**), H^+ will be accumulated, which decreases the local pH. According to **equation 5-3**, the onset potential of hydrogen evolution is shifted positively.

The pH change is dependent on the accumulated charge, and the charge is exponentially dependent on the bias [151]. Because diamond has overpotential for hydrogen and oxygen evolutions, the accumulated charges before these two reactions can change local pH considerably. With the shift of the onset potential of oxygen and hydrogen evolutions, the local pH in the Helmholtz layer can be calculated using **equation 5-3**. The onset potentials for oxygen evolutions shift 59.16 mV per pH. Therefore, for acidic solution, the hydrogen evolution appeared about 1 V earlier; the local pH is therefore estimated to be -9. This indicates that that the Helmholtz layer is composed of mainly H^+ ions. The same mechanism also applies to basic solutions; before oxygen evolution, the local pH is estimated to be 23, and the Helmholtz layer is composed of mainly OH^- ions. Therefore, for supercapacitor applications on diamond, neutral solutions are preferred for providing a larger potential window.

5.2 Ionic Liquids

5.2.1 Electrochemical Window

The electrochemical windows of eight kinds of ionic liquids are investigated by cyclic voltammetry with a current cut-off of 0.5 mA/cm^2. Five different categories of cations (imidazolium, pyridinium, pyrrolidinium, piperidinium, and tetraalkylammonium) and three anions (tetrafluoroborate, methanesulfonate, bis(trifluoromethylsulfonyl)imide) are tested. The structures of these ions are shown in **figure 5-5**. The ECW of these ionic liquids are shown in **figure 5-6**. Four main phenomena become obvious:

1) The electrochemical windows of different ionic liquids can very different: with the smallest observed for EMIMBF4 (1-Ethyl-3-methylimidazolium tetrafluoroborate) with a potential window of 3.6 V. For wide ones like N1114BTA (Butyltrimethylammonium bis(trifluoromethylsulfonyl)imide) the potential window can reach 5.9 V.
2) By comparing (a), (b), and (c), which have the same cation, we know that the BTA is the most stable anion.
3) For the same kind of cation with different length of alkyl chains (c, d), the potential window is similar, but the slope of the current increase at the edge of potential window is smaller with longer chains, showing lower conductivity.
4) The electrochemical window shows the potential range in which the electrolyte is stable. Therefore, the ionic liquids with smaller potential windows are less stable. Among ammonium based cations, i.e. imidazolium (a-d), pyridinium (e), pyrrolidinium (f), piperidinium (g), and tetraalkylammonium (h), the ones with unsaturated bonds are less stable (a-e), with Pyridinium being the least stable one (e); the three saturated ammoniums have similar stability (f-h).

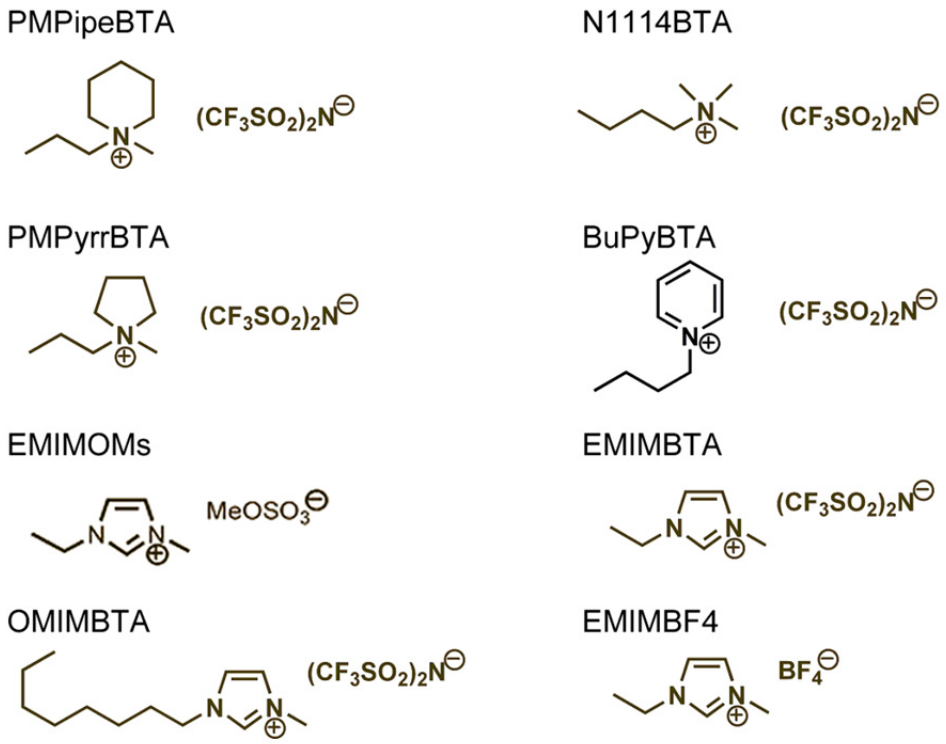

Figure 5-5: Molecular structures of eight kinds of ionic liquid under investigation: PMPipeBTA (1-Methyl-1-propylpiperi-dinium bis(trifluoromethylsulfonyl)imide), PMPyrrBTA (1-Methyl-1-propylpyrrolidinium bis(trifluoromethylsulfonyl)imide), EMIMOMs (1-Ethyl-3-methylimidazolium methyl-sulfate), OMIMBTA (1-Ethyl-3-Octylimidazolium bis(trifluoromethylsulfonyl)imide), N1114BTA (Butyltri-methylammonium bis(trifluoromethylsulfonyl)imide), BuPyBTA (1-Butylpyridinium bis(trifluoromethylsulfonylimde), EMIMBTA (1-Ethyl-3-methylimidazolium bis(trifluoromethylsulfonyl)imide), EMIMBF4 (1-Ethyl-3-methylimidazolium tetrafluoroborate).

Although these data are helpful in the selection of ionic liquid systems for supercapacitors, they do not show an obvious overpotential of diamond on the decomposition of ionic liquids. The potential windows are very similar with those reported on GC or Pt electrodes [92, 97]. For example, EMIMBTA has a potential window of 4.19 V on a GC electrode; here, on a diamond electrode, the potential window is 4.42 V; PMPyrrBTA has a potential window of 5.30 V on a glassy carbon electrode [97]; here, on a diamond electrode, the potential window is 5.67 V. Therefore, using diamond in combination with ionic liquids cannot enhance the potential window as expected.

The reason for this can also be explain with the model shown in **figure 5-2 (e)** and **(f)**. Because ionic liquids are more stable than water, the oxidation bound and reduction bound are further separated than 1.23 V. Therefore, in order to realize IL oxidation and reduction, high potentials are needed. However, in the case of **figure 5-2 (e),** when the applied potential is large, the surface will have strong hole accumulation which increases the carrier density; also, similarly, in **figure 5-2 (f)**, the surface will be highly depleted generating a high internal field which facilitates electron tunnelling. In another word, at high biases (either positive or negative), the difference between dia-

mond and metal disappear. Therefore, the measured potential window on diamond electrode is very similar to that on conductor electrodes (like Pt or glassy carbon). A comparison between the electrochemical window of different ILs on Pt and diamond electrodes is shown in **table 5-1**. It is again confirms that the ECWs on these two electrodes vary only slightly.

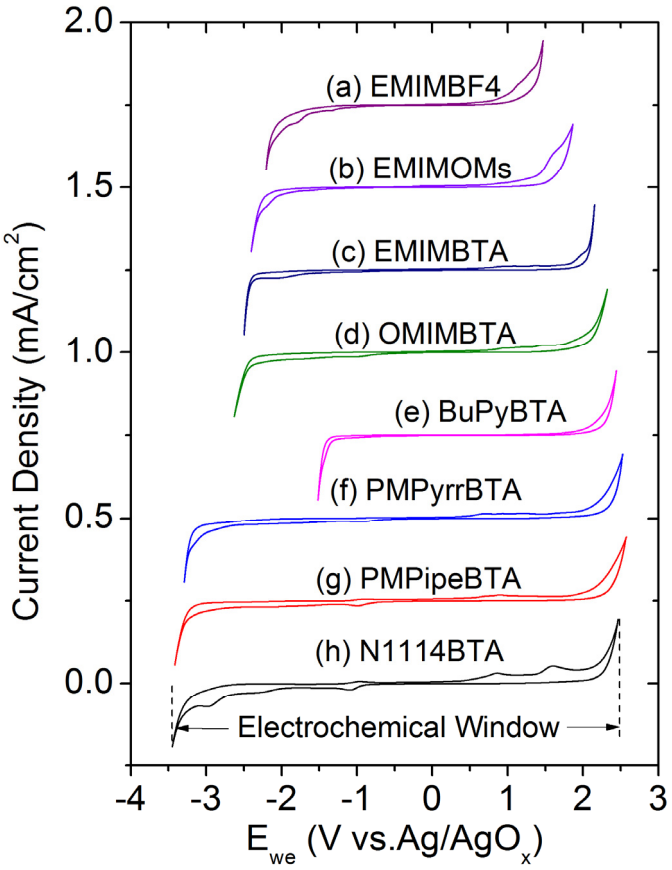

Figure 5-6: Electrochemical windows of a diamond electrode in eight kinds of ionic liquids.

ILs	ECW on Pt (V)	ECW on Diamond (V)
EMIMBTA	4.7	4.6
OMIMBTA	5.4	5.0
EMIMOMs	4.0	4.2
PMPipeBTA	5.9	5.8
PMPyrrBTA	5.9	6.1
N1114BTA	6.1	6.1
BuPyBTA	4.2	3.9

Table 5-1: A comparison between the electrochemical window of different ILs on Pt and diamond electrodes.

5.2.2 Conductivity

Although diamond provides only 200 to 400 mV overpotential to ionic liquid decomposition compared to traditional electrodes, it still obtains wider potential window in

ionic liquids than in aqueous solutions. Therefore, the next question is whether or not the ionic liquids can become as conductive as aqueous solutions

The low conductivity comes from high viscosity [142], i.e. ions move slowly in the liquid under a given electrical field (or low mobility μ). In an ionic solution, μ is described by Stokes-Einstein Relation [152]:

$$\mu = \frac{z}{6\pi r\eta} \quad , \tag{5-5}$$

where μ is the ion mobility, r is the radius of ions, η is the viscosity and z is the ionic charge. The mobility and diffusion coefficient (D) are correlated by Einstein relation [152],

$$\frac{\mu}{zD} = \frac{1}{kT} \quad , \tag{5-6}$$

where k is the Boltzmann constant, and T is the temperature. The diffusion coefficient is again related to conductivity (σ) by the Nernst-Einstein Equation [152]:

$$\sigma = \frac{zcF^2}{RT}(D_+ + D_-) \quad , \tag{5-7}$$

where D_+ and D_- are the diffusion coefficient for cations and anions, respectively; F is the Faraday constant, R is the universal gas constant, and c is the molar concentration. If we substitute μ in **equation 5-6** by **equation 5-5**, we can correlate D with η:

$$D = \frac{kT}{6\pi r\eta} \quad . \tag{5-8}$$

Again, substitute D in **equation 5-7** by **equation 5-8**, we can express conductivity by viscosity and ion radius:

$$\sigma = \frac{zckF^2}{6\pi R\eta}\left(\frac{1}{r_+} + \frac{1}{r_-}\right) \quad . \tag{5-9}$$

It becomes obvious that for a certain ionic liquid $\sigma \propto c/\eta$. One possibility to increase the conductivity is to dilute the ionic liquids with low viscosity organic solvents. If the viscosity is reduced faster than the ionic concentration, the conductivity will increase. Propylene carbonate (PC) and acetonitrile (AN) can be used for this purpose [66, 153].

The effects of dilution of ionic liquids with PC and AN are characterized in this section. The conductivity is measured using an inductive sensor consisted of two wire-wound metal toroids encased in plastic cases (**figure 5-7**). In the left toroid, a driving alternating current (AC) is applied, generating an alternating electrical field which drives an alternating ionic current through the receiving toroid (on the right); and then a current

is induced in the receiving toroid. This current is analyzed, and its value is proportional to the conductance of the liquid in which the sensor is immersed.

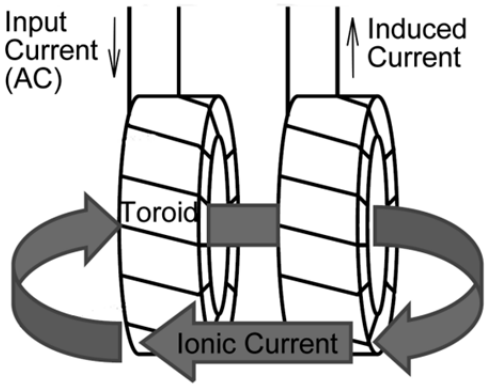

Figure 5-7: Scheme of the inductive conductivity measurement; when an AC current is flowing through the left toroid, an ionic flow is triggered through the right toroid; and then an AC current is induced in to the right coil and recorded. The recorded current is proportional to the conductivity of the electrolyte solution.

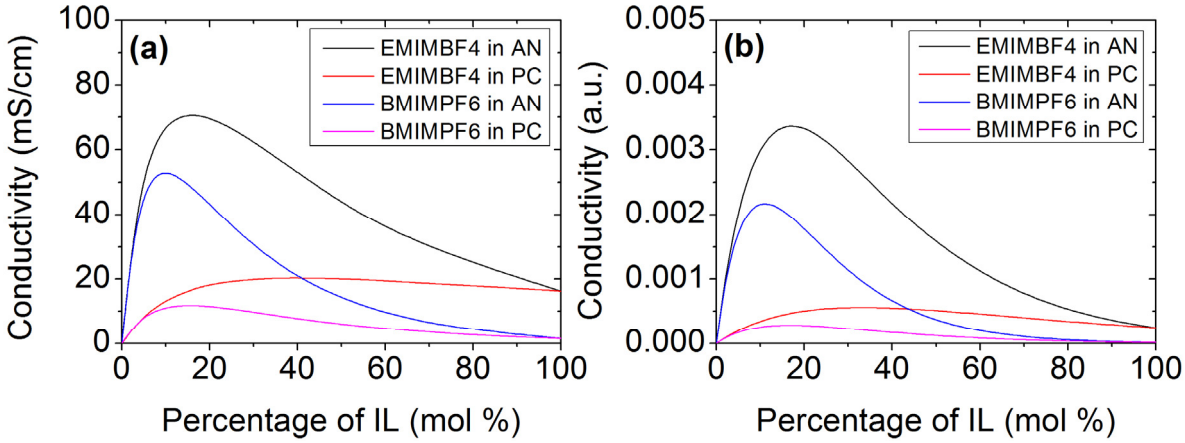

Figure 5-8: Experimental (a) and simulated (b) conductivity vs. mole percentage of ionic liquids in the solution for two kinds of ionic liquids diluted by two kinds of solvents.

Figure 5-8 (a) shows the electric conductivity vs. percentage of EMIMBF4 and BMIMPF6 in the solution. These two ionic liquids are chosen because EMIMBF4 has a low viscosity (25.7 mPa·s) and high conductivity while BMIMPF6 are just the other way round with a high viscosity of 312 mPa·s [97]. In all four combinations, conductivities are first enhanced but later decreased. Because $\sigma \propto c/\eta$, we can conclude that during the initial stage of the dilution, the effect of lowering η is predominant, leading to the increase in the conductivity. In the later stage of dilution, the conductivity is dominated by the reducing of ionic concentration. Therefore, the conductivity decreases.

Mathematical description of this phenomenon can be obtained by assuming a linear behavior of the natural logarithm of the viscosity of two-liquid mixture [154]:

$$\ln(\eta) = x_1 \ln(\eta_1) + x_2 \ln(\eta_2) \quad , \tag{5-10}$$

where η, η_1,and η_2 are the viscosity of the mixture, component 1 and 2, respectively; x_1 and x_2 are the mole percentage of component 1 and 2 (i.e. $x_2 + x_1 = 1$).

For the convenience, the mole percentage is converted to molar concentration by:

$$c = \frac{x_1}{\frac{x_1 MW_1}{d_1} + \frac{x_2 MW_2}{d_2}} \quad , \tag{5-11}$$

where MW_1, MW_2, d_1, and d_2 are molecular weight and density of component 1 and 2. η can be expressed by x_1 using **equation 5-10**:

$$\eta = e^{x_1 \ln\eta_1 + x_2 \ln\eta_2} \quad . \tag{5-12}$$

We rewrite **equation 5-9**, and substitute c and η using **equation 5-11** and **5-12**. We obtain the expression of conductivity which is a unary function of x_1,

$$\sigma = \frac{C_0 x_1}{e^{(x_1 \ln\eta_1 + (1-x_1)\ln\eta_2)} \left(\frac{x_1 MW_1}{d_1} + \frac{(1-x_1) MW_2}{d_2} \right)} \left(\frac{1}{r_+} + \frac{1}{r_-} \right) \quad , \tag{5-13}$$

where C_0 is a constant ($C_0 = kF^2/6\pi R$, where k is the Boltzmann constant, F is the Faraday constant, R is the universal gas constant). Using **equation 5-13** we can simulate the conductivity change during dilution.

	Acetonitrile (AN)		Propylene Carbonate (PC)	
	Simulation	Experiment	Simulation	Experiment
EMIMBF4	17%	18%	33%	35%
BMIMPF6	11%	10%	17%	15%

Table 5-2: Calculated and experimental optimum mole percentage of EMIMBF4 and BMIMPF6 in acetonitrile and propylene carbonate.

Figure 5-8 (b) shows the simulation result. The theoretical model based on **equation 5-10** to **5-13** precisely predicts the trend of the change in the conductivity, especially the peak concentration of IL solution (**table 5-2**). With the simulation, we can now understand that dilution with AN gives 2 – 4 times higher conductivity in comparison to PC is due to the lower viscosity of AN (AN: 0.343 mPa·s; PC: 2.50 mPa·s). However, this model fails to predict the absolute value of conductivity. In this model, we supposed that all the ions are separated, i.e. the concentrations of cations and anions are both equal to the molar concentration of ionic liquid. However, this is not true because in ionic liquids the cation and anions are often bond in pairs [152]. It has been reported in literature that, the iconicity (proportion of ionized ions) of ionic liquids can

vary in between 97% to 30% [155], i.e. for some ionic liquids only 30% of the ions are ionized. With dilution, this proportion may also change. However, this model is still helpful for the understanding of ionic liquid dilution, and it is an easy method to predict the optimized ionic liquid concentration for the highest conductivity.

5.2.3 Specific Capacitance

The total capacitance value of an electrode is calculated from the total surface area times the specific capacitance per unit area. Therefore, the specific capacitance is also an important parameter to optimize.

The expression of a double layer capacitance on an electrode surface is given by:

$$\frac{1}{C_{DL}} = \frac{1}{C_D} + \frac{1}{C_H} + \frac{1}{C_{Dep}} \quad , \tag{5-14}$$

where C_{DL}, C_D, C_H, C_{Dep} are the double layer capacitance, diffusion layer capacitance, Helmholtz layer capacitance, and depletion layer capacitance of the electrode, respectively. For a conductor electrode (like Pt, Au or GC), due to the high carrier density the depletion layer is thin leading to a large capacitance. Therefore, the case of a metal electrode the last part ($1/C_{Dep}$) is neglected. However, for a semiconductor electrode, the situation is different. The depletion layer capacitance for at semiconductor-electrolyte interface is given by:

$$C_{Dep} = \sqrt{\frac{e\varepsilon_0\varepsilon_r N_A}{2(\phi_B - V)}} \quad , \tag{5-15}$$

where e is the charge of an electron, $\boldsymbol{\varepsilon}_0$ is the vacuum permittivity, $\boldsymbol{\varepsilon}_r$ is the relative dielectric constant of diamond, N_A is the acceptor density, $\boldsymbol{\phi}_B$ is the barrier height at the interface, and V is the applied voltage. For a highly boron-doped diamond electrode, N_A is ~ 1×10^{21} cm^{-3}; the typical $\boldsymbol{\phi}_B$ varies between 1 – 4 V depending on the electrolyte and surface termination [86], the depletion capacitance ranges from 7 – 14 μF/cm^2, which is smaller than the typical double layer capacitance (10 - 30 μF/cm^2) [94]. In fact, diamond is widely used for electrochemical sensing because of its small capacitive current [40, 85]. However, a small depletion layer is not suitable for supercapacitor applications. Therefore, during diamond synthesis, a large amount of boron impurities were added to enlarge C_{Dep}, resulting in diamond electrodes which are degenerately doped with an acceptor density of up to 3×10^{21} [75].

In order to investigate whether the depletion layer capacitance is still limiting the overall double layer capacitance in both ionic liquids and aqueous solutions, the electrode capacitance is measured as a function of voltage. The series capacitance C_s is calculated from the imaginary part of impedance, Im(z) by:

$$C_s = -\frac{1}{2\pi f \mathrm{Im}(z)} \quad , \tag{5-16}$$

where f is frequency.

To estimate the influence of C_{Dep} on C_s, the Mott-Schottky plot ($1/C_s^2$ vs Voltage) is determined. From **equation 5-15**, $1/C_{Dep}^2$ shows a linear relationship with applied bias, while the diffusion layer capacitance and Helmholtz layer capacitance remain constant in the given electrolyte concentration [151]. Therefore, if C_{DL} is dominated by C_{Dep}, the Mott-Schottky plot should also show a linear decay. If measured by electrodes with the same doping level, the slope should be the same and from the slop the doping concentration can be calculated.

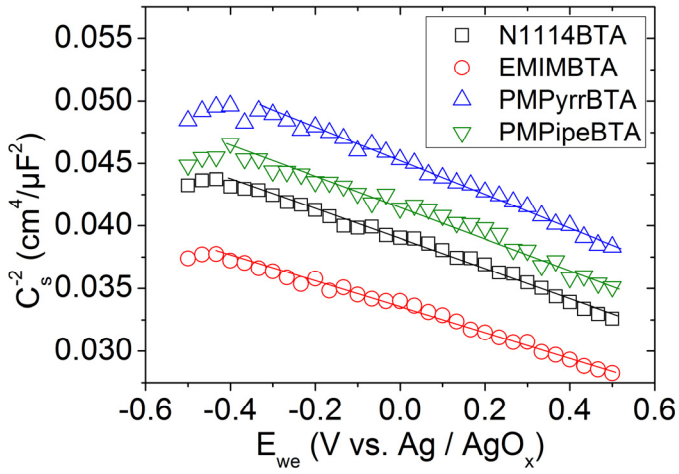

Figure 5-9: Mott-Schottky plots of four ionic liquids measured between ±0.5 V vs reference electrode. The capacitance C_s is measured at 50 Hz via impedance spectroscopy.

The Mott-Schottky plots of four kinds of ILs measured on the same diamond electrode are shown in **figure 5-9**. All the four curves show linear behavior with similar slope, indicating the C_s values measured in the four ILs are all dominated by depletion layer capacitance. The acceptor density in the diamond electrode calculated from the four curves is 2.0 ± 0.2×10^{21} cm^{-3}, which is typical for heavily boron doped diamond [75].

To further confirm if the depletion layer is limiting the capacitance, capacitive charging current in eight kinds of ionic liquids and one aqueous solution was measured within ± 0.25 V vs. Ag/AgCl reference electrode (**Figure 5-10 a**). The capacitive current density of an electrode is proportional to the specific capacitance (C_{DL}, µF/cm^2):

$$j_C = C_{DL}\nu \quad , \tag{5-17}$$

where j_c is the capacitive current density from the charging of the interfacial capacitance C_{DL}, and v is the scan rate (mV/s); j_c is measured at different scan rate and C_{DL} is calculated from the slop of j_c vs v. The results are shown in **figure 5-10 (b)**. The capacitance values vary only slightly for different ionic liquids: Most ionic liquids show capac-

itance values ~ 6 µF/cm^2. Only those with very small ions, such as BF_4^- and OMs^-, have slightly larger capacitance (~ 7 µF/cm^2), but the variation is not significant due to the limitation of depletion layer capacitance. For this reason, the specific capacitance in organic electrolyte is only ~ 30% smaller than in an aqueous one. This difference is smaller in comparison to activate carbon, which may amount to 50% [156].

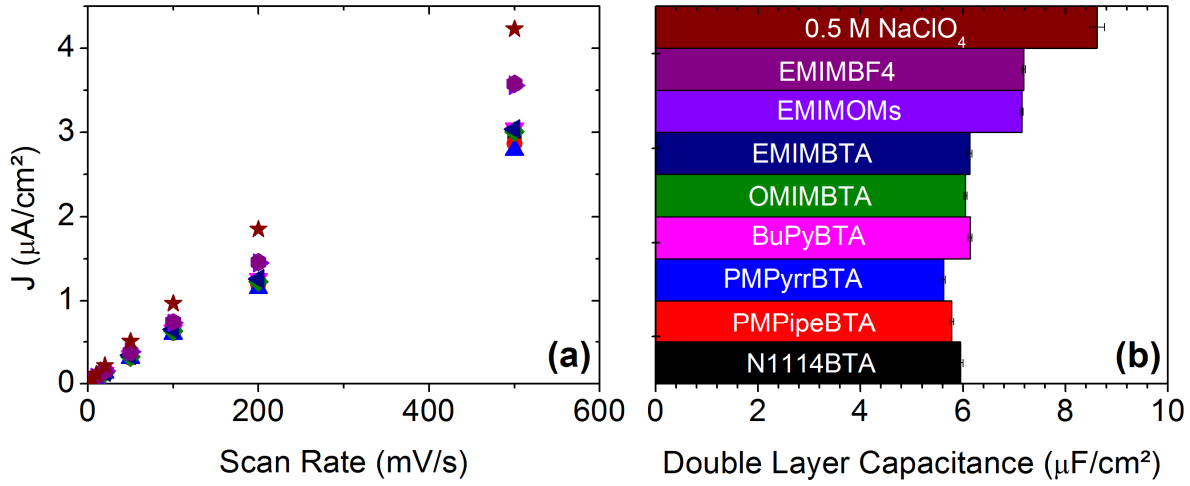

Figure 5-10: (a) Summary of the capacitive current vs. scan rate (a) (from top to bottom: 0.5 M $NaClO_4$, EMIMBF4, EMIMOMs, EMIMBTA, BuPyBTA, OMIMBTA, N1114BTA, PMPipeBTA and PMPyrrBTA) and double layer capacitance (b) of diamond in in these electrolytes calculated from (a).

5.2.4 Power and Energy Calculation

If we perform a simple calculation of device energy *E* and power *P* using [34]:

$$E = \frac{1}{2}CV^2 \tag{5-18}$$

and

$$P_{max} = \frac{V^2}{4R_s} \quad , \tag{5-19}$$

where *C* is the specific capacitance, *V* is the potential window and R_s is the series resistance. We can estimate that if we use ionic liquids in combination with diamond electrodes, only the energy increases slightly while the power is drastically lowered (**table 5-3**). Also, the organic electrolytes are more expensive [97]. Moreover, the potential window of an ionic liquid is highly sensitive to impurities, i.e. trace amount of water and oxygen will significantly shrink the potential window [157]. Therefore, further cost will be induced during the fabrication process to ensure a water and oxygen free environment. Therefore, the conclusion is that electrolytes based on ionic liquid are unfavored for diamond based supercapacitors.

One may ask why organic electrolytes are still widely used in nowadays supercapacitor industry. The answer lies in the fact that sp^2 carbon has a potential window of only ~ 1 V in aqueous solutions. Therefore, after using organic electrolytes the potential win-

dow gets a 300% increase (**figure 5-11**). Such a huge increase in potential window dominates all the negative effects such as small specific capacitance and large series resistance. For activated carbon using aqueous and organic electrolyte, the *E* and *P* are calculated and given in **table 5-3**. As expected, both the energy and power increase greatly with organic electrolyte.

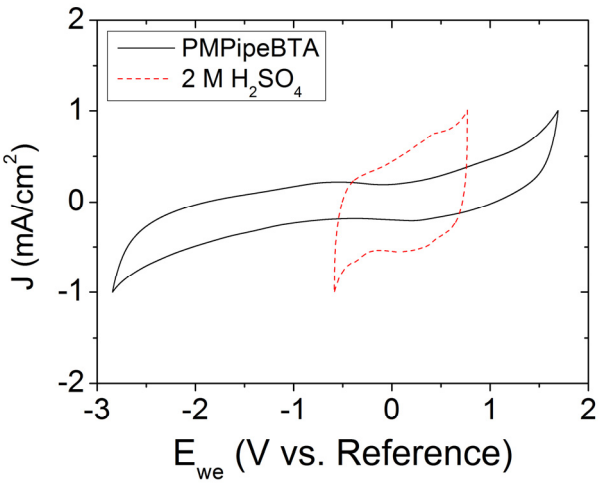

Figure 5-11: Potential window measurement on a carbon black electrode (loading: 0.4 mg/cm^2) in an aqueous solution (2 M H_2SO_4) and an ionic liquid (PMPipeBTA); for the aqueous solution, the reference electrode was Ag/AgCl (1 M KCl); for the ionic liquid, the reference electrode was a silver wire.

Material	Electrolyte	*V*	R_s	*C*	*E*	*P*
Diamond	Aqueous	1	1	1	0.5	0.25
	Organic	1.5	10	0.7	0.788	0.0563
Activated Carbon	Aqueous	1	1	1	0.5	0.25
	Organic	4	10	0.5	4	0.4

Table 5-3: Estimation of energy (*E*) and power (*P*) for diamond and activated carbon; potential window (*V*), series resistance (R_s) and specific capacitance (*C*) in aqueous solution are set as "1" for comparison.

5.3 Summary and Conclusion

With the experiments and discussions in this chapter, the following conclusions can be drawn:

1) Diamond electrodes have wider potential windows in neutral aqueous solutions than basic and acidic ones.
2) Ionic liquids can provide up to 50% wider potential window than aqueous solution. However, diamond has similar potential windows in ionic liquids compared to conventional electrodes (Pt, Au, GC, etc.).
3) A theoretical method to calculate the optimized IL/solvent ratio for maximum conductivity is created. However, the conductivity of ionic liquids is at least one magnitude lower than an aqueous one even after dilution.
4) For diamond based electrode, the depletion layer is always a limitation to the double layer capacitance. Therefore, the double layer capacitance for diamond

is not as sensitive to electrolyte properties as electrodes based on metals or sp^2 carbons.

5) Organic electrolytes cannot enhance the performance of a diamond electrode. As a result, aqueous solutions are favorable for developing diamond-based supercapacitor devices.

Chapter 6: Performance Tests of Diamond-Based Supercapacitors

After the selection of appropriate electrolyte for diamond-based supercapaoctors, in this chapter we will assemble a real device and test the supercapacitor properties. In the first part of this chapter, testing methods and theories about supercapacitor devices will be introduced. In the second part, experimental results, including potential window, device efficiency, capacitance, energy and power, are investigated and discussed in comparison with data reported on other materials.

6.1 Testing Methods

6.1.1 Two- and Three-Electrode Set-Ups

In the case of a supercapacitor electrode, the charges are stored in the electrode-electrolyte interface, i.e. double layer. However, in order to form a real supercapacitor device, a cathode and an anode are needed. Therefore, there are two such interfaces in every supercapacitor device. Therefore, each supercapacitor contains two double-layer capacitors in series connection [90]. This is called a two-electrode system as is depicted in **figure 6-1 (a)**. The equivalent capacitance is therefore only ½ of each electrode. Testing on a two-electrode set-up gives the real performance of a device, but sometimes requires sophisticated cell-design and assembly. Therefore, for convenience traditional three electrode cells can also be used. In a three-electrode set-up, the potential at the "counter-electrode" (which is actually the reference electrode) is fixed. Therefore, in such a set-up the equivalent circuit is a double-layer capacitor in series connection with an infinitely large capacitor, or ground (**figure 6-1 b**), and the measured capacitance is twice as large as the value measured with a two-electrode set-up. Besides capacitance, many other important parameters measured in two- and three-

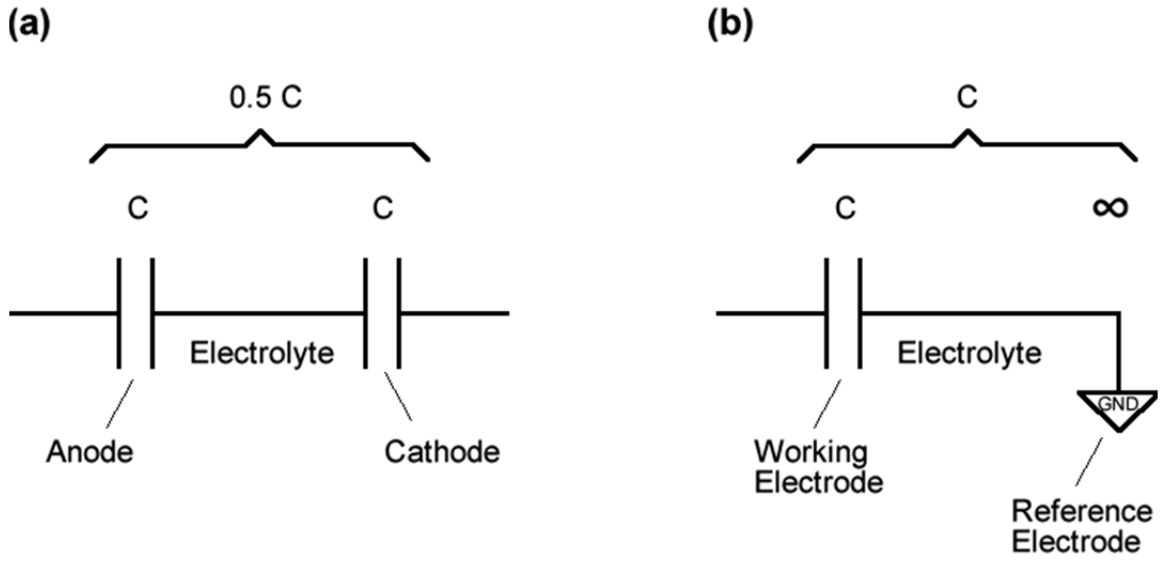

Figure 6-1: Schematic illustrations of a two-electrode system (a) and a three-electrode system (b).

electrode systems are also different, especially the areal and gravimetric capacitance (F/cm^2 and F/g). For example, in a two-electrode cell twice the amount of material (or area) is used but only half of the capacitance is measured; therefore, the areal and gravimetric capacitance obtained from a three-electrode system needs to be divided by four in order to estimate the real device behavior. In the following part, only the results from two-electrode measurements will be shown, because they represent the real device performance. However, information about three-electrode measurements is also available in previous publications [158, 159].

6.1.2 Equivalent Circuit

Figure 6-2 schematically shows the interface between an electrode and electrolyte. R_s is the series resistance which includes the electrolyte resistance, separator resistance, electrode resistance and contact resistance (between electrode and measuring device). R_p is the parallel resistance, which stands for a leakage current. In references this part is always omitted [160], because if a capacitor is working in the electrochemical window, there should be no current flowing through the interface. However, in some cases, if there is a slow faradic process, e.g. the surface oxidation of Si to SiO_2, oxide reduction or oxygen reduction, the R_p cannot be omitted. C_{dl} is the double layer capacitance.

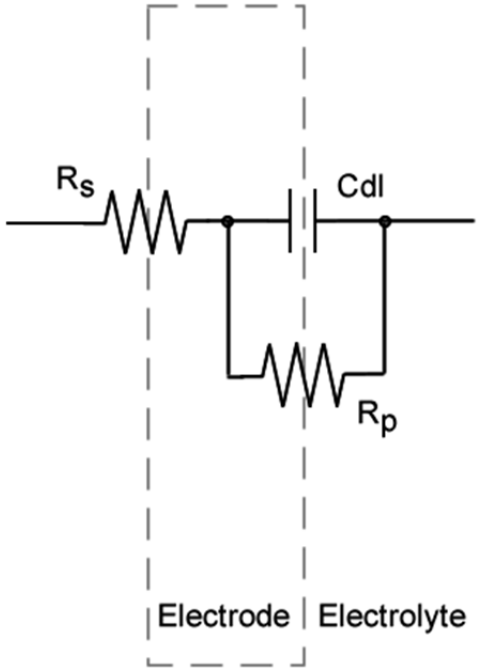

Figure 6-2: Equivalent circuit of an electrode-electrolyte interface.

6.1.3 Measurement Techniques and Theories

Two techniques are mostly applied in this chapter to investigate the supercapacitor performances.

(1) Cyclic Voltammetry (CV)

For the supercapacitor testing, cyclic voltammetry is a convenient and effective method to evaluate all the three elements, i.e. R_s, R_p and C_{dl}. CV of the three-element circuit is simulated with *Mathematica* (**figure 6-3**). In all the simulations, the scan rate is 1 V/s, the scan window is 2 V. C_{dl} was set to be 1 mF; the unit of all the resistances is Ω.

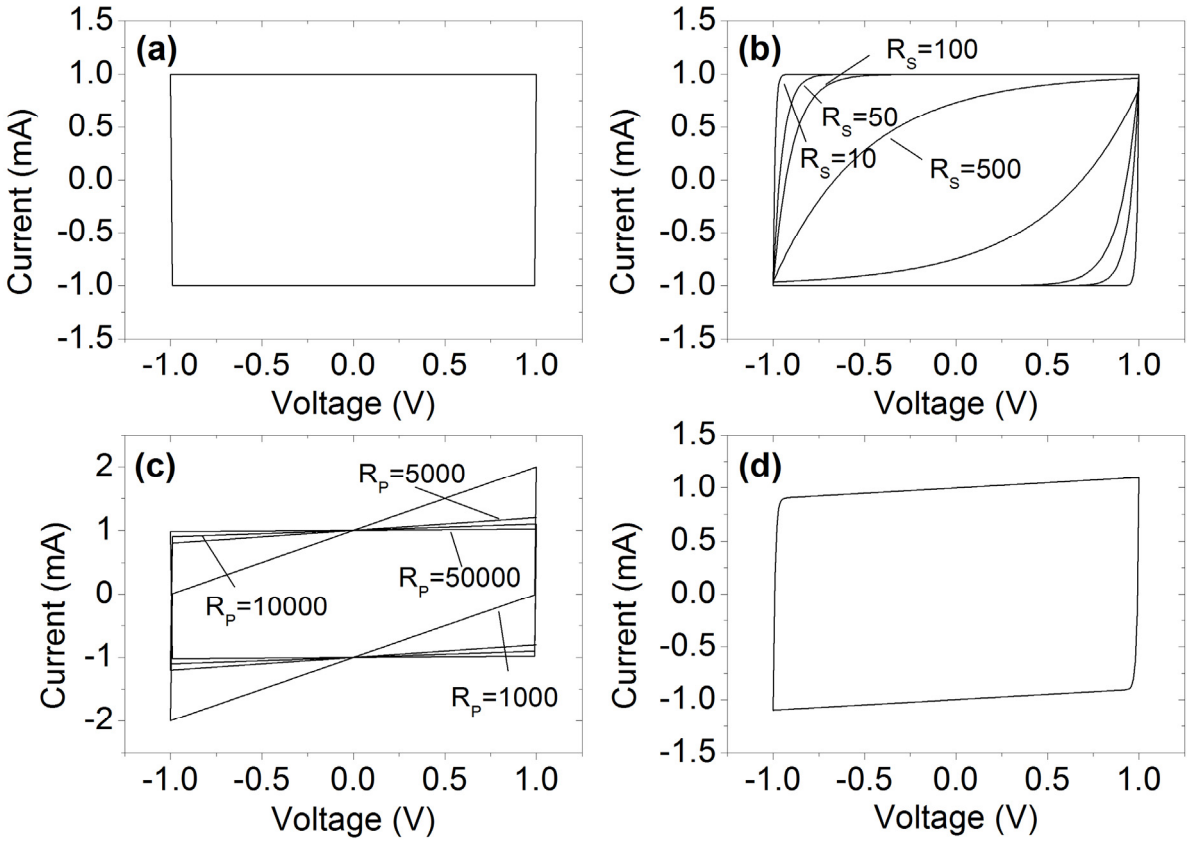

Figure 6-3: Simulations of supercapacitor equivalent circuit with R_s, R_p and C_{dl}: (a) ideal situation, R_s=0 and R_p=∞; (b) R_s≠0 and R_p=∞; (c) R_p≠∞ and R_s=0; (d) R_s≠0 and R_p≠∞.

In an ideal capacitor, namely, R_s=0 and R_p=∞, the charging and discharging currents are both constant (**figure 6-3 a**), and the C_{dl} value is calculated by:

$$C_{dl} = \frac{I}{v} \quad , \tag{6-1}$$

where I is the charging or discharging current and v is the scan rate.

If there is a large series resistance, the current cannot immediately rise from $-I$ to I at the end of each scan (**figure 6-3 b**; R_s = 10, 50, 100, 500; R_p = ∞), and the larger the R_s is, the slower the charging current rises. However, **equation 6-1** still holds; only the meaning of I changes to the stabilized charging current. If there is a very poor contact between the electrode and the potentiostat, or if there is a very resistive electrolyte/electrode, a very large R_s is expected, and the CV curve will be distorted (in the case R_s = 500) and the device is not measurable.

The R_p determines the leakage of the system. If R_p is too small (showing a large leakage), the charging current is not a constant, but "tilted" (**figure 6-3 c**, R_s = 0, R_p = 1000, 5000, 10000, 50000). The slope of the current represents the inverse of R_p. Therefore, the larger the leakage is (smaller R_p) the more heavily the CV curves are tilted. As stated previously, this leakage stands for a faradic process. For measurements in aqueous electrolyte under ambient atmosphere, a very strong leakage current is often seen if the metal current collector is in contact with the electrolyte or, more often, the backside silicon substrate in contact with water and is slowly oxidized during each scan. Fortunately, silicon generates an inert, protective silicon oxide layer after oxidation [161]. Therefore, the leakage current due to silicon oxidation will stop after tens of scans.

After the discussion above, we draw a more realistic CV curve in **figure 6-3 (d)** (R_s = 10; R_p = 10000). With this type of curve all parameters can be measured: C_{dl} can still be measured from **equation 6-1**, with I being the current at the center of the CV curve (V = 0 in this case); R_s can be fitted from the time constant ($\tau = R_s C_{dl}$) of the rising of current; the slope of the linear part of the charging current is equal $1/R_p$.

(2) Electrochemistry Impedance Spectroscopy (EIS)

Cyclic voltammetry would have solved all problems if the double layer capacitance were a constant. In the first chapter, a comparison is made between a MOS capacitor and a double layer capacitor. Although there are a lot of similarities, there is also one notable difference: the mobility of the charge carriers. In heavily doped silicon, the carrier mobility is 100 – 1000 $cm^2/ V{\cdot}s$ [161]; however, in aqueous electrolyte solution, the value is below 10^{-3} $cm^2/ V{\cdot}s$ [162]. Therefore, even at very low frequencies, the capacitance values are frequency dependent. At higher frequencies the ion movement cannot follow the alternating electrical field, and the capacitance drops. Experimentally, C_{dl} measured from CV curves at different scan rates will vary. Consequently, for such a system dynamic measurement is necessary. Compared to CV which scans over a wide potential range at a given frequency, EIS scans a very small potential range (±10 mV) with various frequencies, ranging from 1 MHz to 1 mHz. The potential for EIS is often chosen to be the open circuit potential (in a three-electrode system) or 0 V (in a two-electrode system) to avoid the disturbance from faradic processes. Therefore, in EIS data analysis, R_p can be omitted and the three-element equivalent circuit (**figure 6-2**) can be simplified to a two-element one, i.e. a RC series circuit [98]. The complex impedance of the system is then:

$$Z = Z' + jZ'' = R_s + \frac{1}{j\omega C_{dl}} \quad . \tag{6-2}$$

The Nyquist impedance plot of such an expression is a straight line with the *x*-intercept value being R_s. Here for the convenience in data processing, we regard the whole system as a capacitor, and *C* is the complex capacitance:

$$Z' + jZ'' = R_s + \frac{1}{j\omega C_{dl}} = \frac{1}{j\omega C} \quad . \tag{6-3}$$

If we separate the real and imaginary part of *C*:

$$C' = \frac{C_{dl}}{(1 + \omega^2 R_s^2 C_{dl}^2)} \tag{6-4}$$

$$C'' = \frac{\omega C_{dl}^2 R_s}{(1 + \omega^2 R_s^2 C_{dl}^2)} \quad , \tag{6-5}$$

and

$$C = C' - jC'' \quad . \tag{6-6}$$

For low frequencies ($\omega^2 R_s^2 C_{dl}^2 << 1$) *C′* stands for the double layer capacitance value. *C″* is an indicator of resonance frequency of the RC circuit, because it has a maximum when $\omega^2 R_s^2 C_{dl}^2 = 1$.

If we express *C′* and *C″* with *Z*, we have:

$$C' = \frac{-Z"(\omega)}{\omega |Z(\omega)|^2} \tag{6-7}$$

and

$$C'' = \frac{Z'(\omega)}{\omega |Z(\omega)|^2} \quad . \tag{6-8}$$

With **equation 6-6** and **6-7**, one can easily convert impedance measurement into capacitance measurement. For R_s = 10 Ω, C_{dl} = 1 mF the *C′* and *C″* are simulated in **figure 6-4 (a)**. As expected, at lower frequencies *C′* is constant and equals to C_{dl}, and *C″* has a maximum at the resonance frequency ($f = 1/R_s C_{dl}$); the inverse of this frequency is defined as the relaxation time. From an electrical engineering point of view, it marks the frequency at which half of the input energy is stored, i.e. the efficiency of the device drops to 50%. Also, this frequency can be determined from the Bode plot, and it corresponds to the frequency at a -45° phase shift.

We can see from the analysis above, by converting complex impedance *Z* to the complex capacitance *C*, more information is obtained than a straight line in the Nyquist plot.

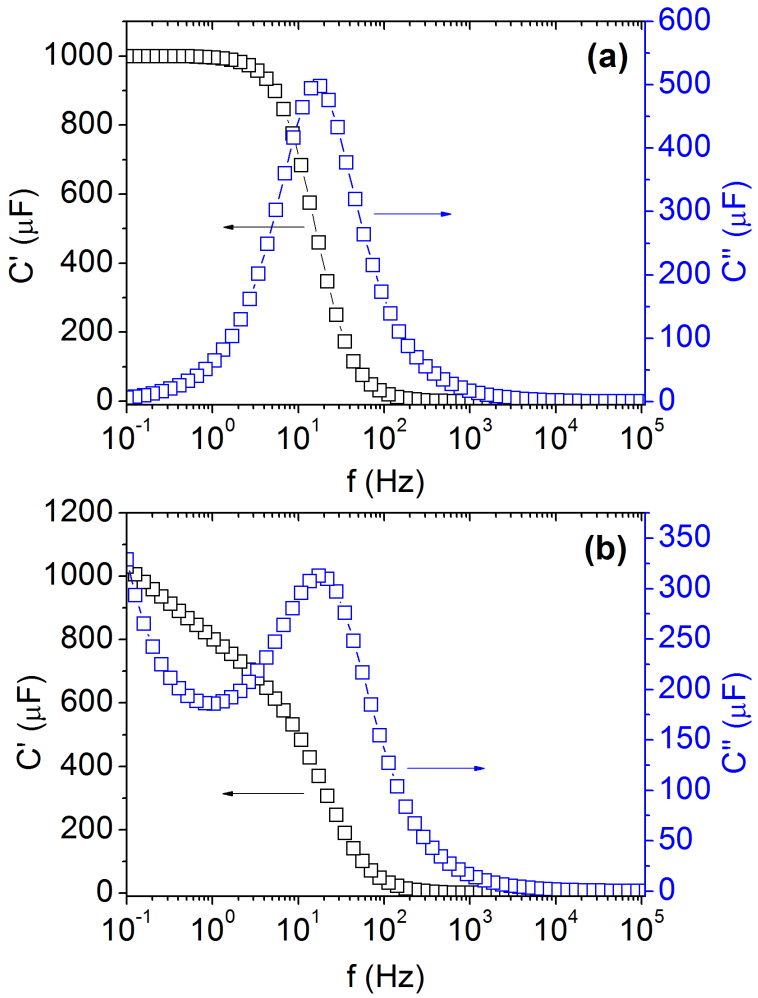

Figure 6-4: Complex capacitance simulation of (a) a RC series circuit and (b) a RQ series circuit.

Up to now C_{dl} is treated as a constant for simplicity; however, this is not the true nature of a double layer capacitor. In electrochemistry, a double layer capacitor is actually described as a constant phase element (CPE, the symbol in the equivalent circuit is *Q*) [163]. Its impedance Z_Q is:

$$Z_Q = \frac{1}{j\omega^{\delta} Q_0} \quad , \tag{6-9}$$

where Q_0 and $0<\delta<1$ are two constants related to the intrinsic property of a CPE. Compared to the impedance of a capacitor, a CPE is actually a capacitor with frequency dependent capacitance, and its equivalent capacitance C_{eq} can be expressed as:

$$C_{eq} = Q_0 \omega^{\delta-1} \quad . \tag{6-10}$$

With increasing frequency, the capacitance value decreases. Although the creation of CPE describes many experimental results well, there is up to now no real theoretical explanation why a double layer capacitor behaves in this way [164]. However, it is possible to give a qualitative understanding: for a parallel-plate capacitor, we always as-

sume the charges at two electrodes are identical in quantity but opposite in signs. However, in the case of a double layer capacitor, the two "plates" are asymmetric and the electrolyte half "responds" much slower than the electrode. In this condition, if we charge the device at a high frequency, the faster electrode has reached a charge Q, but the "slow" electrode only accumulated a charge $Q' < Q$. As a result, capacitance at this high frequency is smaller than the one at low frequencies.

For the inclusion of CPE in the simulation of the complex capacitance, with $\boldsymbol{\delta} = 0.9$ and $Q_0 = 1$ mF, the result is shown in **figure 6-4 (b)**. The most obvious change is that the low frequency part of C' is not a constant, but frequency dependent.

To summarize, the most important point for this section is the frequency dependent performance of a supercapacitor. The general trend is, the higher the frequency, the lower the capacitance. In detail, there are two factors which render this trend:

1) The nature of a RC circuit determines that the energy stored in the capacitor is a function of frequency. At high frequencies, the impedance of the capacitor decreases, and most of the energy input is dissipated on the series resistance. Therefore, the equivalent capacitance of the whole device decreases.
2) A double layer capacitor differs from solid-state capacitors insofar as that its capacitance is frequency dependent. The mobility of ions is several magnitudes slower than the carrier mobility in semiconductors or metals, resulting in a long period of time until equilibrium is reached. This situation is especially true when porous electrodes are used and ion movements are further confined in the system.

The first factor is a systematic limitation, while the second one is the intrinsic property of an electrochemical capacitor. In the next sections, experimental results will be discussed regarding these two points.

6.2 Two-Electrode Measurements

6.2.1 Cell Assembly

The cell assembly follows the sandwich structure of electrode-separator-electrode. Compared to a normal aqueous activated carbon set-up, there are two problems that present themselves in the case of the diamond-based supercapacitor cell:

1) It is not possible to use metal contacts or metal current collecting layers. In an activated carbon cell, the working potential window (0.8 V) is smaller than the thermodynamic decomposition potential window for water (1.23 V). Therefore, even if the metal is in contact with the electrolyte, the potential window will not be affected. In fact, gold is quite often used as the material for contact pads [165]. However, for diamond, because the electrodes work at a potential

window above 1.23 V, any metal parts in contact with water will create a leakage current, rendering the device unusable at high voltages.

2) Unlike supercapacitors made from activated carbon, the materials used in this thesis are mostly semiconductors, therefore, multi-junction exists which causes a high series resistance. In current technology, diamond is grown on silicon, so there is a diamond-silicon junction, and then the back of silicon needs to be in contact with a metal pad, and there will be a metal-silicon junction. Metals, including Pt, Au, Al and stainless steel are used as the metal contact and stainless steel proved to be the best. However, the series resistance for each electrode is ~ 3 Ω, which is still considerably higher in comparison to activated carbon electrodes [160].

The testing cell is made of two pieces of Polytetrafluoroethylene (PTFE) plates with a 1×1 cm^2 depression to embed the two pieces of electrodes. The two plates are held together by four screws. Filter paper is used as separator. The final device is shown in **figure 6-5**. For convenience in later discussion, the diamond nanowire samples are named as DiaNW; the diamond coated silicon wires are called DiaSiW; and diamond foam is called DiaFoam.

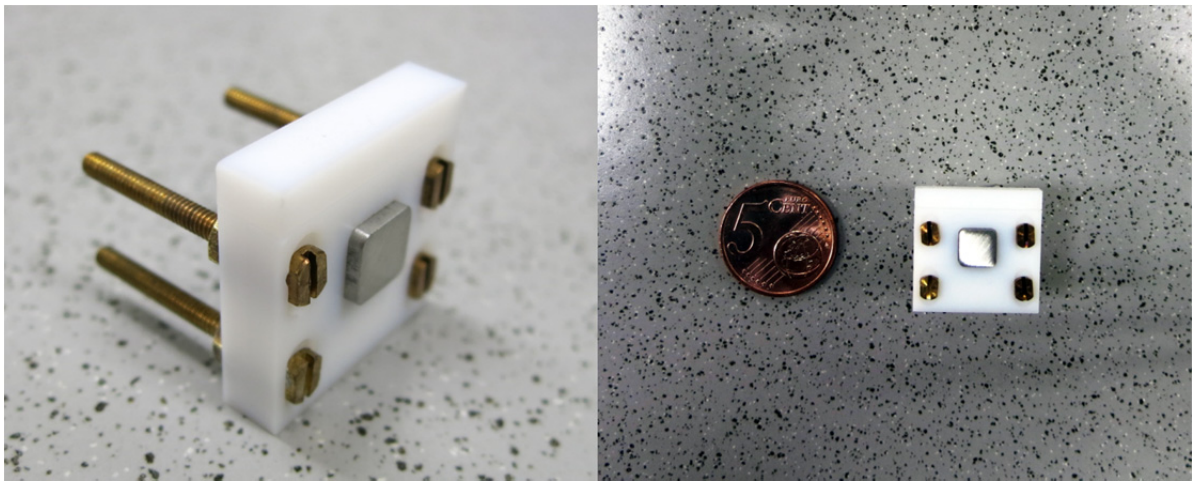

Figure 6-5: Photographs of a two-electrode supercapacitor test cell.

6.2.2 Potential Window Definition

To have an understanding of the device, two planar diamond electrodes are first assembled into the test cell. Initially, the potential window is determined by a "window opening test". In such a test, the potential window is first set at 1 V which is lower than the theoretical electrochemical window of water. Therefore, in this case a featureless, rectangular shaped capacitive current should be recorded. After that, the potential window increases by 0.5 V each time, and the CV curves are recorded (shown in **figure 6-6**). Because diamond has slow kinetics for water splitting, the large water splitting peak does not become obvious until the window is expanded to 2.5 V. Also, noticeably, the reduction current also increases each time when the window is wid-

ened. This means that the products of water splitting (i.e. H_2 and O_2) can partially adsorb on the diamond surface, and during discharging, they can recombine and give out current (like a fuel cell).

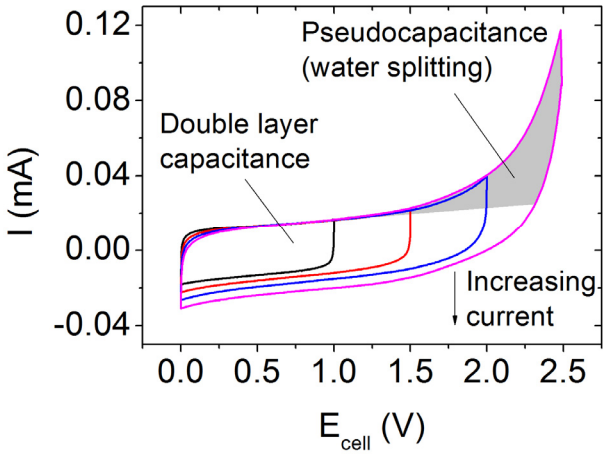

Figure 6-6: Cyclic voltammetry of a capacitor composed of two planar diamond electrodes of 1×1 cm^2 in potential windows of 1.0-2.5 V in 3 M $NaClO_4$ at 1 V/s.

As in the sensor application, the potential window is also very important for supercapacitors. However, because diamond is not a conventional material for this application, the definition of the potential window does not exist so far. For a sensor electrode, as long as the background current is small enough (smaller than signal), the device is still usable. Therefore, a current limit (often 1 mA/cm^2) is used to define the potential window, as done **in chapter 5**. However, for supercapacitors this is not a feasible criterion. For example, in the case of a potential window of 2.5 V, the current is still small (~ 0.12 mA, or 0.06 mA/cm^2). However, the water splitting is already obvious, and water splitting consumes energy which should be stored in the device. As a result, the efficiency of such a device decreases. Therefore, efficiency is a plausible criterion by which the the potential window can be defined. Experimentally, the efficiency of each cycle in cyclic voltammogram is calculated by:

$$\text{Efficiency} = \frac{Q_{discharging}}{Q_{charging}} \times 100\% \quad , \tag{6-11}$$

where $Q_{charging}$ and $Q_{discharging}$ are the amount of charge during charging and discharging processes, respectively. The results are plotted in **figure 6-7 (a)**. As expected, in the 1 V window, there is no water splitting and the efficiency is close to 100%. Starting from 1.5 V the water splitting begins, consuming ~ 5% of the charge. If we define "more energy stored than consumed in each cycle" or 50% efficiency as the criterion for the potential window, the potential window for diamond based supercapacitor lies between 2 and 2.5 V at a scan rate of 1 V/s in aqueous solutions.

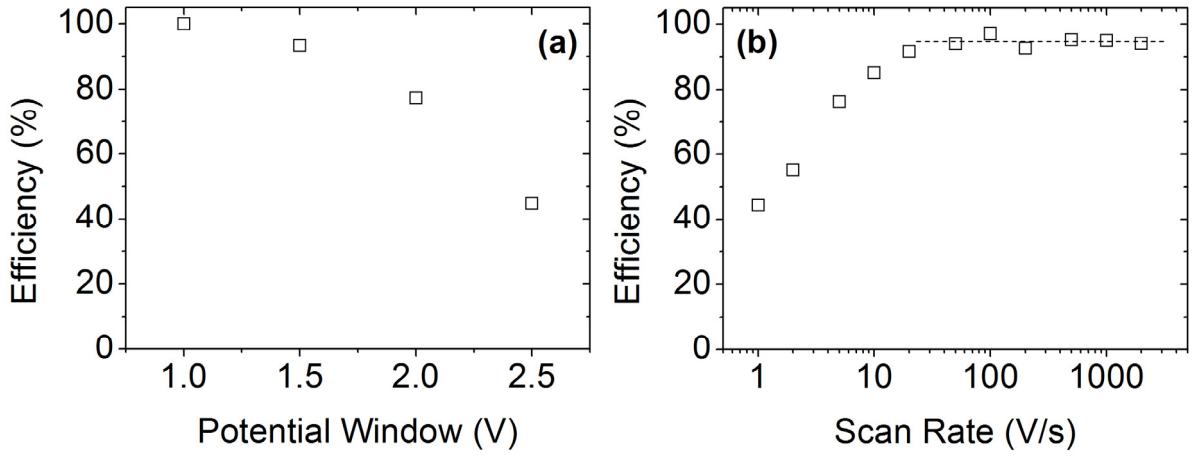

Figure 6-7: Efficiency per cycle of a diamond electrode (a) in various potential windows, (b) at various scan rates.

The dependence of efficiency on the potential window at a certain scan rate is discussed above. However, it is noteworthy that the potential window also shows dependence on scan rates. The reason for lower efficiency is water splitting which is a faradic process. Compared to capacitive charging and discharging, the Faradic electron transfer is much slower [151]. Therefore, by increasing the scan rate, the Faradic processes will be suppressed while the capacitive current will be less affected. The efficiency of a capacitor composed of two planar diamond electrodes is measured at scan rates ranging from 1 V/s up to 2000 V/s in a 2.5 V potential window. The efficiency vs scan rate is plotted in **figure 6-7 (b)**. The efficiency rises with increasing scan rate. From 20 V/s, the faradic process is almost completely stopped, and the efficiency became close to 100%.

To conclude, in sensor applications the potential window is related to the signal/background current ratio [40, 85]; in that case only the absolute value of background current is important. In a capacitor, however, the criterion of potential window is related to the efficiency of the device. Because the efficiency of a supercapacitor is related not only to the chosen potential window but also to the given operation frequency, it is impossible to set a certain potential window for every application. In general, the higher the operation frequency, the wider potential window can be used. Because diamond electrodes are highly resistive to electrochemical corrosion even at high voltages [40], high frequency applications in large potential windows may be suitable for diamond-based devices.

6.2.3 Capacitance Measurement

From cyclic voltammetry the most important value that can be obtained is probably the double layer capacitance. As is stated above, the capacitance can be calculated from **equation 6-1**. However, after we introduced the idea of efficiency, and we know that the total charge during the charging process may not be stored completely, this equation is more appropriately modified to:

$$C = \frac{Q_{discharging}}{V} \quad , \tag{6-12}$$

where V is the potential window. The capacitance values at different scan rates are summarized in **figure 6-8**.

All the samples used here are fabricated with methods and optimized conditions described in **chapter 2** and **3**. The DiaNW sample is fabricated via 3 min ICP etching. Ti nanoparticles from the thermal dewetting of a 3 nm Ti film are applied as the shadow mask. The etching parameters are the same with the sample shown in **figure 2-13**. The DiaSiW sample is fabricated via coating 15 um long silicon wires with the growth parameters shown in **table 3-1**. The DiaFoam sample consists of 5 layers of diamond hollow spheres with the growth parameters shown in **table 3-2**.

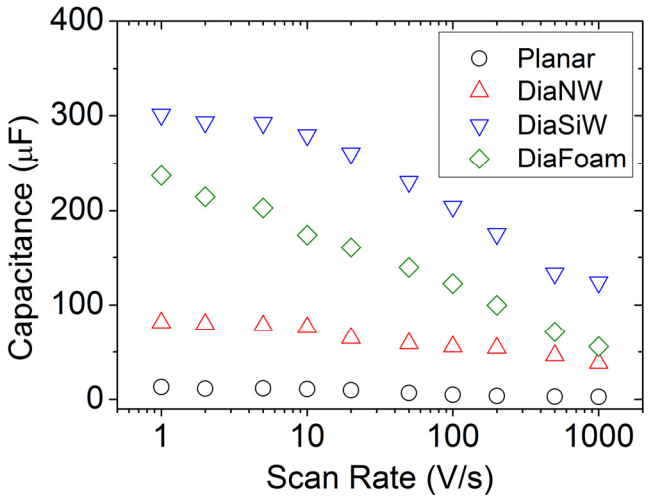

Figure 6-8: Capacitance of planar and nanostructured diamond samples measured from cyclic voltammetry in a 2.5 V window and 3 M $NaClO_4$.

For all the nanostructured samples the capacitance values are enlarged 10-40 times compared to a planar sample. The samples from templated growth show 2 – 3 times the capacitance of the DiaNW fabricated by a top-down etching method, showing the advantages of this new method developed in this work. Also, as predicted by the property of a double layer, the capacitance value decreases with increasing scan rate, which is in accordance with analysis in **section 6.1.3**. 15-μm-DiaSiW has the highest capacitance value of 301 μF at 1 V/s. However, if we take the volume into account, the DiaFoam reaches a highest volumetric capacitance of 0.46 F/cm^3, while DiaSiW only achieved 0.13 F/cm^3. This reflects that for DiaSiW electrode the active material is less compacted than in the case of DiaFoam. Although this low density leads to lower volumetric capacitance, it enhanced the rate capability of the device. For high scan rates the DiaSiW sample maintains higher capacitance values than DiaFoam: at 1000 V/s, the capacitance value is almost twice that of DiaFoam.

Capacitance values are also calculated from EIS measurements (**figure 6-9 a**). These values are very similar with the values calculated from CV measurements. However, we need to notice that at low frequencies, the capacitance of DiaFoam surpasses that of DiaSiW. To understand this difference, we need to first know that the scan rate at 1 Hz is much lower than 1 V/s. With a frequency of 1 Hz and amplitude of 10 mV, the scan rate is 2.5 mV/s. Therefore, capacitance values from impedance measurements shows that at very low frequencies, the DiaFoam electrode provides more capacitance than DiaSiW. This is in accordance with the dense packing of nanostructure in DiaFoam. Ionic movements in these structures are slowed down. Therefore, the capacitance shows high dependency on scan rate. When the frequency is sufficiently low, all the ions have enough time to be attracted to the double layer, and the capacitance value is high. When the scan rate is enhanced, however, the ions cannot follow the potential change in the porous electrode; then less electrode area is accessible to the ions, and the effective capacitance decreases. Besides slower ion diffusion, the time constant of DiaFoam is also higher than DiaSiW showing larger series resistance (**figure 6-9 b**). This may result from a thin diamond shell and lower doping concentration (as is discussed in **section 3.2.3**).

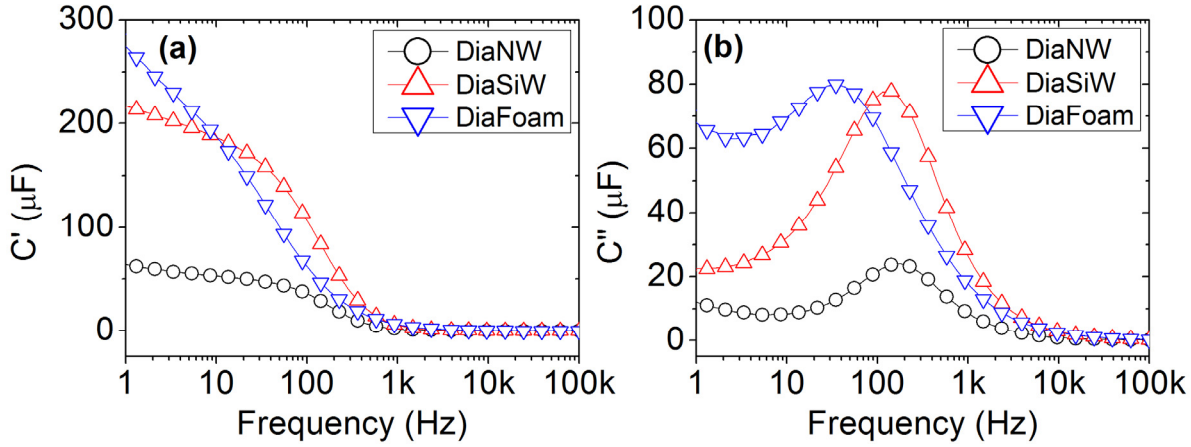

Figure 6-9: Complex capacitances calculated from electrochemistry impedance spectroscopy for nanostructured diamond samples. Relaxation times can be read from the maxima of C": for DiaNW, τ = 5.5 ms; for DiaSiW, τ = 7.0 ms; for DiaFoam, τ = 28.7 ms.

6.2.4 Energy and Power

For the final evaluation and possible application of the device, the energy and power densities are calculated with **equation 4-2** and

$$P = \frac{E}{V/v} \quad , \tag{6-13}$$

where V is the potential window and v is the scan rate. For micro-supercapacitors only the areal capacitance matters, so we calculate the areal energy and power density (**figure 6-10**). Compared to the starting point of this study, i.e. the silicon nanowire

and diamond nanowires, the performance of both diamond coated silicon wire and foam shows an obvious enhancement, with energy density approaching 0.5 mJ/cm^2 and power approaching 100 mW/cm^2. This value is comparable with the state of the art 160 mW/cm^2 achieved by onion-like-carbon [47].

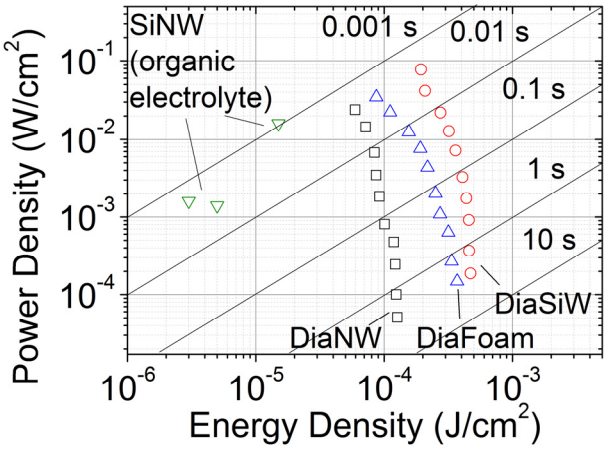

Figure 6-10: Ragone plot of nanostructured diamond samples in comparison to the literature values reported on Si nanowires; all the diamond samples show obvious improvements compared to Si based devices in terms of both energy and power densities.

From the Ragone plot we can also obtain information about possible applications of such a device. Its energy storage can be used in application with a cycle period ranging from 1 ms to 1 s. Therefore, it is suitable for high power applications where only a short pulse is needed, like the communication of wireless sensors and radio frequency identification (RFID) [47]. However, it is worth pointing out that all the nanostructured diamond materials shown here are not suitable for energy storage for two reasons. Firstly, the energy can only be stored for short periods of time. As we stated before, at potential windows larger than 1.5 V, the water has already started to split. As a result, if we hold the potential beyond 1.5 V the water will be slowly split and the potential will gradually decay to 1.23 V. In this way, the energy stored is partially lost. The only way to use high potential windows is to charge and discharge the device faster than it leaks. Therefore, diamond-based materials differ from traditional materials because they are only suitable for dynamic devices rather than static ones if a wide potential window is to be used. Secondly, practically speaking, the areal capacitance and energy density is still too small. In literature, the main stream capacitance values for double layer micro-supercapacitors are around 1-10 mF/cm^2 [47, 166], and can reach as high as 78 mF/cm^2 with the help of pseudocapacitive coatings [109, 133]. However, because of the high power performance, it is still possible to use nanostructured diamond electrode as a power booster part for a micro-supercapacitor module.

6.3 Summary and Conclusion

In this chapter, two-electrode supercapacitor devices based on diamond nanowires, diamond-coated nanowires and diamond foam are fabricated. The performance of such devices is investigated. There are three main conclusions:

1) The statement of "a large potential window of diamond" needs to be taken carefully. The definition of the potential window in supercapacitor applications is different from that in sensor applications. Diamond can be used in a potential window larger than 1.23 V, but the energy can only be stored for a short period of time and the efficiency needs to be taken into account.
2) Although diamond-based materials have small capacitance values (~ 300 μF/cm^2), the power density can reach 100 mW/cm^2 thanks to the large potential window and the use of aqueous electrolyte.
3) Based on the above two points, a practical way to use diamond for micro-supercapacitors is to use a diamond double layer capacitor as the power booster, and use another energy storage unit for the back-up power. Therefore, in the next chapter the aim will be to enhance the energy storage for diamond-based materials.

Chapter 7: Pseudocapacitor Systems Based on Diamond Nanostructures

7.1 Motivation

Due to the limitation of the surface enlargement, the diamond-based nanomaterials so far developed in this thesis achieved double layer capacitance values less than 1 mF/cm^2. Consequently, in applications where high capacitance is needed, the device area needs to be multiplied. However, making a large device goes against the purpose of this work which is micro-supercapacitors for integrated devices. Therefore, to enhance the available capacitance per unit area based on the already developed technology for diamond nanostructuring is necessary. Pseudocapacitive coating on diamond is therefore a potential solution.

Pseudocapacitors are a category of supercapacitors which use the fast and reversible surface faradic redox reactions, often from metal oxides/hydroxides [100, 105, 111, 136, 138], to enhance the energy storage [32]. In a pseudocapacitor, electrical energy is stored electrochemically rather than electrostatically (as in the case of double layer capacitors). Compared to activated carbon which provides typically 50-200 F/g capacitance [156], the specific capacitance values for pseudocapacitance materials are ~ 1000 F/g, and in some cases as high as ~ 2500 F/g [106, 127]. Taking into account the already small specific capacitance of diamond (~ 10 F/g [10]), magnitudes higher capacitance can be expected with just a thin layer of pseudocapacitive coating.

Despite the large energy storage (10-100 Wh/kg), pseudocapacitive materials deliver the energy slowly, which leads to a small power capability of 1-10 kW/kg [111, 113, 124], due to the poor conductivity of the metal oxide and slow ion diffusion in the porous material. This chapter is devoted mainly to achieving higher power density (up to 100 kW/kg) while maintaining the state of art energy capability.

7.2 Pt-Diamond System

7.2.1 Concept

The rate capability of pseudocapacitive electrodes is limited by the reaction kinetics and conductivity of the active materials [100]. By careful examination of the redox reactions used in pseudocapacitors, it is easy to find that the reaction with water is often involved [120, 128, 137], i.e. the reactions involves either H^+ or OH^- depending on the pH of the electrolyte used. Therefore, if a pseudocapacitance material has a fast reaction with H^+/OH^-, the rate performances will also be enhanced.

To enhance the reaction rate, the use of platinum is a potential solution, because platinum-related materials have been implemented as efficient catalysts for hydrogen/oxygen evolution [167]. The hydrogen adsorption/desorption and surface oxida-

tion/reduction is known and studied for over half a century [168, 169]. Compared to metal oxide materials which only display oxidation/reduction, hydrogen-related faradic reaction is unique to platinum, and will also contribute to pseudocapacitance. However, unlike the porous metal oxides, the redox reaction will only happen on Pt surface rather than in bulk platinum [151]. Therefore, a thick Pt layer will in principal not enhance the capacitance. Therefore, a feasible approach is to deposit a thin layer of Pt over a large area. A highly conductive nanostructured material is preferred.

In order to enhance the conductivity as well as surface area of a pseudocapacitive material, conductive nanomaterials, such as graphene nanosheet [100], carbon nanotubes [134], silicon nanowires [112], and nanostructured metals [106, 141], are often used as current collectors inside the semiconductive materials. However, to the best knowledge of the author, to charge/discharge pseudocapacitors at scan rates higher than 500 mV/s has not been reported.

In this chapter, the speed of a pseudocapacitor is enhanced from two aspects: 1) using the fast catalytic reactions between Pt and water, i.e.

$$\mathrm{Pt} + x\mathrm{H_2}0 + x\mathrm{e} \leftrightarrow \mathrm{PtH}_x + x\mathrm{OH}^- \tag{7-1}$$

and

$$\mathrm{Pt} + x\mathrm{H_2}0 \leftrightarrow \mathrm{PtO}_x + 2x\mathrm{H}^+ + 2x\mathrm{e}^- \tag{7-2}$$

to enhance the charging/discharging kinetics, 2) using highly conductive BDD nanowires as a surface-enlarged current collector. The concept is to use the fast surface oxidation/reduction together with hydrogen desorption/adsorption of Pt to provide pseudocapacitance with fast kinetics. Moreover, with the combination of Pt and BDD, the surface area of such a composite material is expected to be high.

For the fabrication of common pseudocapacitor electrodes, be it metal oxides or conductive polymers, electrochemical deposition is frequently used [104, 106, 118, 170]. However, in the case of coating on diamond nanowires, the method is not suitable for the following reasons.

1) It is difficult to obtain a uniform coating. The pseudocapacitive behavior of Pt is a surface phenomenon; therefore, a thick coating will not improve the performance, but waste material. In the case of diamond nanowires, because electrodeposition is a diffusion controlled process [171, 172], only the tops of the wires will be covered, resulting in a non-uniform coverage.
2) Reproducibility is very sample dependent. For example, different wire thicknesses and densities will result in different conductivities of individual wires as well as different diffusion profiles surrounding each wire. These effects will lead to poor reproducibility of the Pt coverage.

From the results of **chapter 2**, the diamond wires have tapered shapes with sharp tips. Therefore, the entire surfaces are accessible to vertical deposition flux. Therefore, in this chapter a physical deposition method, i.e. sputtering, is applied to achieve uniform and reproducible metal coverage on diamond nanowires. Experimentally, diamond nanowires are fabricated using redeposition-enhanced etching parameters (1200 W ICP power, 300 W HF power, O_2 pressure 3 Pa). The surface enlargement factor is calculated via cyclic voltammetry as 19.2 times (as is measured in **chapter 2**). Nominal thicknesses of 20, 40 and 60 nm are deposited on the diamond wires, and they are named as PtDia20, PtDia40 and PtDia60, respectively. These electrode samples are characterized by SEM and electrochemical techniques.

7.2.2 Results and Discussion

Figure 7-1 (a) shows the SEM images of diamond nanowires. The wires have tapered shapes which are preferred for achieving a high sputtering coverage. For the sample with 20 nm Pt deposition (PtDia20) (**figure 7-1 b**) the surface of the wires becomes rough, showing metal coverage. As more Pt is deposited (**figure 7-1 c** and **d**) the wires grow thicker and become corrugated nanorods. It is observed that as the metal layers thicken the spaces between wires are filled by Pt and neighboring wires start to

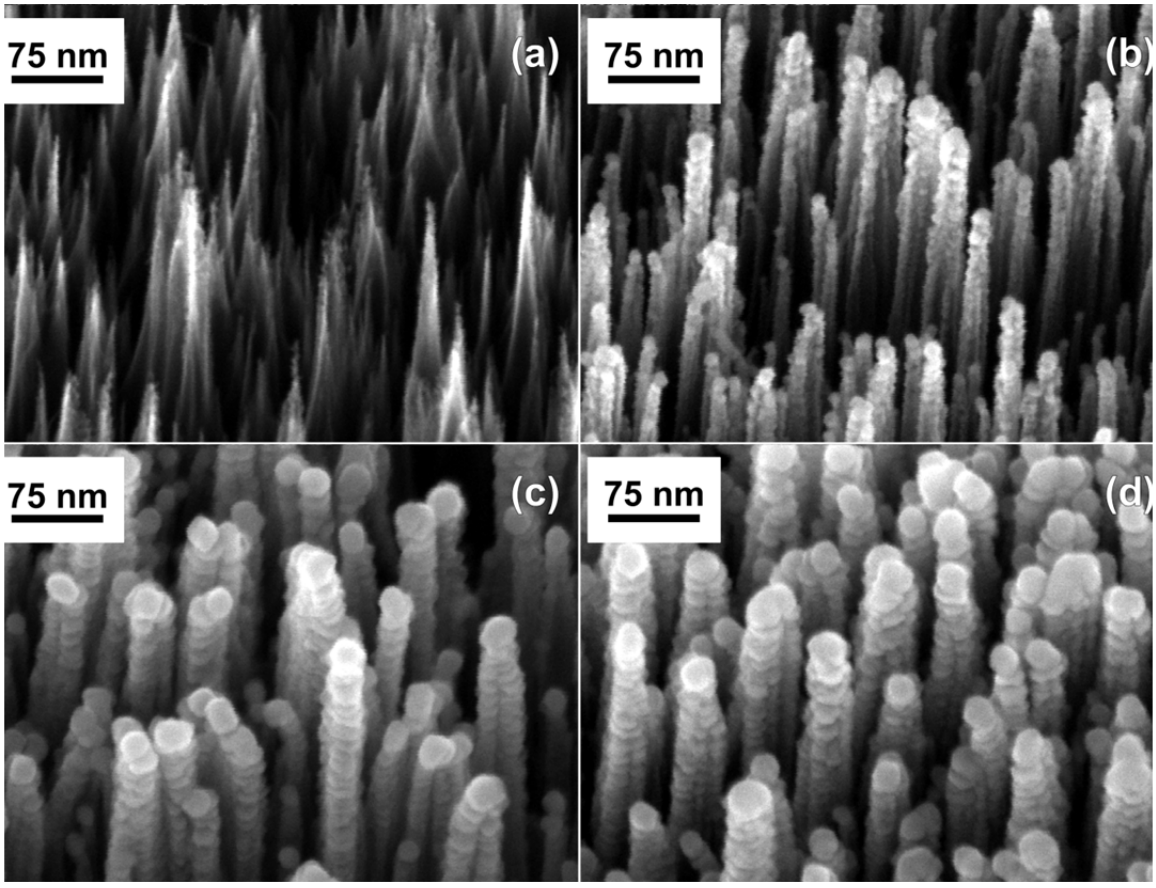

Figure 7-1: SEM images of vertically aligned diamond nanowires (30˚tilting angle) (a) and Pt-diamond core-shell wires, PtDia20 (b), PtDia40 (c), and PtDia60 (d).

agglomerate. Therefore, the metal thickness needs to be optimized.

In order to find out the optimized Pt thickness for the largest capacitance, cyclic voltammetry in a potential window of 1.2 V was performed with scan rates from 20 mV/s to 2 V/s. The results for PtDia40 are shown in **figure 7-2 (a)** as an example. For the investigated scan rates, typical platinum behaviors were recorded. Hydrogen adsorption/desorption happened at potentials lower than 0.2 V while Pt surface oxidation happened from 0.6 V to 1.0 V. The surface reduction appeared as a broad peak from 0.9 to 0.1 V. The double peak for hydrogen adsorption/desorption shows the reaction at different crystal surfaces [169].

The capacitance values can be calculated with [118]:

$$C = \frac{\int I(V)dV}{2\Delta V v} \quad , \tag{7-3}$$

where I is the current density, v is the scan rate and ΔV is the potential window. The calculated results are shown in **figure 7-2 (b)**. As expected, the capacitance value shows a dependence on the amount of Pt coating. At a scan rate of 20 mV/s, the PtDia40 sample shows a specific capacitance of 11.1 mF/cm^2, which is about twice the capacitance value of PtDia20. However, the capacitance values of PtDia60 are slightly smaller than PtDia40.

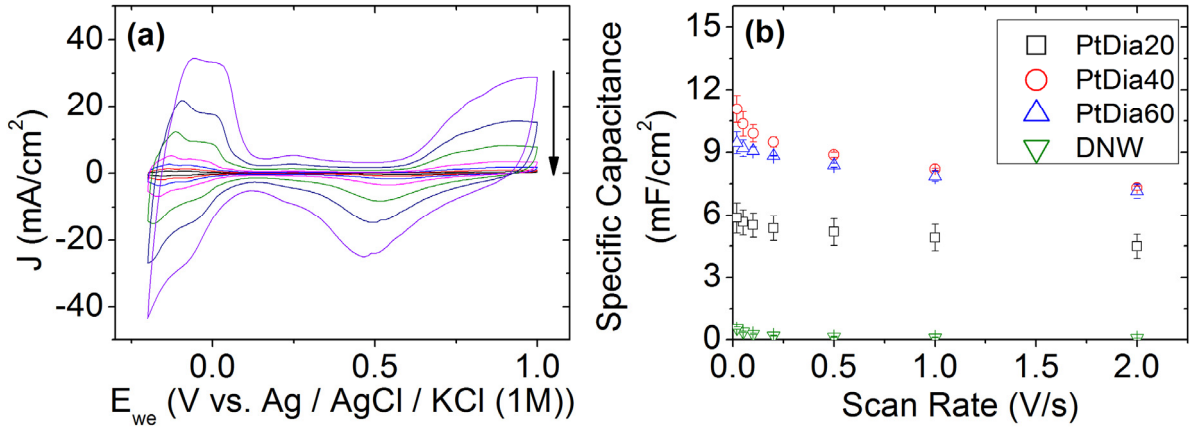

Figure 7-2: (a) Cyclic voltammetry of a PtDia40 sample between -0.2 and 1.0 V vs Ag/AgCl (1 M KCl) in 2 M H_2SO_4 at 2000, 1000, 500, 200, 100, 50, 20 mV/s; scan rate decreases along the direction of the arrow. (b) Specific capacitances calculated from cyclic voltammetry for PtDia20, PtDia40 and PtDia60 at different scan rates; DNW stands for the bare diamond nanowire sample.

To ascertain if the change in the capacitance with different coating thicknesses is a result of the increasing Pt coverage or Pt thickness, planar Pt samples with different thicknesses were investigated. First, the specific capacitances of planar BDD samples with 1, 2, 3 and 5 nm Pt coatings were calculated from cyclic voltammetry (the same as shown in **figure 7-2 a**). The results are shown in **figure 7-3 (a)**. The specific capacitance of Pt is about 0.5 mF/cm^2 and does not vary significantly with Pt thickness.

Therefore, the change in the capacitance is not a result of the changing thickness but the changing coverage of Pt coating.

The Pt surface area can be calculated from the charge of hydrogen desorption peaks (Q_H) in cyclic voltammetry divided by a standard value of 0.21 mC/cm^2 [173]. As we know the surface enlargement factor (F = 19.2) and the geometric electrode area (A_G) of the diamond nanowire sample, the Pt coverage can be obtained using:

$$Coverage = \frac{Q_H/0.21}{A_G \times F} \times 100\% \quad , \tag{7-4}$$

The coverages of different samples were calculated and plotted in **figure 7-3 (b)**. The coverage increases linearly with Pt amount until a saturation of 82% is reached after 40 nm Pt deposition. This result is in accordance with **figure 7-2 (b)**. When the Pt amount is low (20 nm), the lower part of nanowires is not fully covered because the bottom is less available to the deposition flux. This non-uniformity is also seen when sputtering is used to coat high-aspect-ratio features, the top of the side-wall is thicker than the bottom [174].

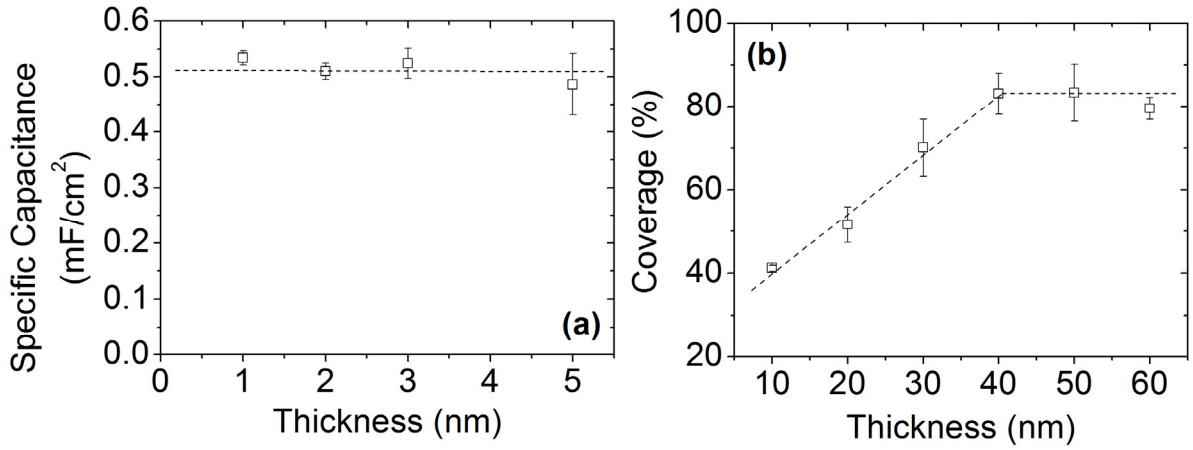

Figure 7-3: (a) Specific capacitance of planar Pt films of different thickness calculated from CV curves between -0.2 and 1.0 V vs Ag/AgCl (1 M KCl) in 2 M H_2SO_4 at 100 mV/s with **equation 7-3**; (b) calculated Pt coverage a function of different Pt deposition thickness.

As is indicated by the results here, further increasing the Pt deposition above 40 nm does not further enhances the total Pt surface area, which again confirms that excessive metal just enhance the thickness of the coating which does not change the total capacitance, as is shown in **figure 7-3 (a)**. This explains why the PtDia40 and PtDia60 have similar capacitances (**figure 7-2 b**). Also, one side effect of a thick coating is the wire coalescence. When the coating on the sidewall grows too thick, the inter-wire space will be completely closed, which results in one thick coalesced wire. This phenomenon is very similar to trench filling in microelectronics processing when a thick metal layer is deposited [175].

The capability of Pt-coated electrode for fast charging/discharging is evaluated by comparing capacitance values at different scan rates. When the scan rate increases 100 times from 20 mV/s to 2 V/s the capacitance only decreases 23.4%, 34.0% and 24.3% for PtDia20, PtDia40 and PtDia60, respectively. This rate capability surpasses all the pseudocapacitive materials summarized in **table 7-1**, confirming the concept of using catalytic reaction to enhance the device speed.

Material	Reported Scan Rates ($mV\ s^{-1}$)	Capacitance Loss	Ref.
Ni Oxide Nanosheet	5 to 40	34%	[113]
NiO_x	2 to 20	32%	[124]
$Ni(OH)_2$/Graphene	2 to 20	59%	[127]
Ni-Co Oxide Nanosheet	5 to 20	37%	[119]
Nanoporous NiO	1 to 100	77%	[118]
MnO_2/Graphene	2 to 100	45%	[132]
Pt/diamond Nanowire	20 to 2000	23%	PtDia20

Table 7-1: Summary of rate capabilities of pseudocapacitive materials in previous literature in comparison to the PtDia20 sample.

With the capacitance values calculated from CV measurements, a gravimetric capacitance as high as 109 F/g is obtained from PtDia20 sample. It is difficult to compare with other materials, because in current literature scan rates higher than 100 mV/s are seldom used for pseudocapacitor characterization. However, even compared to the capacitance values obtained at much lower scan rates, a capacitance value between 100 and 200 F/g is still comparable with or even higher than less conventional materials like Fe_3O_4 [138] and MoO_3 [111]. Although the capacitances at lower charging currents/scan rates are lower than conventional pseudocapacitance materials like nickel hydroxide [100], cobalt oxide [128] and manganese dioxide [139], at high charging currents/scan rates this situation might change, because the capacitance values for metal oxides decrease quickly with increasing cycling rates.

To conclude, the highlight of this section is the introduction of catalytic reactions in pseudocapacitive systems. With Pt coating the concept of using diamond nanowires as 3D current collector for pseudocapacitive materials is proven. More than one magnitude enhancement in areal capacitance (to ~ 10 mF/cm^2) together with fast charging/discharging performance is achieved after a thin layer of Pt coating.

However, a Pt-based capacitor has several drawbacks:

1) The total capacitance is still limited because the catalytic reaction can only happen at the surface (as is shown in **figure 7-3**); i.e. the atoms which are not on the surface are wasted.
2) Many metals like nickel or cobalt have porous hydroxides which provide large surface area after oxidation. However, platinum is inert, and it does not provide more surface area after oxidation. This also limits the area capacitance.

3) Platinum is a heavy metal (21.5 g/cm^3, which is ~ 6 times the density of diamond, more than twice the density of nickel), and the gravimetric capacitance value (F/g) is thus limited.
4) Platinum is expensive. Large quantity use is not welcome in industry.

Therefore, in the next section, a substitute material is considered.

7.3 Nickel-Diamond System

7.3.1 Concept

As a result of the drawbacks summarized in the last section, it is necessary to consider other pseudocapacitive metals as a coating for diamond nanowires. As a pseudocapacitance material, nickel hydroxides and their composites are widely investigated because of their low cost and high theoretical capacitance of > 2000 F/g [37, 116, 118, 119, 126, 132, 135, 140, 141]. The conversion of different phase of nickel hydroxides follows the scheme in **figure 7-4** described by Bode *et al* [176]. The conversion between β (II) and β (III) phases is the normal type during charging and discharging [177].

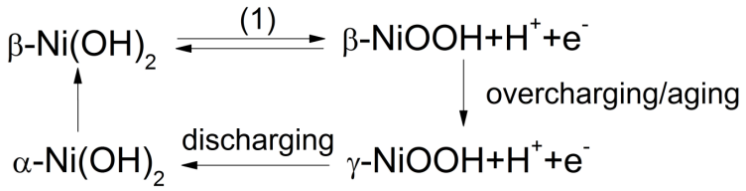

Figure 7-4: Conversions between Ni(II) and Ni(III) hydroxides.

Compared to Pt, Ni is not only cheaper and lighter. One important feature of Ni which Pt misses is the high porosity of its hydroxides. If a thin Ni coating on diamond nanowire is electrochemically oxidized to $Ni(OH)_2$/NiOOH, the total surface area will further increase. Therefore, Ni is very interesting for the purpose of enhancing area capacitance (F/cm^2) for diamond-based pseudocapacitors.

7.3.2 Results and Discussion

Using the same method described in the **section 7.2**, diamond nanowires were coated with nominal thicknesses of 20, 40 and 60 nm of Ni. These samples are named as NiDia20, NiDia40 and NiDia60, respectively. After sputtering, metallic Ni is converted to $Ni(OH)_2$ in NaOH solution to be [141]. The SEM images of the metal coated diamond nanowires are shown in **figure 7-5 (a), (c) and (e)**. Similar to the Pt coating, the core-shell wires become corrugated when the metal coating is thicker than 20 nm. Also, with thicker Ni coating, adjacent wires start to agglomerate. However, unlike Pt which is stable after oxidation, Ni will become nickel hydroxide after anodization as is shown in **figure 7-5 (b), (d) and (f)**. The volume of the coating increases, showing fibrous structures surrounding the wires. The inter-wire space is taken up by the highly porous hydroxide. The $Ni(OH)_2$ phase resulted from anodization was previously reported to be α-$Ni(OH)_2$ [141]. However, because α-$Ni(OH)_2$ is not stable in alkaline solution, it will

automatically transform to β-$Ni(OH)_2$ [178]. Therefore, we expected the porous coating to be β-$Ni(OH)_2$.

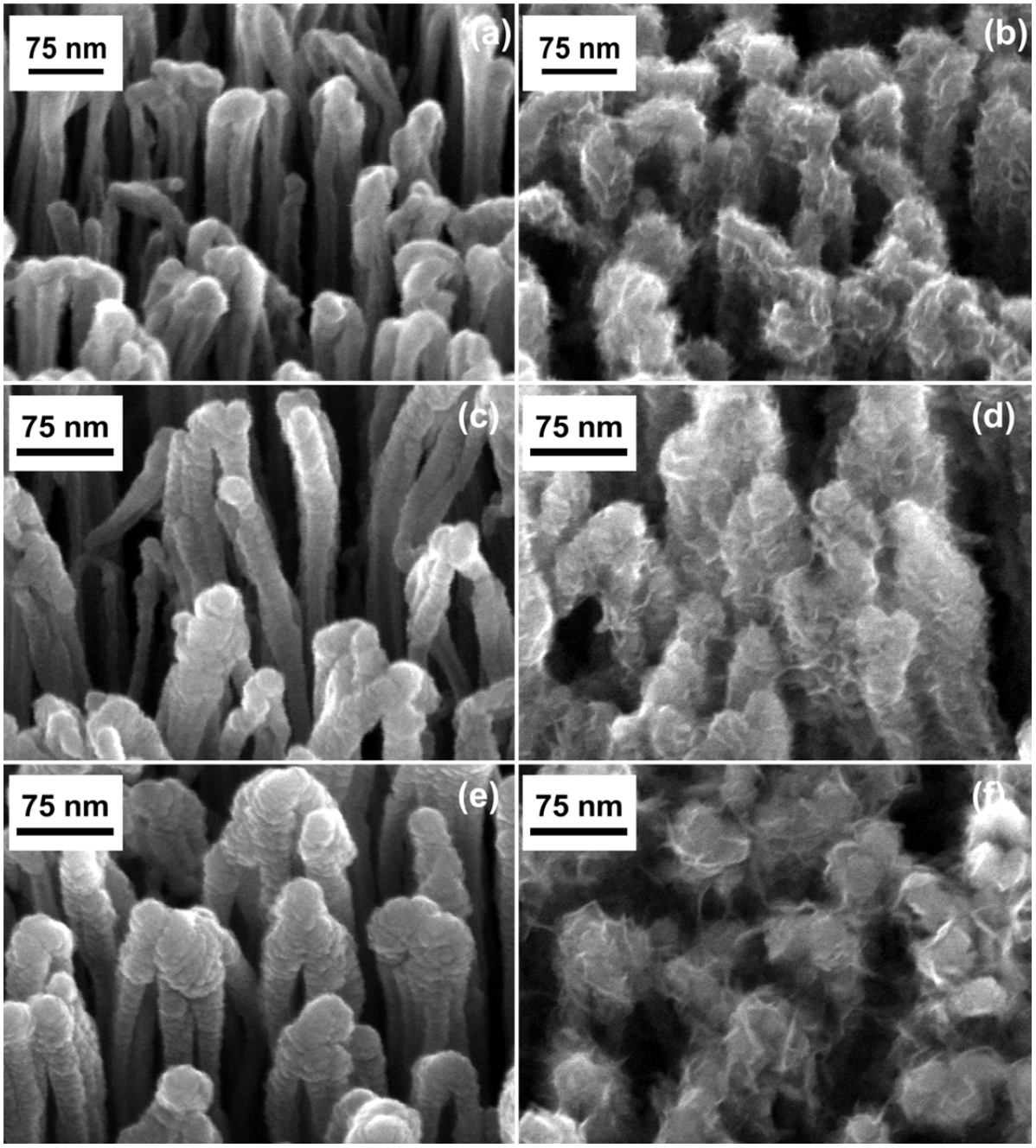

Figure 7-5: SEM images of NiDia20 (a, b), NiDia40 (c, d) and NiDia40 (e, f) before (a, c, e) and after (b, d, f) anodization; the anodization was performed via cyclic voltammetry in 3 M NaOH solution between 0-0.5 V vs. Ag/AgCl (1 M KCl) reference electrode for 20 cycles.

The cyclic voltammogram of NiDia20 at different scan rates are shown in **figure 7-6 (a)** as an example. The characteristic redox couple centered at ~ 0.3 V vs reference electrode results from the **reaction (1)** in **figure 7-4**. The areal capacitance was calculated

from the integration of CV curves (**equation 7-3**). The calculated results are shown in **figure 7-6 (b)**. The areal capacitance increased with thicker nickel coating as a result of larger amount of functional material. The highest capacitance of 91 mF/cm^2 was reached by the 60 nm Ni coating. The highest gravitational capacitance is achieved by NiDia20, being 1601 F/g which is 76.9% of the theoretical value [118]. The specific capacitance will decrease as the scan rate or discharging rate increases. The reason is twofold. On the one hand, the higher the discharging rate, the less time the diffusing species (namely, H^+) in the electrolyte have to move into the porous electrode and to be stored in the functional layer [100]. This will result in not fully charged cycles. On the other hand, high discharging rates lead to large current through the weakly conductive porous hydroxide layers. As a result, the potential drop on the functional material will increase and the actually potential of the device (between the two electrodes) will decrease. This will also reduce the charge storage in each charging-discharging cycle. However, for this material the decreasing trend is much less than the other Ni-based pseudocapacitive materials summarized in **table 7-1**, which shows the good conductivity of the core-shell wires and the good permeability of the ions in the 3D porous network.

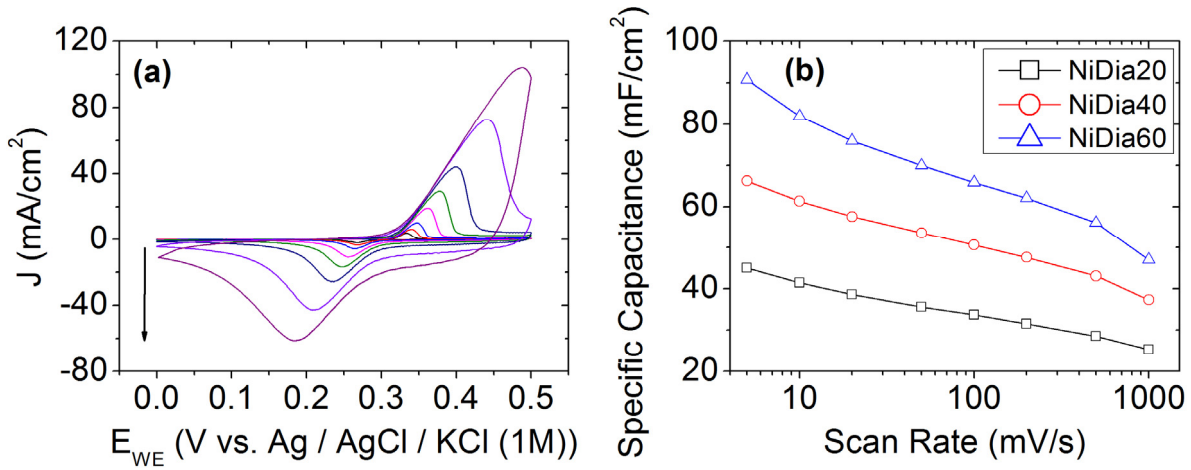

Figure 7-6: (a) Cyclic voltammetry of NiDia20 sample between 0-0.5 V at 5, 10, 20, 50, 100, 200, 500, 1000, 2000 mV/s (scan rates increase along the arrow direction); (b) areal capacitance vs scan rate for vairous samples.

The ability of the diamond-Ni(OH)$_2$ core-shell nanowires for fast charging/discharging is supported by the kinetics of the redox reaction of Ni(OH)$_2$. The kinetics of the redox reaction can be evaluated with the peak separation of the anodic and cathodic peaks ΔE_p [151]. Comparing our results with the values shown in the literature, we find that at 100 mV/s the smallest report peak separation for Ni(OH)$_2$ is 340 mV [141], which is about three times our value (130 mV). In fact, for the capacitance tests concerning Ni(OH)$_2$, typical scan rates used in CV are usually smaller than 100 mV/s (typically up to 40 mV/s) [100, 126, 127]. Even at these low scan rates, ΔE_p is above 300 mV. Therefore, our core-shell structure facilitated the electron transfer process on Ni(OH)$_2$.

To find out a physical explanation for the fast electron transfer kinetics, cathodic and anodic peak potentials at different scan rates are plotted in **figure 7-7** for different coating thicknesses. It is observed that the peak separation increases with increasing scan rates, which is typical for quasi-reversible reactions with a slow electron transfer rate [151]. Because nickel hydroxide and oxy-hydroxide are highly amorphous and poorly conductive [100, 117], the wide peak separation with thicker coating probably results from a thicker non-conductive layer and thus larger charge transfer resistance. The anodic peak position shows a weaker dependence on the coating thicknesses than the cathodic one. The reason for a change in peak position can be complex and related to local change in material conductivity, composition and ion concentration in the solution [177, 179]. However, a simple explanation can be deduced from the reaction mechanism of **reaction (1)** in **figure 7-4**: when NiOOH is reduced to $Ni(OH)_2$ one proton and one electron per Ni atom is intercalated into the β(III) phase [179]. Therefore, in an alkaline solution under positive bias this process is limited by H^+ diffusion (low H^+ concentration), and this process will become more and more difficult as the coatings become thicker. The oxidation of β(II) phase, however, is a H^+ removal process which is less affected by the high pH.

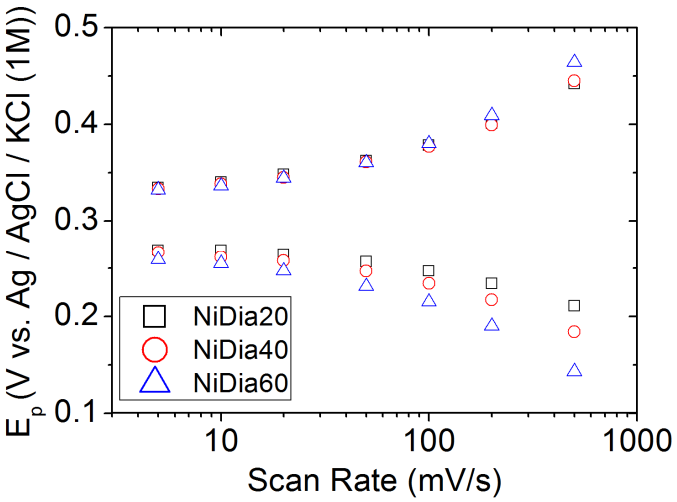

Figure 7-7: Anodic and cathodic peak position vs scan rate for NiDia20/40/60 samples.

A high charging/discharging rate leads to high power densities. The energy and power can be calculated by:

$$E = \frac{C\Delta V^2}{2} \tag{6-5}$$

and

$$P = \frac{E}{\Delta t} \quad . \tag{6-6}$$

The results are plotted in **figure 7-8**. For state-of-the-art pseudocapacitive materials, the energy density lies between 10-100 Wh/kg, and the power density is limited to 10^4 W/kg. Compared with these data, the highest power densities of the Ni-coated diamond nanowires are over one order of magnitude higher, while their energy densities are comparable to the present main stream values [113, 119, 124, 127, 139].

When micro-supercapacitors are considered, areal energy and power is more important. For NiDia60 sample, the energy density reaches 5.69 mJ/cm^2. Please note that this value is measured with a three electrode set-up. In a real device, which should be two-electrode, this value will decrease to only half, i.e. 2.85 mJ/cm^2. From the result of the last chapter, the DiaSiW has an energy density of 0.47 mJ/cm^2; NiDia60 has a 500% increase in energy storage.

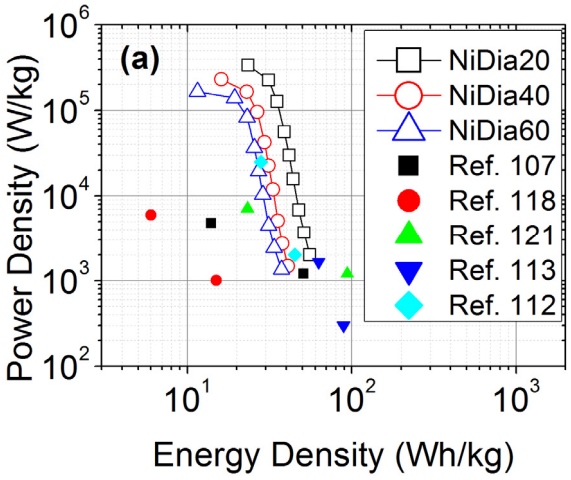

Figure 7-8: Ragone plot of different samples in comparison with data from other literature.

7.4 Summary and Conclusion

In this chapter, pseudocapacitive coating is deposited on diamond nanowires to enhance the areal capacitance. Both platinum metal and nickel hydroxide show suitability for the coating. For the platinum coating, the operation speed is enhanced by the catalytic surface adsorption of hydrogen and oxygen. For nickel hydroxide, the diamond nanowires enhanced electron transfer kinetics. As a result, for both kinds of coatings, the charging and discharging rate can reach 1 V/s which is one magnitude higher than the typical rates reported in literature.

As is pointed out in the beginning of this chapter, the aim is to enhance the area capacitance of diamond-based supercapacitor with the present surface enlargement technology. The results show that after coating, the capacitance value was enhanced from ~ 100 μF/cm^2 to ~ 100 mF/cm^2, and the energy storage is enhanced 5 times from that of diamond-based double layer capacitors.

As far as the the cell design of a pseudocapacitor is concerned, the symmetric cell design as in the case of a double layer capacitor will not work. The reason is that when

one electrode is charged to positive potential the other electrode potential must be negative. That is to say when, for example, a $Ni(OH)_2$ electrode is working in the potential of 0 – 0.5 V where the surface redox reaction happens, the counter electrode must work at -0.5 – 0 V where there is no redox behavior. As a result, the capacitance of the counter electrode will be much smaller than the other. As the capacitance of a supercapacitor is limited by the smaller electrode, the total capacitance will be limited.

A realistic design is an asymmetric cell, with the anode being a large surface area double layer electrode (e.g. activated carbon), and the cathode being a pseudocapacitive electrode [142]. During the charging-discharging processes, the pseudocapacitive electrode will always work in the positive potentials, and the negative potentials are made up by the double layer electrode.

However, in the realization of such designs in diamond-based devices lies a technical difficulty. We know from this chapter that the typical value for a Ni-coated diamond electrode is ~100 mF/cm^2. In order to form an asymmetric cell the diamond double layer electrode serving as a counter electrode should also have more or less the same capacitance. From **chapter 3**, we know that 5-layer diamond foam has a capacitance of ~ 0.5 mF/cm^2 and a DiaSiW with density of 3×10^8 cm^{-2} and a length of 5 μm has ~ 0.1 mF/cm^2. Therefore, to reach a capacitance of 50 mF/cm^2, 1000-layer foam or 100 times denser and 10 times longer (50 μm) Si nanowires are needed. Based on current technology, however, further effort is needed to fulfill these requirements.

Chapter 8: Diamond-Based Materials for Energy Conversion

The energy storage and conversion lie in the core of nowadays energy issues. In the previous chapters of this thesis, supercapacitors based on diamond materials have been thoroughly investigated, and interesting results are obtained. In order to enlighten possible future research topics, nanostructured diamond materials developed in this thesis will be applied for energy conversion in this chapter.

About the electrochemical energy conversion, the following two topics are of interest:

1) The conversion of an electrical energy into a chemical one. One example of this type of application is to use the excessive energy from wind or solar energy to split water. The products, i.e. H_2 and O_2 can be used in other applications or recombined to again give out energy.
2) The conversion of a chemical energy into an electrical one. This conversion is often realized via fuel cells, in which the fuels, such as H_2, Methanol, and $NaBH_4$, are oxidized and generate electricity without combustion.

For both the fuel cells and water splitting, the electrocatalyst is an indispensable part. The performance of a catalytic electrode will be closely related to its active surface area. Therefore, surface-enlarged electrodes developed in this thesis will also be helpful in these two topics.

The combination of metal catalysts nanoparticles(e.g. platinum, gold, palladium, copper, and their alloys) and sp^2 carbon based materials, such as carbon nanotube, carbon black, activated carbon and graphene has been applied as a popular system for electrocatalysis [180-186]. While providing large surface area, these materials have less stability compared to diamond (i.e. sp^3 carbon), especially in case of oxidation [40, 139]. Therefore, diamond has been proposed as an alternative support for electrocatalysis. Planar BDD electrode, for instance, has been widely used as a support for Pt nanoparticles for catalytic oxidation of liquid fuels (e.g. methanol, ethanol) and oxidation of carbon monoxide as well as for other catalytic reactions like hydrogen evolution and oxygen reduction [180, 183, 185, 187-189]. However, even by fully covering a planar electrode with a dense layer of semispherical nanoparticles, the active area enlargement is still limited to a geometric factor of ~ 4. As a result, nanostructured diamond can be applied. In this chapter, both planar and nanostrucured diamond electrodes will be use as solid support for Pt catalyst to challenge the commercial Pt-Carbon catalyst.

8.1 Diamond Electrodes Decorated with Platinum Nanoparticles

To deposit uniform Pt nanoparticles on diamond, the thermal de-wetting introduced in **chapter 3** is a fast and convenient method. It is also compatible to cleanroom technologies and suitable for mass production. However, this method has two drawbacks:

1) the de-wetting can only happen if the thickness of the metal layer is very thin, usually less than 4 nm (**figure 8-1 a**); 2) during the de-wetting, the molten metal can etching diamond surface, resulting in either etch pits or carbide forming [190, 191] (**figure 8-1 b**). Therefore, a non-destructive electrochemical metal deposition technology is preferred.

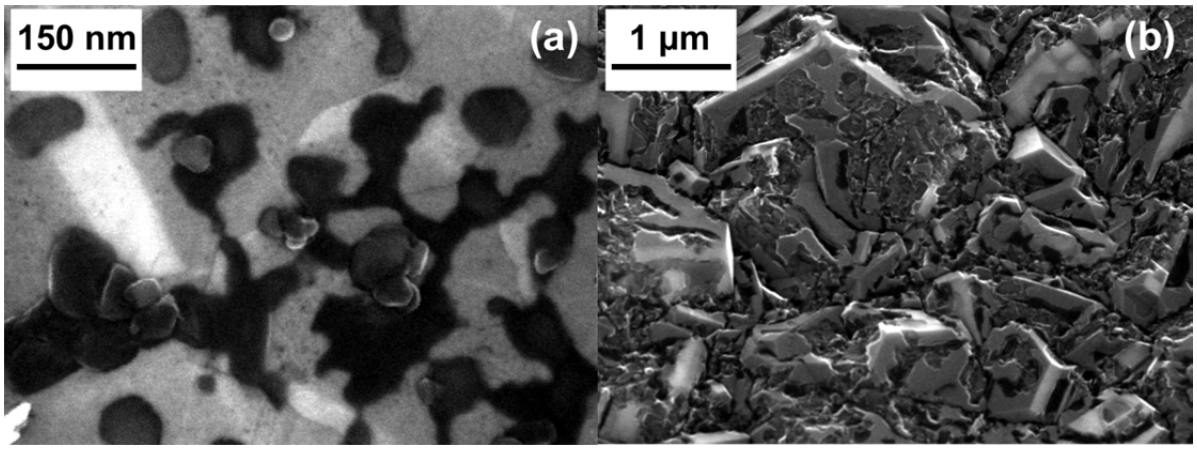

Figure 8-1: (a) 5 nm thick Ni film after de-wetting; (b) the same sample after Ni removal in 1:3 mixture of HNO_3 and H_2SO_4 at 250 °C.

Electrochemical deposition is a method using electrical current to reduce dissolved metal ions to metal nanoparticles [180, 183, 186, 187, 192-195]. However, same as most of chemical reactions, the deposition needs to overcome an activation barrier. Therefore, the nucleation will choose to happen at energetically favored sites such as local defects and grain boundaries. Because of the limited nucleation sites, the resulting particle density is low. If the particles are used as etching masks, a low particle density will lead to a low wire density and thus a lower surface enlargement. Therefore, methods to enhance the nucleation density are necessary.

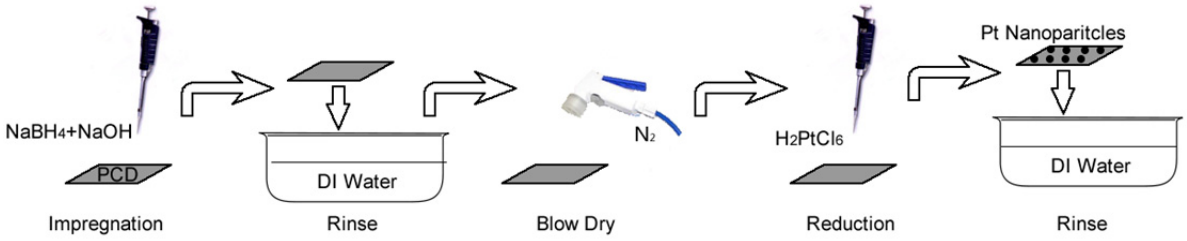

Figure 8-2: Schematic drawing of the wet-chemical seeding procedures.

The origin of this non-uniform nucleation comes from the different conductivity between grain boundaries and grains. Therefore, a non-electrochemical seeding method might solve this problem. In this seeding technique, 25 µL 1.0 M $NaBH_4$ in 0.1 M NaOH solution was first dropped onto a clean diamond for the adsorption of $NaBH_4$. The electrode was then rinsed with water and blow dried with N_2 to remove excessive

$NaBH_4$. The formation of Pt nanoparticles was done by adding 25 µL 1.0 mM H_2PtCl_6 solution onto the electrodes. After that, the electrode was again cleaned with water and blown dry with N_2 (**figure 8-2**). It is believed that a certain amount of reductant adsorbing on the electrode surface will reduce the Pt precursor (H_2PtCl_6) and form a high density uniform Pt nanoparticle layer on the surface (**formula 8-1**) [147]:

$$BH_4^- + 3OH^- + PtCl_6^{2-} \rightarrow Pt + 6Cl^- + H_3BO_3 + 2H_2 \uparrow \quad . \tag{8-1}$$

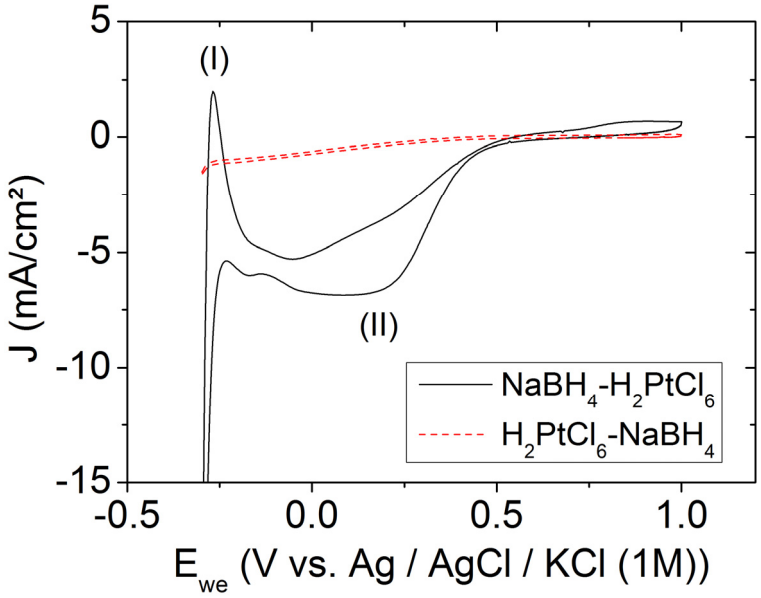

Figure 8-3: Cyclic voltammogram of a diamond electrode in 0.1 M H_2SO_4 solution at a scan rate of 100 mV/s; red dotted curve: H_2PtCl_6 was added before $NaBH_4$; black solid curve: in the reverse sequence.

In order to investigate the seeding mechanism two seeding experiments was performed. In the first experiment, H_2PtCl_6 solution was dropped onto the diamond electrode before adding $NaBH_4$; in the second experiment, the sequence was the opposite. In both experiments, seeding was performed only once. The existence of Pt on these two diamond electrodes was examined via cyclic voltammetry (**Figure 8-3**)**.** For the first electrode, the CV curve (red dotted curve) is featureless, showing no Pt deposition. For the second electrode which is first exposed to $NaBH_4$, the cyclic voltammogram (black solid curve) shows clearly Pt signal: an oxidation peak (I) which corresponds to oxygen reduction [196] and an oxidation peak (II) which indicates to hydrogen desorption from Pt surface [193, 197]. This suggests that in order to form Pt particles in this seeding process, the electrode should be exposed to $NaBH_4$ first. Therefore, the adsorption of $NaBH_4$ on the diamond surface leads to the generation of Pt seeds. The mechanism of this specific adsorption is however, not yet very clear. It is believed to be related to the surface termination of diamond. **Figure 8-4** shows the result of seeding on H- and O-terminated diamond, respectively. The H-terminated surface shows obviously better seeding effect. Presumably, the slightly positively charged H-terminated surface exhibits a higher affinity to the negatively charged BH_4^- ion.

Because this seeding is based on the specific adsorption of BH_4^- ion on diamond surface, it is expected to be applicable for the deposition of other metal nanoparticles on diamond electrode. As far as a metal ion can be reduced by $NaBH_4$ to metal, it can be deposited on diamond using the wet-chemical seeding method. As a proof of concept, we investigated the deposition of Ni, Au and Cu by replacing 1.0 mM H_2PtCl_6 with1.0 M $NiSO_4$, 2.4 mM $HAuCl_4$, or 10 mM $CuSO_4$. **Figure 8-5** provides SEM images of Au (a), Cu (b), and Ni (c) nanoparticles seeded on H-terminated diamond surfaces. As is observed in the images, homogenously distributed nanoparticles are detected on the diamond surface. Therefore, the wet-chemical seeding method proposed here is a universal metal deposition method on diamond surfaces.

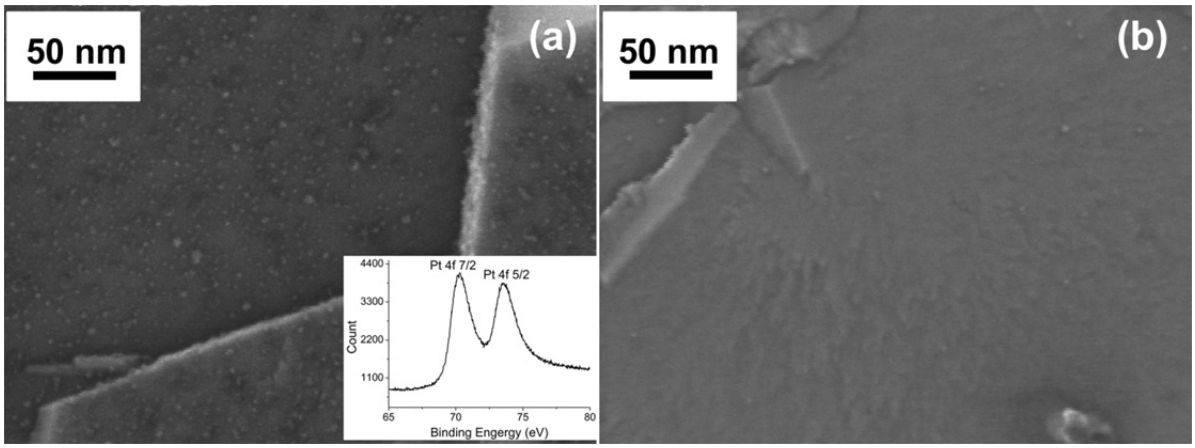

Figure 8-4: SEM images of Pt particles on (a) H-terminated and (b) O-terminated diamond surface. The samples were prepared using the procedure only with once seeding process; the inset of (a) is an XPS spectrum of the sample showing Pt deposition.

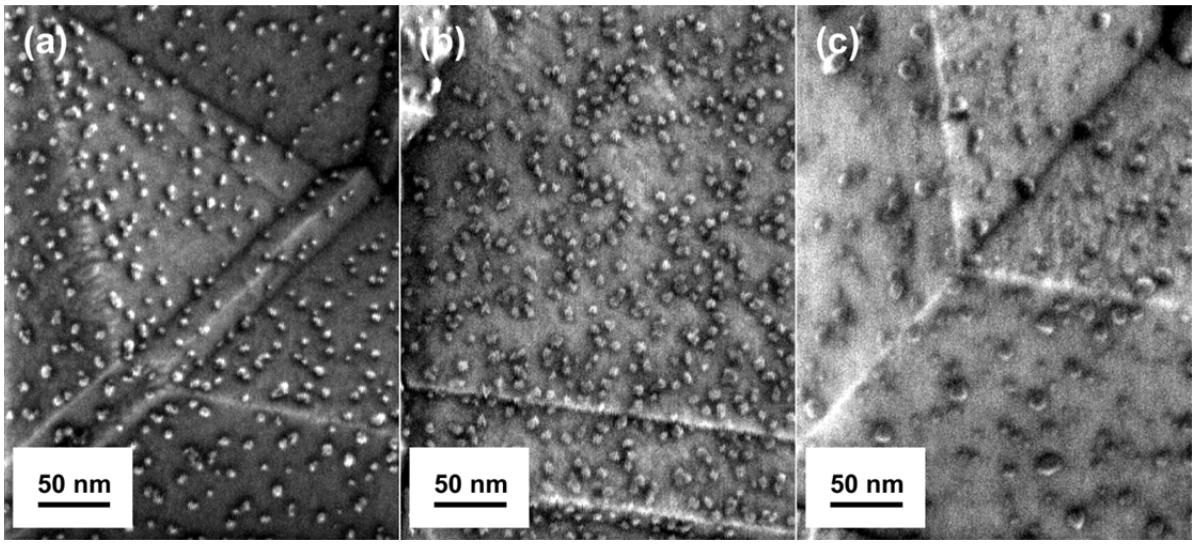

Figure 8-5: SEM images of wet-chemically deposited (a) Au, (b) Cu, and (c) Ni particles on diamond.

To enlarge the catalyst loading on the diamond electrode, a further electrochemical deposition, or an overgrowth of the seeds, is necessary. Experimental result proves

that with wet-chemical seeding, the problem of nucleation energy barrier is overcome (**Figure 8-6 a**). Compared with the unseeded sample (**figure 8-6 b**), particle deposited densely on the grains rather than only on the grain boundaries. As a result, the particle density is enhanced by more than two orders of magnitude.

The deposition mechanism is analyzed via the deposition *i-t* curves. **Figure 8-7 (a)** shows the deposition curves from the electrochemical growth with and without seeding. The deposition curve of the unseeded sample has a current maximum. Mathematically, this process is described with **equation 8-2 and 8-3**. Depending on different nucleation process, the curve can be fitted with either instantaneous nucleation (all nucleation happens at the first nucleation) or progressive nucleation (nucleation happens throughout the deposition process) [172]:

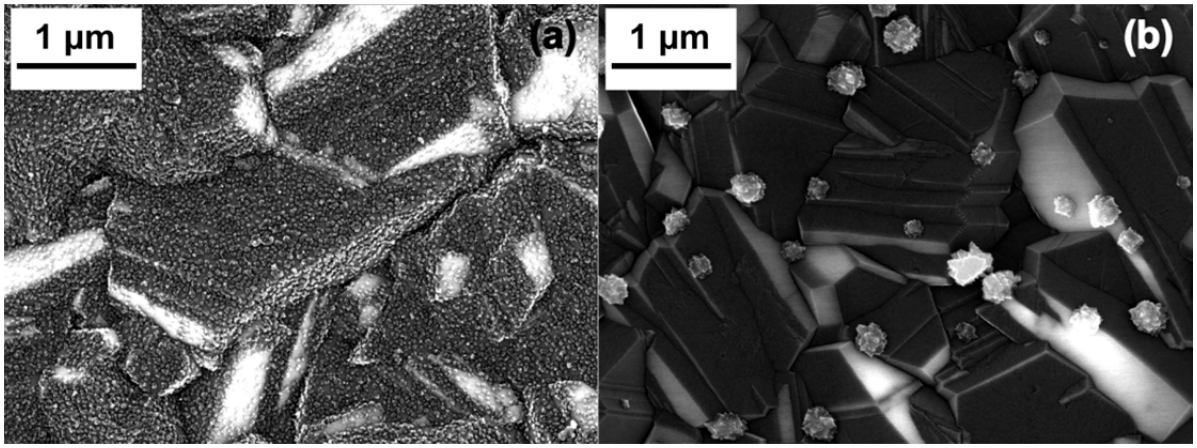

Figure 8-6: SEM images for samples after electrochemical deposition at -0.2 V vs Ag/AgCl (1 M KCl) (with a charge of 7.2 mC) on a wet-chemically seeded sample (a) and a bare diamond sample (b).

$$\left(\frac{i}{i_{\max}}\right)^2_{\text{prog}} = 1.2254\frac{(t-t_0)_{\max}}{(t-t_0)}\left[1-\exp\left(-2.3367\frac{(t-t_0)^2}{(t-t_0)^2_{\max}}\right)\right]^2 \quad (8\text{-}2)$$

and

$$\left(\frac{i}{i_{\max}}\right)^2_{\text{inst}} = 1.9542\frac{(t-t_0)_{\max}}{(t-t_0)}\left[1-\exp\left(-1.2564\frac{(t-t_0)}{(t-t_0)_{\max}}\right)\right]^2 \quad , \quad (8\text{-}3)$$

where i_{max} and t_{max} are the maximum current and the corresponding time, respectively; t_0 is the time when the deposition starts (here t_0 = 0). By comparing the deposition curve with the simulated curves (**figure 8-7 b**), the initial curve fits better the progressive nucleation. This is in accordance with the experimental observation of large particle coexisting with much smaller particles. At a later stage, the deposition curve deviates from both progressive and instantaneous deposition probably because of the side-reaction of hydrogen evolution happening at the same time, contributing an extra current.

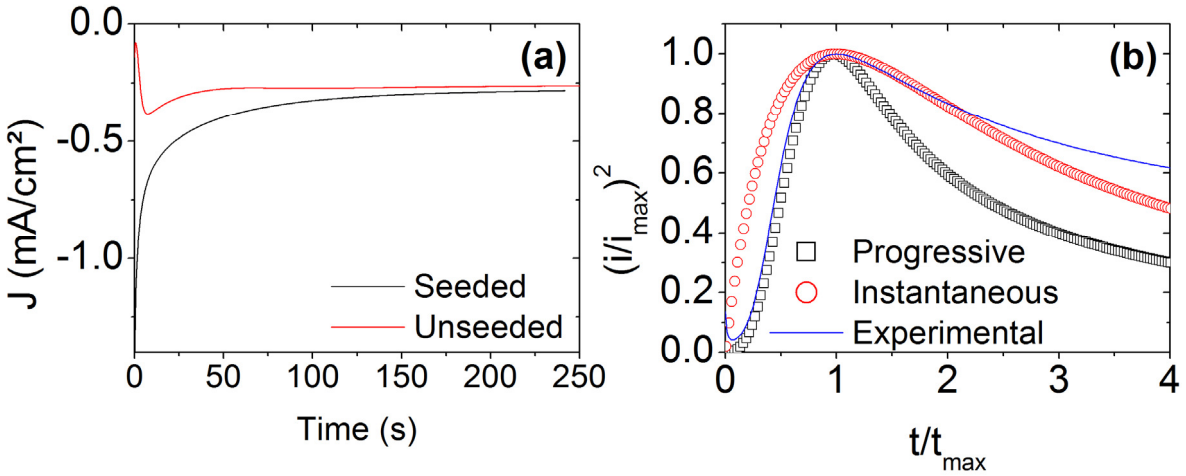

Figure 8-7: *J-t* curves for electrochemical growth of Pt particles on diamond surface with (black solid) and without (red) wet-chemically synthesized Pt particles as seeds. (b) The simulation curves for instantaneous (red circular) and progressive (blue triangular) growth modes in comparison to the growth curve of Pt particles on diamond electrode without wet-chemical seeding.

For the deposition curve of the seeded sample, the behavior is a monotonous decay without a current maximum. This behavior differs from unseeded sample and the theoretical prediction. The physical meaning of this current maximum is explained previously [171]. Initially, when the number of nuclei is small (and the time is short), the diffusion layers of each particle are not overlapping (**figure 8-8 a**). Therefore, with increasing number of nuclei (and increasing time), the total surface area of the diffusion zone will increase with increasing time. However, as soon as the diffusion zone of each particle start to overlap, the surface area of the diffusion zone will reach a maximum, and then decrease, and the three-dimensional diffusion will finally become 2-dimensional (**figure 8-8 b**). For unseeded case, this model is true; however, for seeded samples, the initial diffusion zones of neighboring seeds are already overlapping because of the high density of seeds. The maximum of current will be reached in the first moment, and only a monotonous decay is later recorded.

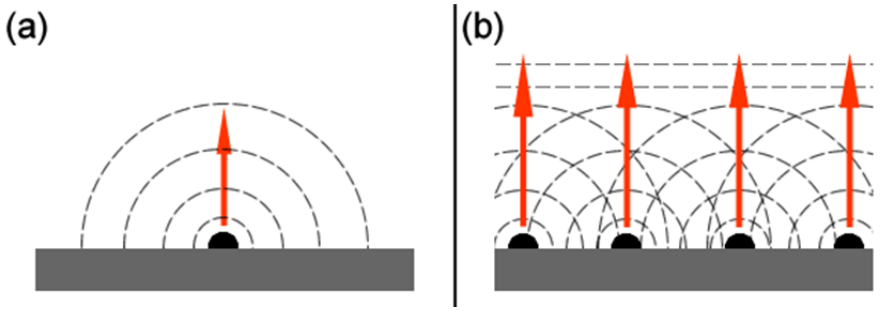

Figure 8-8: Schematic drawing of the spreading of the diffusion zones surrounding particles during electrochemical deposition for (a) vastly distributed particles and (b) closely located particles.

Because of the enhanced seeding densities, the growth of individual particles is slowed down, enabling fine tuning of particle sizes. **Figure 8-9** shows the particles deposited

with different amount of charge. Such an accurate controllability of the particle size is not possible with thermal de-wetting method.

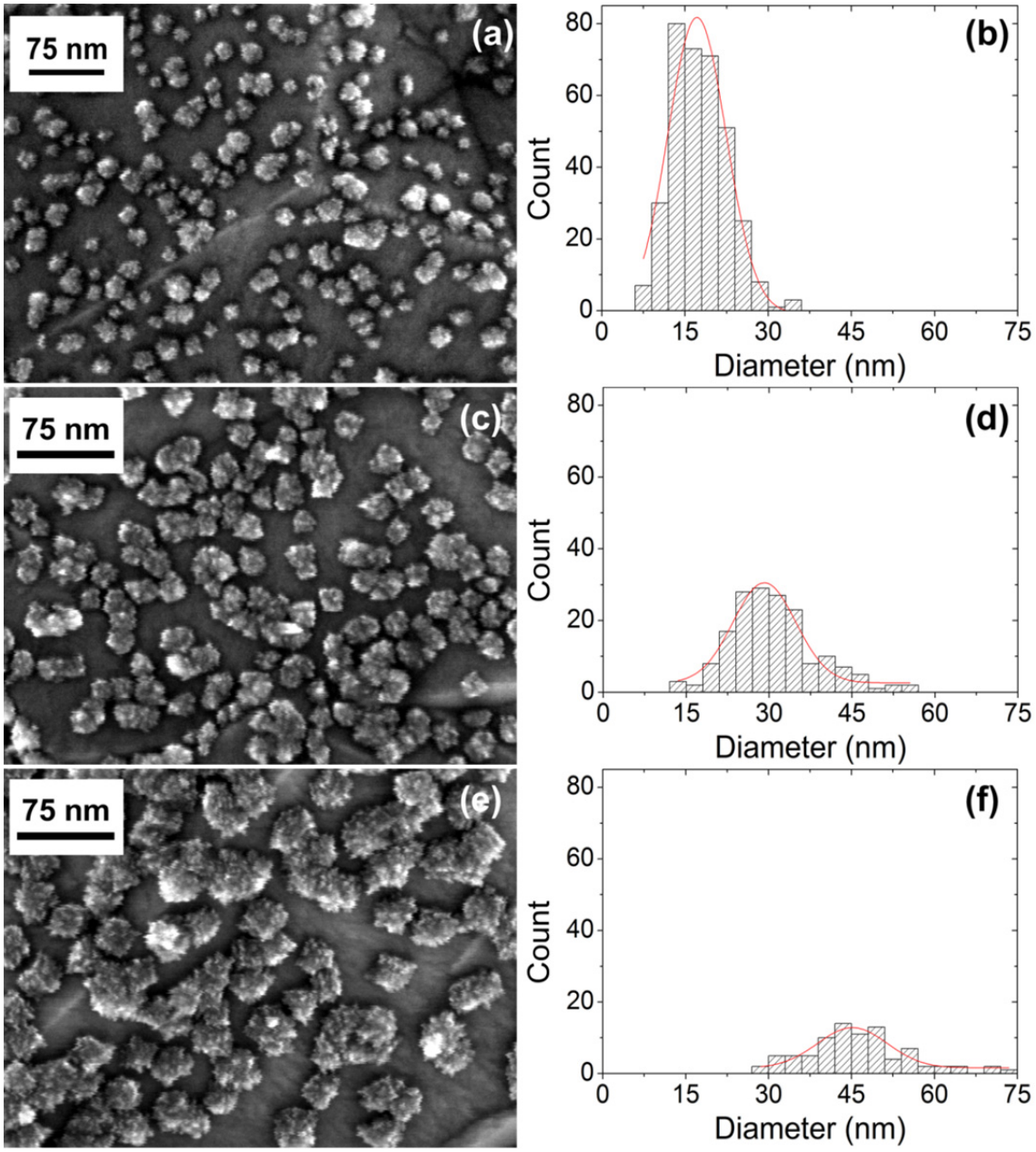

Figure 8-9: SEM images (a, b, c) and histograms of particle sizes (d, e, f) of two-step deposited Pt particles on diamond surface with consumed charge of 1.8 mC (a, d), 7.2 mC (b, e), and 14.4 mC (c, f).

From the electrochemical measurement of hydrogen desorption, the active Pt surface area can be calculated and compared to a planar Pt electrode (**figure 8-10**). The area hydrogen desorption peak is 0.91 mC for diamond particle decorated diamond electrode in comparison to 0.21 mC for a planar Pt electrode. This result shows that the active surface area has been approximately quadrupled by the Pt nanoparticles.

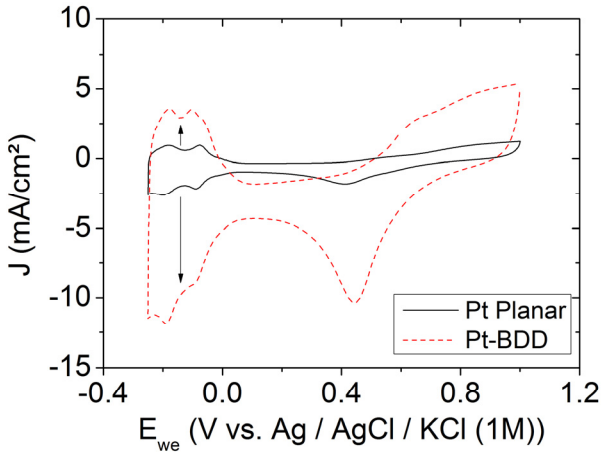

Figure 8-10: The background current of a planar Pt electrode (black solid line) and diamond electrode decorated with Pt nanoparticles (red dashed line). Arrows indicate the enlargements of hydrogen desorption/adsorption peaks.

8.2 Diamond-Pt Core-Shell Nanowires as Catalyst

In the last section, highly dense nanoparticles have been deposited on planar diamond electrode. However, if we consider a close-packed layer of semispherical particles, the maximum surface enlargement is 3.63 times of a planar electrode, which is very limited [147]. Therefore, we need to apply nanostructured diamond surface as a 3D substrate for catalysts. By coating diamond nanostructures with metal catalysts, the system will combine electronic and mechanic properties of diamond with beneficial properties of metal catalysts [143]. Although there has been report about using diamond nanowires as catalyst-support, in these reports the metal catalyst only covered very small area because of the fabrication methods [195, 198]. As a result, the total active area is still not high. In the **chapter 7** uniform metal coating on diamond has been achieved with DC sputtering technique; it can be naturally transferred to the fabrication of metal-based catalysts [199].

PtDia20, 40, and 60 samples are fabricated with the sample method described in **chapter 6**. In order to investigate the Pt-coverage which is very important for a catalyst, the fine structures of Pt-coated diamond wires were characterized by TEM (**figure 8-11**). A uniform coverage of nanoparticles on the nanowires is detected at all the three samples. These particles are formed in a self-organization process to minimize the overall surface energy, as is described by Winterbottom construction which describes the equilibrium shape of supported nanoparticles [200]. For the PtDia20 sample, the particles are not covering the complete surface. With more Pt deposition, PtDia40 and PtDia60 show a full coverage of nanoparticles. However, the adjacent wires start to agglomerate, forming thicker wires: **Figure 8-11 (b)** and **(c)** actually show a bunch of wires covered by Pt nanoparticles.

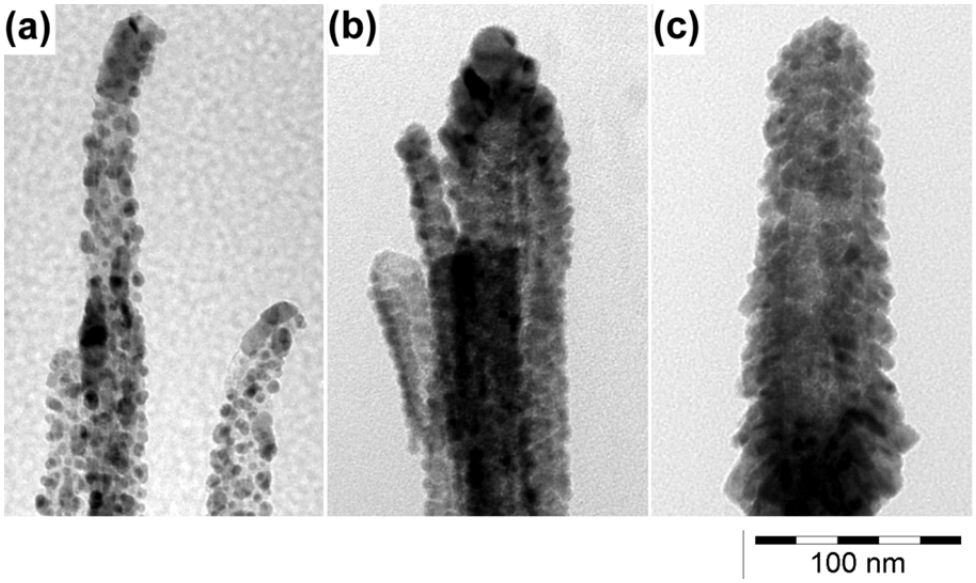

Figure 8-11: TEM images of (a) PtDia20, (b) PtDia40 and (c) and PtDia60.

The wire agglomeration is also reflected on the electrochemical activities of these samples. Cyclic voltammetry in a potential window of 1.2 V is performed at 100 mV/s on all the samples; a planar Pt sample is also measured in the same condition for comparison (**figure 8-12 a**). For all the samples, typical Pt the behaviors are recorded: hydrogen adsorption/desorption between 0.2 and -0.2 V and Pt surface oxidation/reduction between 1.0 and 0.4 V. To relate the cyclic voltammogram to the equivalent Pt surface area, the hydrogen desorption peak area Q_H is used (**figure 8-12 b**). For a planar Pt surface, the standard Q_H value is 0.21 mC/cm^2 [173]. A higher Q_H represents surface enlargement. Among the three samples, PtDia40 has the largest hydrogen desorption signal (4.82 mC/cm^2), which corresponds to 23 times of a planar platinum electrode. This value is even larger than the surface enlargement provided by the diamond nanowire forest (19.2 times) due to the extra surface are provided by the Pt nanoparticles. Compared to previous results on Pt deposition on planar diamond surface, the array of core-shell wires provides ~4 times higher activity[147]. However, similar to the decreasing trend of the gravitational capacitance with thicker Ni coating, the specific area of Pt is decreasing when more Pt is deposited. The specific area of Pt (A_{Pt}) is calculated using:

$$A_{Pt} = \frac{Q_H/0.21}{M_{\mathrm{Pt}}} \quad , \tag{8-4}$$

where M_{Pt} is the mass of Pt per unit area, which is 42.9, 85.8, and 128.7 µg/cm^2 for DiaPt20, 40 and 60, respectively. The results are plotted in **figure 8-12 (b)**. A highest specific active surface of 33 m^2/g was achieved on PtDia20, which has reached the same order of magnitude of other Pt catalyst supported on activated carbon (60 – 100 m^2/g) [173, 186].

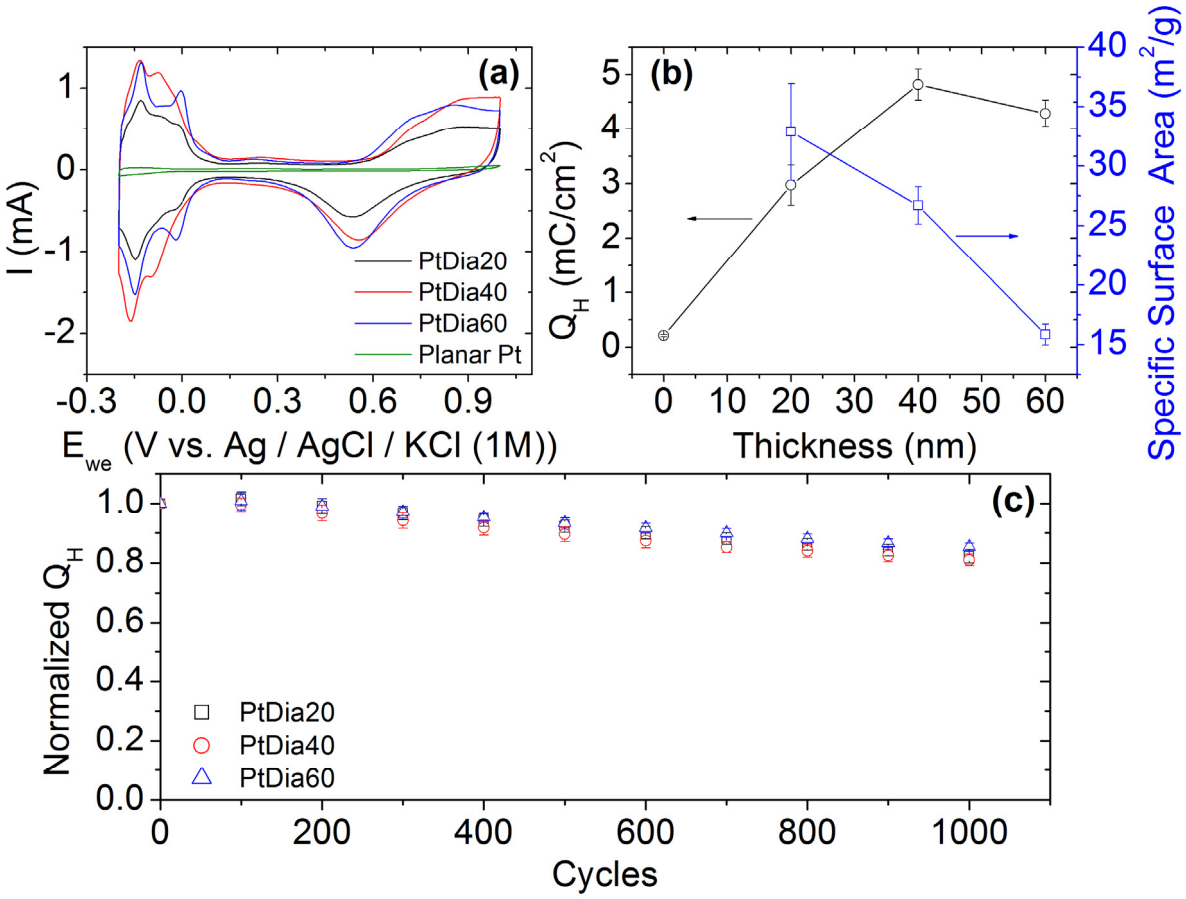

Figure 8-12: Electrochemical measurements for PtDia samples in 2 M H_2SO_4: (a) cyclic voltammetry in -0.2 to 1.0 V window; (b) hydrogen desorption charge (QH) and specific surface area of Pt vs coating thickness; a thickness of 0 means planar Pt electrode; (c) decay of Q_H during 1000 cycles at 100 mV/s in -0.2 to 1.0 V window.

Finally, the stability is tested via 1000 charging/discharging cycles in a 1.2 V potential window at a scan rate of 100 mV/s. Q_H is used to characterize the Pt reactivity. For electrocatalyst, the stability is known to be a problem. For example, it was reported that the activity of Pt particles on diamond from direct electrochemical deposition lost ~ 40% after 100 cycles [193, 194]. In our case, however, after 1000 cycles, Q_H retains ~ 85% for all the samples (**figure 8-12 c**), and the stability is PtDia60 > PtDia40 > PtDia20. This good stability is attributed to the strong binding between the Pt particles and the diamond nanowires. The reason for this strong binding is, however, not clear at the moment. There could be a physical explanation for that. Due to the etching, the diamond wire surface is heavily damaged, and for this reason the facial energy was increased. After covering by Pt the total energy was expected to be lowered, resulting in a stable Pt-C interface.

The methanol oxidation performance of the PtDia20 sample is shown in **figure 8-13**. The double peak is typical for methanol oxidation on a Pt catalyst. In the forward scan, a peak centered at 0.65 V corresponds to the deprotonation of methanol with the

generation of CO ad-molecules on the Pt surface. These adsorbents are oxidized in the reverse scan, generating another oxidation peak centered at 0.45 V. For the Pt catalyst, the surface adsorbed species block the active sites and hence decrease the performance of the catalyst. As observed in **figure 8-13 (a)**, the peak current decreases in each cycle. Because Pt is a noble metal, a short life time of a Pt-containing device causes high costs. Therefore, it is of high practical importance to "refresh" these electrodes after they are poisoned.

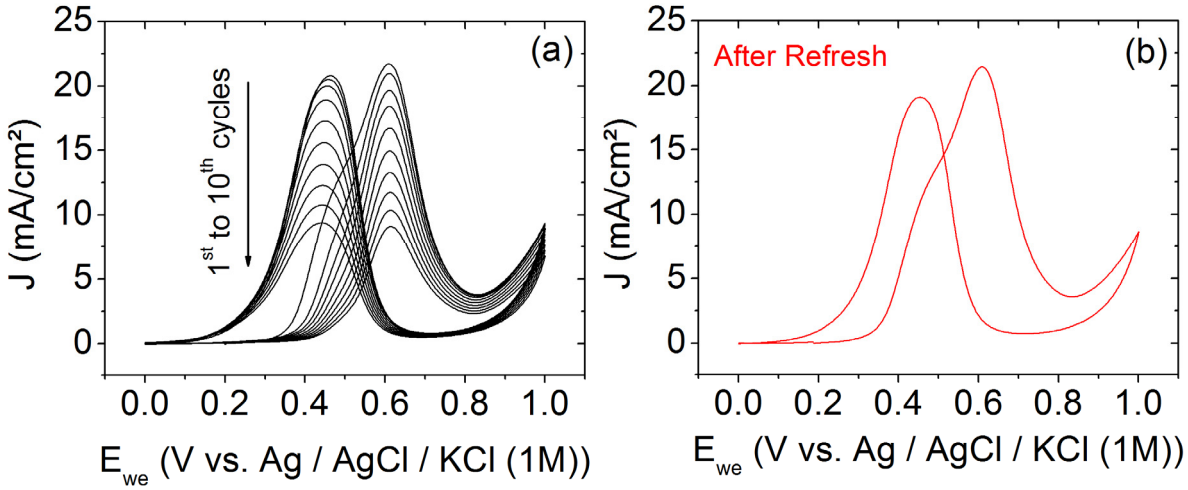

Figure 8-13: Methanol oxidation on a PtDia20 sample in an aqueous solution of 1 M H_2SO_4 containing 1 M methanol. (a) Cyclic voltammetry (1 to 10 cycles) between 0 and 1 V at 15 mV/s. After (a), the sample was refreshed in 2 M H_2SO_4 at potentials of +5 V and –5 V for 1 min, respectively. Then the first cycle of cyclic voltammetry (b) was recorded again with the same parameters as (a).

For diamond-based electrodes, surface contaminants can be easily removed by applying a high negative/positive potential in an aqueous solution (electrochemical polishing) [201]. The hydrogen or oxygen radicals generated in this process will act as cleaning agents. Because of the extreme stability, diamond will not be etched in this process. Previous study has proved the diamond electrode are stable in a wide potential range (-35 to +6 V) in aqueous solutions [82, 202]. For commercial Pt-C catalyst, this method is, however, not applicable. The reason is that the sp^2 carbon substrate cannot survive high potential treatment. **Figure 8-14** shows an SEM image of a highly oriented pyrolytic graphite (HOPG) electrode after 10 s bias at 4 V in 2 M H_2SO_4. The left part of the electrode is in contact with the solution and is heavily damaged. Therefore, what can be used to clean diamond electrode is not suitable for sp^2 carbon based materials.

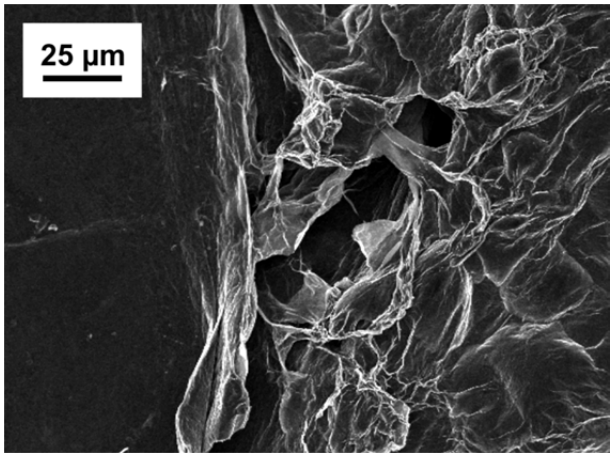

Figure 8-14: SEM image of an HOPG electrode after 10 s oxidation in 2 M H_2SO_4 solution under a 4 V bias. Only the right side is exposed to liquid, showing severe damage in comparison to the untreated left side [203].

However, in the case of Pt-Diamond composites, because of the diamond substrates, these samples are potentially suitable for high-potential refreshing. In order to confirm this idea, PtDia20 sample after the intoxication shown in **figure 8-13 (a)** is refreshed in 2 M H_2SO_4 at potentials of +5 V and –5 V for 1 min, sequentially. **Figure 8-13 (b)** shows the first cycle of methanol oxidation under the same condition as **figure 8-13 (a)**. It is clearly observed that the catalytic activities have been completely recovered. This is a clear evidence of the benefit provided by the diamond substrate. With the extreme stability and the large active surface area of Pt, Diamond-Pt core-shell nanowire are highly promising substitutes for the commercial Pt-C catalysts in energy applications. Moreover, the fabrication method of both diamond nanowires and diamond-Pt core-shell wires are suitable for large scare applications (up to 6 inch). All the techniques, like sputtering and RIE etching are all compatible with clean room technology. Therefore, this material is very promising for reproducible mass production.

8.3 Summary and Conclusions

In this chapter, the diamond-based surface enlarged catalytic electrode is investigated. The achievements concern mainly the following three aspects:

1) For planar diamond electrode, the highest Pt particle density has been realized via seeding-assisted electrochemical deposition. The Pt-decorated diamond electrode achieves an active Pt surface area equal to ~ 4 times that of a planar Pt electrode.
2) Using diamond nanowires as cores, a 3D catalytic material, i.e. Diamond-Pt core-shell wires, have been fabricated. The active Pt surface area was enhanced to 24 times that of a planar Pt electrode. The specific area of Pt in terms of m^2/g was comparable to commercial Pt-C catalysts.

3) As opposed to the existing Pt-C catalysts, Pt-diamond catalysts have proven to be "refreshable". By biasing the electrode at ± 5 V in 2 M H_2SO_4, poisoning of the catalyst can be completely relieved.

Chapter 9: Summary and Outlook

9.1 Summary

The development of this thesis can be broken down into three phases. Initially, the work was built upon the existing diamond nanostructuring technology, in which nanowires are fabricated via plasma etching. However, both experimental results and theoretical analysis show that the surface enlargement provided by these wires is insufficient for the application of energy storage/conversion. Driven by this problem the thesis enters phase two, in which an alternative route towards high-surface-area diamond materials is developed. As opposed to the top-down etching, the diamond surface is enlarged using bottom-up approaches, i.e. templated growth methods. In this part, challenging attempts such as coating diamond on high aspect ratio structures (1:30) and spheres have been made; new and interesting diamond structures have been fabricated, like ultra-long diamond wires (up to 30 μm) and diamond foam. In the third phase, applications based on these surface enlarged electrodes are investigated, i.e. supercapacitors and electrocatalyst.

For supercapacitors, both bare diamond nanostructures and those with pseudocapacitive coatings are applied. All these materials exhibit suitability for high frequency applications; the modest capacitance values are compensated by the high power performances. The Ni-hydroxide coated diamond nanowires are particularly interesting, because the coating enhances the capacitance of bare diamond wires by nearly three orders of magnitude to ~ 100 mF/cm^2. Therefore, this material has more potential compared to pure diamond supercapacitor devices.

The method for pseudocapacitive coating can be readily transplanted to other functional materials. Catalyst coating is shown as an example. With a thin Pt coating, the Pt-diamond composite catalyst achieved the performance of a commercial Pt-C catalyst. Most importantly, Pt-diamond catalyst can survive harsh working conditions which would render graphitic carbon nonviable. Therefore, the material is a potential substitute for industrially used traditional Pt catalysts.

9.2 Outlook

In this thesis, diamond-based nanostructured materials have shown promising applications in the supercapacitor and electrocatalysis. However, this is not the end of the story. In **chapters 7** and **8**, we have seen that a large variety of potential applications are enlightened if a layer of functional coating is deposited on the nanostructured diamond electrode. In fact, diamond has often served as a non-functional material which has been used as coating or substrate. In electrochemistry, the nanostructured diamond electrode has been extensively used as a substrate, and the applications include sensing and catalysis. Therefore, in the future, the meaning of this thesis may lie

far beyond the topic of supercapacitors. Possible applications in this direction include but are not limited to:

1) Photochemistry: the decoration of a diamond surface with functional molecules (dyes and proteins) for energy conversion has been widely investigated [204-211]. In these applications a large surface area is usually preferred. For example, in light conversion, a thick layer of porous diamond can absorb more light and thus obtain higher efficiency. In fact, diamond foam is potentially attractive in the light of dye-sensitized solar cells [208, 209]. Moreover, taking into consideration the negative electron affinity (NEA) of diamond [212-214], using diamond for photocatalysis is now a hot topic in the diamond community [204, 210, 211]. However, this phenomenon has not been investigated on nanostructured diamond. As a result, the diamond materials developed in this thesis may be also interesting for this topic.
2) Sensing: it may sound strange that surface enlarged electrodes can be used as substrates for sensor electrodes. In fact, the low background current is one of the advantages of using diamond as a sensing electrode [88, 215]. Nanostructured diamond materials have been used widely as the electrode material for electrochemical sensors [29, 216-223]. The multiplication of signal given by surface enlargement enhances the sensitivity as well as the limit of detection. However, the combination of diamond with functional coating is still not yet well investigated. Examples like copper oxide or nickel oxide coating on diamond nanowires for glucose sensing are potential candidates for future researches.

Reference

[1] Shiomi H. Reactive ion etching of diamond in O2 and CF4 plasma, and fabrication of porous diamond for field emitter cathodes. Jpn J Appl Phys, Part 1. 1997;36(12B):7745-8.
[2] Shenderova OA, Padgett CW, Hu Z, Brenner DW. Diamond nanorods. J Vac Sci Technol B. 2005;23(6):2457-64.
[3] Yang NJ, Uetsuka H, Williams OA, Osawa E, Tokuda N, Nebel CE. Vertically aligned diamond nanowires: Fabrication, characterization, and application for DNA sensing. Phys Status Solidi A. 2009;206(9):2048-56.
[4] Masuda H, Watanabe M, Yasui K, Tryk D, Rao T, Fujishima A. Fabrication of a nanostructured diamond honeycomb film. Adv Mater. 2000;12(6):444-7.
[5] Forsberg P, Karlsson M. Inclined surfaces in diamond: broadband antireflective structures and coupling light through waveguides. Opt Express. 2013;21(3):2693-700.
[6] Smirnov W, Kriele A, Yang N, Nebel CE. Aligned diamond nano-wires: Fabrication and characterisation for advanced applications in bio- and electrochemistry. Diamond Relat Mater. 2010;19(2-3):186-9.
[7] Zou YS, Yang Y, Zhang WJ, Chong YM, He B, Bello I, et al. Fabrication of diamond nanopillars and their arrays. Appl Phys Lett. 2008;92(5):053105.
[8] Yang NJ, Uetsuka HS, Sawa E, Nebel CE. Vertically Aligned Nanowires from Boron-Doped Diamond. Nano Lett. 2008;8(11):3572-6.
[9] Yang NJ, Uetsuka H, Nebel CE. Biofunctionalization of Vertically Aligned Diamond Nanowires. Adv Funct Mater. 2009;19(6):887-93.
[10] Honda K, Rao TN, Tryk DA, Fujishima A, Watanabe M, Yasui K, et al. Electrochemical Characterization of the Nanoporous Honeycomb Diamond Electrode as an Electrical Double-Layer Capacitor. J Electrochem Soc. 2000;147(2):659-64.
[11] Ting JM, Lagounov AG, Lake ML. Chemical vapour infiltration of diamond into a porous carbon. J Mater Sci Lett. 1996;15(4):350-2.
[12] Baranauskas V, Peterlevitz AC, Ceragioli HJ, Durrant SF. Growth of diamond and carbon structures on natural pyrolized fibers. Thin Solid Films. 2001;398:260-4.
[13] Demkowicz PA, Bell NS, Gilbert DR, Singh R, Drawl WR, Adair JH. Diamond-coated silicon carbide whiskers. J Am Ceram Soc. 1999;82(4):1079-81.
[14] Masuda H, Yanagishita T, Yasui K, Nishio K, Yagi I, Rao TN, et al. Synthesis of well-aligned diamond nanocylinders. Adv Mater. 2001;13(4):247-9.
[15] Terranova ML, Orlanducci S, Fiori A, Tamburri E, Sessa V, Rossi M, et al. Controlled evolution of carbon nanotubes coated by nanodiamond: the realization of a new class of hybrid nanomaterials. Chem Mater. 2005;17(12):3214-20.
[16] Luo D, Wu L, Zhi J. Fabrication of Boron-Doped Diamond Nanorod Forest Electrodes and Their Application in Nonenzymatic Amperometric Glucose Biosensing. Acs Nano. 2009;3(8):2121-8.
[17] Kato H, Hees J, Hoffmann R, Wolfer M, Yang N, Yamasaki S, et al. Diamond foam electrodes for electrochemical applications. Electrochem Commun. 2013;33:88-91.
[18] Gao F, Nebel CE. Diamond-Based Supercapacitors: Realization and Properties. ACS Appl Mater Interfaces. 2015.
[19] Kondo T, Lee S, Honda K, Kawai T. Conductive diamond hollow fiber membranes. Electrochem Commun. 2009;11(8):1688-91.

[20] Yu Y, Wu LZ, Zhi JF. Diamond Nanowires: Fabrication, Structure, Properties, and Applications. Angew Chem Int Edit. 2014;53(52):14326-51.
[21] Kobashi K, Tachibana T, Yokota Y, Kawakami N, Hayashi K, Yamamoto K, et al. Fibrous structures on diamond and carbon surfaces formed by hydrogen plasma under direct current bias and field electron-emission properties. J Mater Res. 2003;18(2):305-26.
[22] Joo SW, Banerjee AN. Field emission characterization of vertically oriented uniformly grown nickel nanorod arrays on metal-coated silicon substrate. J Appl Phys. 2010;107(11):114317.
[23] Chang TH, Panda K, Panigrahi BK, Lou SC, Chen CL, Chan HC, et al. Electrophoresis of Nanodiamond on the Growth of Ultrananocrystalline Diamond Films on Silicon Nanowires and the Enhancement of the Electron Field Emission Properties. J Phys Chem C. 2012;116(37):19867-76.
[24] Palomino J, Varshney D, Resto O, Weiner BR, Morell G. Ultrananocrystalline Diamond-Decorated Silicon Nanowire Field Emitters. ACS Appl Mater Interfaces. 2014;6(16):13815-22.
[25] Masuda H, Yasui K, Watanabe M, Nishio K, Nakao M, Tamamura T, et al. Fabrication of through-hole diamond membranes by plasma etching using anodic porous alumina mask. Electrochem Solid St. 2001;4(11):G101-G3.
[26] Hausmann BJM, Babinec TM, Choy JT, Hodges JS, Hong SK, Bulu I, et al. Single-color centers implanted in diamond nanostructures. New J Phys. 2011;13:045004.
[27] Eifert A, Smirnov W, Frittmann S, Nebel C, Mizaikoff B, Kranz C. Atomic force microscopy probes with integrated boron doped diamond electrodes: Fabrication and application. Electrochem Commun. 2012;25:30-4.
[28] Wei M, Terashima C, Lv M, Fujishima A, Gu ZZ. Boron-doped diamond nanograss array for electrochemical sensors. Chem Commun. 2009(24):3624-6.
[29] Zhao JW, Wu LZ, Zhi JF. Non-enzymatic glucose detection using as-prepared boron-doped diamond thin-film electrodes. Analyst. 2009;134(4):794-9.
[30] Shalini J, Sankaran KJ, Dong CL, Lee CY, Tai NH, Lin IN. In situ detection of dopamine using nitrogen incorporated diamond nanowire electrode. Nanoscale. 2013;5(3):1159-67.
[31] Zhao GH, Qi Y, Tian Y. Simultaneous and direct determination of tryptophan and tyrosine at boron-doped diamond electrode. Electroanal. 2006;18(8):830-4.
[32] Simon P, Gogotsi Y. Materials for electrochemical capacitors. Nat Mat. 2008;7(11):845-54.
[33] Liu HS, Song CJ, Zhang L, Zhang JJ, Wang HJ, Wilkinson DP. A review of anode catalysis in the direct methanol fuel cell. J Power Sources. 2006;155(2):95-110.
[34] Frackowiak E. Carbon materials for supercapacitor application. Phys Chem Chem Phys. 2007;9(15):1774-85.
[35] Lozano-Castelló D, Cazorla-Amorós D, Linares-Solano A, Shiraishi S, Kurihara H, Oya A. Influence of pore structure and surface chemistry on electric double layer capacitance in non-aqueous electrolyte. Carbon. 2003;41(9):1765-75.
[36] Barbieri O, Hahn M, Herzog A, Kötz R. Capacitance limits of high surface area activated carbons for double layer capacitors. Carbon. 2005;43(6):1303-10.
[37] Liu JP, Jiang J, Bosman M, Fan HJ. Three-dimensional tubular arrays of MnO2-NiO nanoflakes with high areal pseudocapacitance. J Mater Chem. 2012;22(6):2419-26.

[38] Hwang DS, Saito T, Fujimori N. New etching process for device fabrication using diamond. Diamond Relat Mater. 2004;13(11-12):2207-10.
[39] Smirnov W, Fraunhofer IAF F, Ambacher O. Diamond Diversity: From Micro- and Nanostructuring to Multifunctional Tools and Devices: Fraunhofer IRB Verlag; 2012.
[40] Swain GM, Anderson AB, Angus JC. Applications of diamond thin films in electrochemistry. MRS Bull. 1998;23(9):56-60.
[41] Buffat P, Borel JP. Size Effect on Melting Temperature of Gold Particles. Phys Rev A. 1976;13(6):2287-98.
[42] Mehedi H-a, Mille V, Achard J, Brinza O, Gicquel A. Effect of the process parameters of inductively coupled plasma reactive ion etching on the fabrication of diamond nanotips. Phys Status Solidi A. 2014;211(10):2343-6.
[43] Yang NJ, Yu JH, Uetsuka H, Nebel CE. Characterization of diamond surface terminations using electrochemical grafting with diazonium salts. Electrochem Commun. 2009;11(11):2237-40.
[44] Haynes WM, Lide DR. CRC handbook of chemistry and physics : a ready-reference book of chemical and physical data. 91st ed. Boca Raton, Fla.: CRC Press; 2010.
[45] Tran DT, Fansler C, Grotjohn TA, Reinhard DK, Asmussen J. Investigation of mask selectivities and diamond etching using microwave plasma-assisted etching. Diamond Relat Mater. 2010;19(7-9):778-82.
[46] Laidler KJ. Chemical kinetics. 3rd ed. New York: HarperCollins; 1987.
[47] Pech D, Brunet M, Durou H, Huang P, Mochalin V, Gogotsi Y, et al. Ultrahigh-power micrometre-sized supercapacitors based on onion-like carbon. Nat Nanotechnol. 2010;5(9):651-4.
[48] Yang NJ, Smirnov W, Nebel CE. Three-dimensional electrochemical reactions on tip-coated diamond nanowires with nickel nanoparticles. Electrochem Commun. 2013;27:89-91.
[49] Caruso F. Nanoengineering of Particle Surfaces. Adv Mater. 2001;13(1):11-22.
[50] Ania CO, Khomenko V, Raymundo-Piñero E, Parra JB, Béguin F. The Large Electrochemical Capacitance of Microporous Doped Carbon Obtained by Using a Zeolite Template. Adv Funct Mater. 2007;17(11):1828-36.
[51] Li WR, Chen DH, Li Z, Shi YF, Wan Y, Wang G, et al. Nitrogen-containing carbon spheres with very large uniform mesopores: The superior electrode materials for EDLC in organic electrolyte. Carbon. 2007;45(9):1757-63.
[52] Xue T, Xu CL, Zhao DD, Li XH, Li HL. Electrodeposition of mesoporous manganese dioxide supercapacitor electrodes through self-assembled triblock copolymer templates. J Power Sources. 2007;164(2):953-8.
[53] Liu HJ, Wang XM, Cui WJ, Dou YQ, Zhao DY, Xia YY. Highly ordered mesoporous carbon nanofiber arrays from a crab shell biological template and its application in supercapacitors and fuel cells. J Mater Chem. 2010;20(20):4223-30.
[54] Wang YG, Xia YY. Electrochemical capacitance characterization of NiO with ordered mesoporous structure synthesized by template SBA-15. Electrochim Acta. 2006;51(16):3223-7.
[55] Gracio JJ, Fan QH, Madaleno JC. Diamond growth by chemical vapour deposition. J Phys D: Appl Phys. 2010;43(37):374017.
[56] Williams OA, Hees J, Dieker C, Jager W, Kirste L, Nebel CE. Size-Dependent Reactivity of Diamond Nanoparticles. Acs Nano. 2010;4(8):4824-30.

[57] Okada Y, Tokumaru Y. Precise Determination of Lattice-Parameter and Thermal-Expansion Coefficient of Silicon between 300-K and 1500-K. J Appl Phys. 1984;56(2):314-20.
[58] Priolo F, Gregorkiewicz T, Galli M, Krauss TF. Silicon nanostructures for photonics and photovoltaics. Nat Nanotechnol. 2014;9(1):19-32.
[59] Walavalkar SS, Hofmann CE, Homyk AP, Henry MD, Atwater HA, Scherer A. Tunable Visible and Near-IR Emission from Sub-10 nm Etched Single-Crystal Si Nanopillars. Nano Lett. 2010;10(11):4423-8.
[60] Peng KQ, Xu Y, Wu Y, Yan YJ, Lee ST, Zhu J. Aligned single-crystalline Si nanowire arrays for photovoltaic applications. Small. 2005;1(11):1062-7.
[61] Fang H, Wu Y, Zhao JH, Zhu J. Silver catalysis in the fabrication of silicon nanowire arrays. Nanotechnology. 2006;17(15):3768-74.
[62] Sivakov V, Andra G, Gawlik A, Berger A, Plentz J, Falk F, et al. Silicon Nanowire-Based Solar Cells on Glass: Synthesis, Optical Properties, and Cell Parameters. Nano Lett. 2009;9(4):1549-54.
[63] Sanjay KS, Dinesh K, Schmitt SW, Sood KN, Christiansen SH, Singh PK. Large area fabrication of vertical silicon nanowire arrays by silver-assisted single-step chemical etching and their formation kinetics. Nanotechnology. 2014;25(17):175601.
[64] Wagner RS, Ellis WC. Vapor-Liquid-Solid Mechanism of Single Crystal Growth. Appl Phys Lett. 1964;4(5):89-90.
[65] Kim BJ, Tersoff J, Kodambaka S, Reuter MC, Stach EA, Ross FM. Kinetics of Individual Nucleation Events Observed in Nanoscale Vapor-Liquid-Solid Growth. Science. 2008;322(5904):1070-3.
[66] Thissandier F, Le Comte A, Crosnier O, Gentile P, Bidan G, Hadji E, et al. Highly doped silicon nanowires based electrodes for micro-electrochemical capacitor applications. Electrochem Commun. 2012;25:109-11.
[67] Thissandier F, Pauc N, Brousse T, Gentile P, Sadki S. Micro-ultracapacitors with highly doped silicon nanowires electrodes. Nanoscale Research Letters. 2013;8:1-5.
[68] Thissandier F, Gentile P, Pauc N, Brousse T, Bidan G, Sadki S. Tuning silicon nanowires doping level and morphology for highly efficient micro-supercapacitors. Nano Energy. 2014;5:20-7.
[69] Gentile P, Solanki A, Pauc N, Oehler F, Salem B, Rosaz G, et al. Effect of HCl on the doping and shape control of silicon nanowires. Nanotechnology. 2012;23(21).
[70] Hees JJ. All-diamond nanoelectrode arrays. Stuttgart: Fraunhofer-Verl.; 2013.
[71] Prawer S, Nemanich RJ. Raman spectroscopy of diamond and doped diamond. Philos Trans R Soc London, Ser A. 2004;362(1824):2537-65.
[72] Ferrari AC, Robertson J. Origin of the 1150-cm(-1) Raman mode in nanocrystalline diamond. Phys Rev B. 2001;63(12):121405.
[73] Kriele A, Williams OA, Wolfer M, Brink D, Muller-Sebert W, Nebel CE. Tuneable optical lenses from diamond thin films. Appl Phys Lett. 2009;95(3):031905.
[74] Locher R, Wagner J, Fuchs F, Maier M, Gonon P, Koidl P. Optical and Electrical Characterization of Boron-Doped Diamond Films. Diamond Relat Mater. 1995;4(5-6):678-83.
[75] Gajewski W, Achatz P, Williams OA, Haenen K, Bustarret E, Stutzmann M, et al. Electronic and optical properties of boron-doped nanocrystalline diamond films. Phys Rev B. 2009;79(4):045206.
[76] Stöber W, Fink A, Bohn E. Controlled growth of monodisperse silica spheres in the micron size range. J Colloid Interface Sci. 1968;26(1):62-9.

[77] Kim SW, Kim M, Lee WY, Hyeon T. Fabrication of hollow palladium spheres and their successful application to the recyclable heterogeneous catalyst for Suzuki coupling reactions. J Am Chem Soc. 2002;124(26):7642-3.
[78] Kruk M, Dufour B, Celer EB, Kowalewski T, Jaroniec M, Matyjaszewski K. Synthesis of mesoporous carbons using ordered and disordered mesoporous silica templates and polyacrylonitrile as carbon precursor. J Phys Chem B. 2005;109(19):9216-25.
[79] Kao L-H, Hsu T-C. Silica template synthesis of ordered mesoporous carbon thick films with 35-nm pore size from mesophase pitch solution. Mater Lett. 2008;62(4–5):695-8.
[80] Celii F. Diamond Chemical Vapor Deposition. Annu Rev Phys Chem. 1991;42(1):643-84.
[81] Butler JE, Woodin RL. Thin-Film Diamond Growth Mechanisms. Philos Trans R Soc London, Ser A. 1993;342(1664):209-24.
[82] Hoffmann R, Kriele A, Obloh H, Hees J, Wolfer M, Smirnov W, et al. Electrochemical hydrogen termination of boron-doped diamond. Appl Phys Lett. 2010;97(5):052103.
[83] Malta DM, Vonwindheim JA, Wynands HA, Fox BA. Comparison of the Electrical-Properties of Simultaneously Deposited Homoepitaxial and Polycrystalline Diamond Films. J Appl Phys. 1995;77(4):1536-45.
[84] Lagrange JP, Deneuville A, Gheeraert E. A large range of boron doping with low compensation ratio for homoepitaxial diamond films. Carbon. 1999;37(5):807-10.
[85] Granger MC, Witek M, Xu JS, Wang J, Hupert M, Hanks A, et al. Standard electrochemical behavior of high-quality, boron-doped polycrystalline diamond thin-film electrodes. Anal Chem. 2000;72(16):3793-804.
[86] Denisenko A, Pietzka C, Romanyuk A, El-Hajj H, Kohn E. The electronic surface barrier of boron-doped diamond by anodic oxidation. J Appl Phys. 2008;103(1):014904.
[87] Pleskov YV, Evstefeeva YE, Varnin VP, Teremetskaya IG. Synthetic semiconductor diamond electrodes: Electrochemical characteristics of homoepitaxial boron-doped films grown at the (111), (110), and (100) faces of diamond crystals. Russ J Electrochem. 2004;40(9):886-92.
[88] Brillas E, Martinez-Huitle CA. Synthetic diamond films : preparation, electrochemistry, characterizatio, and applications. Hoboken, N.J.: Wiley-Blackwell; 2011.
[89] Tarascon JM, Armand M. Issues and challenges facing rechargeable lithium batteries. Nature. 2001;414(6861):359-67.
[90] Kötz R, Carlen M. Principles and applications of electrochemical capacitors. Electrochim Acta. 2000;45(15-16):2483-98.
[91] Conway BE, Bockris JOM, Ammar IA. The dielectric constant of the solution in the diffuse and Helmholtz double layers at a charged interface in aqueous solution. Trans Faraday Society. 1951;47(0):756-66.
[92] Hayyan M, Mjalli FS, Hashim MA, AlNashef IM, Mei TX. Investigating the electrochemical windows of ionic liquids. Journal of Industrial and Engineering Chemistry. 2013;19(1):106-12.
[93] Ong SP, Andreussi O, Wu YB, Marzari N, Ceder G. Electrochemical Windows of Room-Temperature Ionic Liquids from Molecular Dynamics and Density Functional Theory Calculations. Chem Mater. 2011;23(11):2979-86.

[94] Alam MT, Islam MM, Okajima T, Ohsaka T. Capacitance Measurements in a Series of Room-Temperature Ionic Liquids at Glassy Carbon and Gold Electrode Interfaces. J Phys Chem C. 2008;112(42):16600-8.
[95] Lauw Y, Horne MD, Rodopoulos T, Nelson A, Leermakers FAM. Electrical Double-Layer Capacitance in Room Temperature Ionic Liquids: Ion-Size and Specific Adsorption Effects. J Phys Chem B. 2010;114(34):11149-54.
[96] Pandey GP, Hashmi SA. Studies on electrical double layer capacitor with a low-viscosity ionic liquid 1-ethyl-3-methylimidazolium tetracyanoborate as electrolyte. Bull Mater Sci. 2013;36(4):729-33.
[97] Galiński M, Lewandowski A, Stępniak I. Ionic liquids as electrolytes. Electrochim Acta. 2006;51(26):5567-80.
[98] Taberna PL, Simon P, Fauvarque JF. Electrochemical Characteristics and Impedance Spectroscopy Studies of Carbon-Carbon Supercapacitors. J Electrochem Soc. 2003;150(3):A292.
[99] Passerini S, Appetecchi GB. Toward more environmentally friendly routes to high purity ionic liquids. MRS Bull. 2013;38(7):540-7.
[100] Wang HL, Casalongue HS, Liang YY, Dai HJ. Ni(OH)(2) Nanoplates Grown on Graphene as Advanced Electrochemical Pseudocapacitor Materials. J Am Chem Soc. 2010;132(21):7472-7.
[101] Park JH, Park OO, Shin KH, Jin CS, Kim JH. An Electrochemical Capacitor Based on a Ni(OH)[sub 2]/Activated Carbon Composite Electrode. Electrochem Solid-State Lett. 2002;5(2):H7.
[102] Sugimoto W, Iwata H, Yasunaga Y, Murakami Y, Takasu Y. Preparation of ruthenic acid nanosheets and utilization of its interlayer surface for electrochemical energy storage. Angew Chem Int Edit. 2003;42(34):4092-6.
[103] Broughton JN, Brett MJ. Investigation of thin sputtered Mn films for electrochemical capacitors. Electrochim Acta. 2004;49(25):4439-46.
[104] Broughton JN, Brett MJ. Variations in MnO2 electrodeposition for electrochemical capacitors. Electrochim Acta. 2005;50(24):4814-9.
[105] Hu CC, Chang KH, Lin MC, Wu YT. Design and tailoring of the nanotubular arrayed architecture of hydrous RuO2 for next generation supercapacitors. Nano Lett. 2006;6(12):2690-5.
[106] Yang GW, Xu CL, Li HL. Electrodeposited nickel hydroxide on nickel foam with ultrahigh capacitance. Chem Commun. 2008(48):6537-9.
[107] Kim JH, Zhu K, Yan Y, Perkins CL, Frank AJ. Microstructure and pseudocapacitive properties of electrodes constructed of oriented NiO-TiO2 nanotube arrays. Nano Lett. 2010;10(10):4099-104.
[108] Shrestha NK, Yang M, Schmuki P. Self-Ordered Nanoporous Nickel Oxide/Fluoride Composite Film with Strong Electrochromic Contrast. Electrochem Solid St. 2010;13(8):C21-C4.
[109] Sun W, Zheng RL, Chen XY. Symmetric redox supercapacitor based on micro-fabrication with three-dimensional polypyrrole electrodes. J Power Sources. 2010;195(20):7120-5.
[110] Zhang LL, Zhao S, Tian XN, Zhao XS. Layered Graphene Oxide Nanostructures with Sandwiched Conducting Polymers as Supercapacitor Electrodes. Langmuir : the ACS journal of surfaces and colloids. 2010;26(22):17624-8.
[111] Liang RL, Cao HQ, Qian D. MoO3 nanowires as electrochemical pseudocapacitor materials. Chem Commun. 2011;47(37):10305-7.

[112] Lu F, Qiu MC, Qi X, Yang LW, Yin JJ, Hao GL, et al. Electrochemical properties of high-power supercapacitors using ordered NiO coated Si nanowire array electrodes. Applied Physics a-Materials Science & Processing. 2011;104(2):545-50.
[113] Sun X, Wang GK, Hwang JY, Lian J. Porous nickel oxide nano-sheets for high performance pseudocapacitance materials. J Mater Chem. 2011;21(41):16581-8.
[114] Chen Z, Weng D, Wang XL, Cheng YH, Wang G, Lu YF. Ready fabrication of thin-film electrodes from building nanocrystals for micro-supercapacitors. Chem Commun. 2012;48(31):3736-8.
[115] Duay J, Gillette E, Liu R, Lee SB. Highly flexible pseudocapacitor based on freestanding heterogeneous MnO2/conductive polymer nanowire arrays. Phys Chem Chem Phys. 2012;14(10):3329-37.
[116] Hasan M, Jamal M, Razeeb KM. Coaxial NiO/Ni nanowire arrays for high performance pseudocapacitor applications. Electrochim Acta. 2012;60:193-200.
[117] Li JX, Yang M, Wei JP, Zhou Z. Preparation and electrochemical performances of doughnut-like Ni(OH)(2)-Co(OH)(2) composites as pseudocapacitor materials. Nanoscale. 2012;4(15):4498-503.
[118] Liang K, Tang X, Hu W. High-performance three-dimensional nanoporous NiO film as a supercapacitor electrode. J Mater Chem. 2012;22(22):11062.
[119] Lu X, Huang X, Xie S, Zhai T, Wang C, Zhang P, et al. Controllable synthesis of porous nickel–cobalt oxide nanosheets for supercapacitors. J Mater Chem. 2012;22(26):13357.
[120] Mahmood Q, Kim WS, Park HS. Structure and compositional control of MoO3 hybrids assembled by nanoribbons for improved pseudocapacitor rate and cycle performance. Nanoscale. 2012;4(24):7855-60.
[121] Pan GX, Xia X, Cao F, Tang PS, Chen HF. Porous Co(OH)(2)/Ni composite nanoflake array for high performance supercapacitors. Electrochim Acta. 2012;63:335-40.
[122] Salunkhe RR, Jang K, Lee SW, Ahn H. Aligned nickel-cobalt hydroxide nanorod arrays for electrochemical pseudocapacitor applications. Rsc Advances. 2012;2(8):3190-3.
[123] Sawangphruk M, Pinitsoontorn S, Limtrakul J. Surfactant-assisted electrodeposition and improved electrochemical capacitance of silver-doped manganese oxide pseudocapacitor electrodes. J Solid State Electrochem. 2012;16(8):2623-9.
[124] Tian X, Cheng C, Qian L, Zheng B, Yuan H, Xie S, et al. Microwave-assisted non-aqueous homogenous precipitation of nanoball-like mesoporous α-Ni(OH)2 as a precursor for NiOx and its application as a pseudocapacitor. J Mater Chem. 2012;22(16):8029.
[125] Xia XH, Tu JP, Zhang YQ, Wang XL, Gu CD, Zhao XB, et al. High-Quality Metal Oxide Core/Shell Nanowire Arrays on Conductive Substrates for Electrochemical Energy Storage. Acs Nano. 2012;6(6):5531-8.
[126] Yan J, Fan Z, Sun W, Ning G, Wei T, Zhang Q, et al. Advanced Asymmetric Supercapacitors Based on Ni(OH)2/Graphene and Porous Graphene Electrodes with High Energy Density. Adv Funct Mater. 2012;22(12):2632-41.
[127] Yan J, Sun W, Wei T, Zhang Q, Fan Z, Wei F. Fabrication and electrochemical performances of hierarchical porous Ni(OH)2 nanoflakes anchored on graphene sheets. J Mater Chem. 2012;22(23):11494.

[128] Yang L, Cheng S, Ding Y, Zhu XB, Wang ZL, Liu ML. Hierarchical Network Architectures of Carbon Fiber Paper Supported Cobalt Oxide Nanonet for High-Capacity Pseudocapacitors. Nano Lett. 2012;12(1):321-5.
[129] Cross AD, Morel A, Drozd M, Olcomendy I, Hollenkamp AF, Donne SW. Active mass analysis on thin films of electrodeposited manganese dioxide for electrochemical capacitors. Electrochim Acta. 2013;87:133-9.
[130] Han JB, Dou YB, Zhao JW, Wei M, Evans DG, Duan X. Flexible CoAl LDH@PEDOT Core/Shell Nanoplatelet Array for High-Performance Energy Storage. Small. 2013;9(1):98-106.
[131] Hsu HY, Chang KH, Salunkhe RR, Hsu CT, Hu CC. Synthesis and characterization of mesoporous Ni-Co oxy-hydroxides for pseudocapacitor application. Electrochim Acta. 2013;94:104-12.
[132] Huang J, Lei T, Wei X, Liu X, Liu T, Cao D, et al. Effect of Al-doped β-Ni(OH)2 nanosheets on electrochemical behaviors for high performance supercapacitor application. J Power Sources. 2013;232(0):370-5.
[133] Huang PH, Pech D, Lin RY, McDonough JK, Brunet M, Taberna PL, et al. On-chip micro-supercapacitors for operation in a wide temperature range. Electrochem Commun. 2013;36:53-6.
[134] Jiang Y, Wang P, Zang X, Yang Y, Kozinda A, Lin L. Uniformly embedded metal oxide nanoparticles in vertically aligned carbon nanotube forests as pseudocapacitor electrodes for enhanced energy storage. Nano Lett. 2013;13(8):3524-30.
[135] Jin M, Zhang GG, Yu F, Li WF, Lu W, Huang HT. Sponge-like Ni(OH)(2)-NiF2 composite film with excellent electrochemical performance. Phys Chem Chem Phys. 2013;15(5):1601-5.
[136] Li WY, Li G, Sun JQ, Zou RJ, Xu KB, Sun YG, et al. Hierarchical heterostructures of MnO2 nanosheets or nanorods grown on Au-coated Co3O4 porous nanowalls for high-performance pseudocapacitance. Nanoscale. 2013;5(7):2901-8.
[137] Sarma B, Jurovitzki AL, Smith YR, Mohanty SK, Misra M. Redox-Induced Enhancement in Interfacial Capacitance of the Titania Nanotube/Bismuth Oxide Composite Electrode. ACS Appl Mater Interfaces. 2013;5(5):1688-97.
[138] Wang L, Ji H, Wang S, Kong L, Jiang X, Yang G. Preparation of Fe3O4 with high specific surface area and improved capacitance as a supercapacitor. Nanoscale. 2013;5(9):3793-9.
[139] Xiong G, Hembram KPSS, Reifenberger RG, Fisher TS. MnO2-coated graphitic petals for supercapacitor electrodes. J Power Sources. 2013;227:254-9.
[140] Yang F, Yao JY, Liu FL, He HC, Zhou M, Xiao P, et al. Ni-Co oxides nanowire arrays grown on ordered TiO2 nanotubes with high performance in supercapacitors. J Mater Chem A. 2013;1(3):594-601.
[141] Zhang GG, Li WF, Xie KY, Yu F, Huang HT. A One-Step and Binder-Free Method to Fabricate Hierarchical Nickel-Based Supercapacitor Electrodes with Excellent Performance. Adv Funct Mater. 2013;23(29):3675-81.
[142] Beguin F, Frackowiak E. Supercapacitors: Materials, Systems and Applications: Wiley; 2013.
[143] Kraft A. Doped diamond: A compact review on a new, versatile electrode material. Int J Electrochem Sc. 2007;2(5):355-85.
[144] Vinokur N, Miller B, Avyigal Y, Kalish R. Electrochemical Behavior of Boron-Doped Diamond Electrodes. J Electrochem Soc. 1996;143(10):L238-L40.

[145] Gao F, Yang NJ, Nebel CE. Highly stable platinum nanoparticles on diamond. Electrochim Acta. 2013;112:493-9.
[146] Gao F, Yang NJ, Obloh H, Nebel CE. Shape-controlled platinum nanocrystals on boron-doped diamond. Electrochem Commun. 2013;30(0):55-8.
[147] Gao F, Yang NJ, Smirnov W, Obloh H, Nebel CE. Size-controllable and homogeneous platinum nanoparticles on diamond using wet chemically assisted electrodeposition. Electrochim Acta. 2013;90(0):445-51.
[148] Atkins PW. Physical chemistry. 6th ed. Oxford: Oxford University Press; 1998.
[149] Sawyer DT, Sobkowiak A, Roberts JL. Electrochemistry for chemists. 2nd ed. New York ; Chichester: Wiley; 1995.
[150] Gerischer H. The Impact of Semiconductors on the Concepts of Electrochemistry. Electrochim Acta. 1990;35(11-12):1677-99.
[151] Bard AJ, Faulkner LR. Electrochemical methods : fundamentals and applications. 2nd ed. New Delhi: Wiley India Ltd.; 2006.
[152] Bockris JOM, Reddy AKN, Gamboa-Aldeco ME. Modern electrochemistry. 2nd ed. New York: Plenum Press; 1998.
[153] Liu W, Yan X, Lang J, Xue Q. Effects of concentration and temperature of EMIMBF4/acetonitrile electrolyte on the supercapacitive behavior of graphene nanosheets. J Mater Chem. 2012;22(18):8853.
[154] Bloomfie.Va, Dewan RK. Viscosity of Liquid Mixtures. J Phys Chem. 1971;75(20):3113-&.
[155] MacFarlane DR, Forsyth M, Izgorodina EI, Abbott AP, Annat G, Fraser K. On the concept of ionicity in ionic liquids. Phys Chem Chem Phys. 2009;11(25):4962-7.
[156] Zhang LL, Zhao XS. Carbon-based materials as supercapacitor electrodes. Chem Soc Rev. 2009;38(9):2520-31.
[157] Randstroem S, Appetecchi GB, Lagergren C, Moreno A, Passerini S. The influence of air and its components on the cathodic stability of N-butyl-N-methylpyffolidinium bis(trifluoromethanesulfonyl)imide. Electrochim Acta. 2007;53(4):1837-42.
[158] Gao F, Wolfer MT, Nebel CE. Highly porous diamond foam as a thin-film micro-supercapacitor material. Carbon. 2014;80(0):833-40.
[159] Gao F, Lewes-Malandrakis G, Wolfer MT, Muller-Sebert W, Gentile P, Aradilla D, et al. Diamond-coated silicon wires for supercapacitor applications in ionic liquids. Diamond Relat Mater. 2015;51:1-6.
[160] Taberna PL, Portet C, Simon P. Electrode surface treatment and electrochemical impedance spectroscopy study on carbon/carbon supercapacitors. Appl Phys A. 2006;82(4):639-46.
[161] Berton N, Brachet M, Thissandier F, Le Bideau J, Gentile P, Bidan G, et al. Wide-voltage-window silicon nanowire electrodes for micro-supercapacitors via electrochemical surface oxidation in ionic liquid electrolyte. Electrochem Commun. 2014;41:31-4.
[162] Koneshan S, Rasaiah JC, Lynden-Bell RM, Lee SH. Solvent Structure, Dynamics, and Ion Mobility in Aqueous Solutions at 25 °C. The Journal of Physical Chemistry B. 1998;102(21):4193-204.
[163] Zoltowski P. On the electrical capacitance of interfaces exhibiting constant phase element behaviour. J Electroanal Chem. 1998;443(1):149-54.
[164] Hsu CH, Mansfeld F. Technical note: Concerning the conversion of the constant phase element parameter Y-0 into a capacitance. Corrosion. 2001;57(9):747-8.

[165] Pech D, Brunet M, Taberna PL, Simon P, Fabre N, Mesnilgrente F, et al. Elaboration of a microstructured inkjet-printed carbon electrochemical capacitor. J Power Sources. 2010;195(4):1266-9.
[166] Huang P, Heon M, Pech D, Brunet M, Taberna PL, Gogotsi Y, et al. Micro-supercapacitors from carbide derived carbon (CDC) films on silicon chips. J Power Sources. 2013;225:240-4.
[167] Osterloh FE. Inorganic materials as catalysts for photochemical splitting of water. Chem Mater. 2008;20(1):35-54.
[168] Gilroy D, Conway B. Surface oxidation and reduction of platinum electrodes: Coverage, kinetic and hysteresis studies. Can J Chem. 1968;46(6):875-90.
[169] Will FG. Hydrogen Adsorption on Platinum Single Crystal Electrodes. J Electrochem Soc. 1965;112(4):451.
[170] Aradilla D, Bidan G, Gentile P, Weathers P, Thissandier F, Ruiz V, et al. Novel hybrid micro-supercapacitor based on conducting polymer coated silicon nanowires for electrochemical energy storage. Rsc Advances. 2014;4(50):26462.
[171] Gunawardena G, Hills G, Montenegro I, Scharifker B. Electrochemical Nucleation .1. General-Considerations. J Electroanal Chem. 1982;138(2):225-39.
[172] Krumm R, Guel B, Schmitz C, Staikov G. Nucleation and growth in electrodeposition of metals on n-Si(111). Electrochim Acta. 2000;45(20):3255-62.
[173] Pozio A, De Francesco M, Cemmi A, Cardellini F, Giorgi L. Comparison of high surface Pt/C catalysts by cyclic voltammetry. J Power Sources. 2002;105(1):13-9.
[174] Powell RA, Rossnagel SM. PVD for microelectronics : sputter deposition applied to semiconductor manufacturing. San Diego, Calif. ; London: Academic Press; 1999.
[175] Lu JQ, Kushner MJ. Trench filling by ionized metal physical vapor deposition. Journal of Vacuum Science & Technology a-Vacuum Surfaces and Films. 2001;19(5):2652-63.
[176] Bode H, Dehmelt K, Witte J. Zur kenntnis der nickelhydroxidelektrode—I.Über das nickel (II)-hydroxidhydrat. Electrochim Acta. 1966;11(8):1079-IN1.
[177] Oliva P, Leonardi J, Laurent JF, Delmas C, Braconnier JJ, Figlarz M, et al. Review of the Structure and the Electrochemistry of Nickel Hydroxides and Oxy-Hydroxides. J Power Sources. 1982;8(2-3):229-55.
[178] Singh D. Characteristics and effects of gamma-NiOOH on cell performance and a method to quantify it in nickel electrodes. J Electrochem Soc. 1998;145(1):116-20.
[179] Leger C, Tessier C, Menetrier M, Denage C, Delmas C. Investigation of the second discharge plateau of the beta(III)-NiOOH/beta(II)-Ni(OH)(2) system. J Electrochem Soc. 1999;146(3):924-32.
[180] Brulle T, Denisenko A, Sternschulte H, Stimming U. Catalytic activity of platinum nanoparticles on highly boron-doped and 100-oriented epitaxial diamond towards HER and HOR. Physical chemistry chemical physics : PCCP. 2011;13(28):12883-91.
[181] Bajpai R, Roy S, Kumar P, Bajpai P, Kulshrestha N, Rafiee J, et al. Graphene supported platinum nanoparticle counter-electrode for enhanced performance of dye-sensitized solar cells. ACS Appl Mater Interfaces. 2011;3(10):3884-9.
[182] Yu RQ, Chen LW, Liu QP, Lin JY, Tan KL, Ng SC, et al. Platinum deposition on carbon nanotubes via chemical modification. Chem Mater. 1998;10(3):718-22.
[183] Lu X, Hu J, Foord JS, Wang Q. Electrochemical deposition of Pt–Ru on diamond electrodes for the electrooxidation of methanol. J Electroanal Chem. 2011;654(1-2):38-43.

[184] Arunagiri T, Golden TD, Chyan O. Study of palladium metal particle deposition on the conductive diamond surface by XRD, XPS and electrochemistry. Mater Chem Phys. 2005;92(1):152-8.
[185] Kim P, Joo JB, Kim W, Kim J, Song IK, Yi J. NaBH4-assisted ethylene glycol reduction for preparation of carbon-supported Pt catalyst for methanol electro-oxidation. J Power Sources. 2006;160(2):987-90.
[186] Jeon MK, Won JY, Lee KR, Woo SI. Highly active PtRuFe/C catalyst for methanol electro-oxidation. Electrochem Commun. 2007;9(9):2163-6.
[187] Wang J, Swain GM. Fabrication and evaluation of platinum/diamond composite electrodes for electrocatalysis - Preliminary studies of the oxygen-reduction reaction. J Electrochem Soc. 2003;150(1):E24-E32.
[188] Maillard F, Schreier S, Hanzlik M, Savinova ER, Weinkauf S, Stimming U. Influence of particle agglomeration on the catalytic activity of carbon-supported Pt nanoparticles in CO monolayer oxidation. Phys Chem Chem Phys. 2005;7(2):385-93.
[189] La-Torre-Riveros L, Guzman-Blas R, Mendez-Torres AE, Prelas M, Tryk DA, Cabrera CR. Diamond nanoparticles as a support for Pt and PtRu catalysts for direct methanol fuel cells. ACS Appl Mater Interfaces. 2012;4(2):1134-47.
[190] Smirnov W, Hees JJ, Brink D, Müller-Sebert W, Kriele A, Williams OA, et al. Anisotropic etching of diamond by molten Ni particles. Appl Phys Lett. 2010;97(7):073117.
[191] Ohashi T, Sugimoto W, Takasu Y. Catalytic etching of {100}-oriented diamond coating with Fe, Co, Ni, and Pt nanoparticles under hydrogen. Diamond Relat Mater. 2011;20(8):1165-70.
[192] Bennett JA, Show Y, Wang S, Swain GM. Pulsed Galvanostatic Deposition of Pt Particles on Microcrystalline and Nanocrystalline Diamond Thin-Film Electrodes. J Electrochem Soc. 2005;152(5):E184-E92.
[193] Hu J, Lu X, Foord JS. Nanodiamond pretreatment for the modification of diamond electrodes by platinum nanoparticles. Electrochem Commun. 2010;12(5):676-9.
[194] Hu J, Lu X, Foord JS, Wang Q. Electrochemical deposition of Pt nanoparticles on diamond substrates. Phys Status Solidi A. 2009;206(9):2057-62.
[195] Shpilevaya I, Smirnov W, Hirsz S, Yang N, Nebel CE, Foord JS. Nanostructured diamond decorated with Pt particles: preparation and electrochemistry. Rsc Advances. 2014;4(2):531-7.
[196] Jaeger NI, Jourdan AL, Schulzekloff G. Effect of the Size of Platinum Particles on the Chemisorption of Oxygen. Journal of the Chemical Society-Faraday Transactions. 1991;87(8):1251-7.
[197] Kodera F, Kuwahara Y, Nakazawa A, Umeda M. Electrochemical corrosion of platinum electrode in concentrated sulfuric acid. J Power Sources. 2007;172(2):698-703.
[198] Yang N, Smirnov W, Nebel CE. Three-dimensional electrochemical reactions on tip-coated diamond nanowires with nickel nanoparticles. Electrochem Commun. 2013;27(0):89-91.
[199] Gao F, Thomann R, Nebel CE. Aligned Pt-diamond core-shell nanowires for electrochemical catalysis. Electrochem Commun. 2015;50(0):32-5.
[200] Winterbottom WL. Equilibrium shape of a small particle in contact with a foreign substrate. Acta Metall. 1967;15(2):303-10.

[201] Kiran R, Scorsone E, Mailley P, Bergonzo P. Quasi-Real Time Quantification of Uric Acid in Urine Using Boron Doped Diamond Microelectrode with in Situ Cleaning. Anal Chem. 2012;84(23):10207-13.
[202] Hoffmann R, Obloh H, Tokuda N, Yang N, Nebel CE. Fractional surface termination of diamond by electrochemical oxidation. Langmuir. 2012;28(1):47-50.
[203] Hoffmann R. Towards the solid protein surface. Stuttgart: Fraunhofer-Verl.; 2013.
[204] Zhu D, Zhang LH, Ruther RE, Hamers RJ. Photo-illuminated diamond as a solid-state source of solvated electrons in water for nitrogen reduction. Nat Mat. 2013;12(9):836-41.
[205] Nakabayashi S, Ohta N, Fujishima A. Dye sensitization of synthetic p-type diamond electrode. Phys Chem Chem Phys. 1999;1(17):3993-7.
[206] Yao SA, Ruther RE, Zhang LH, Franking RA, Hamers RJ, Berry JF. Covalent Attachment of Catalyst Molecules to Conductive Diamond: CO2 Reduction Using "Smart" Electrodes. J Am Chem Soc. 2012;134(38):15632-5.
[207] Zegkinoglou I, Cook PL, Johnson PS, Yang WL, Guo JH, Pickup D, et al. Electronic Structure of Diamond Surfaces Functionalized by Ru(tpy)(2). J Phys Chem C. 2012;116(26):13877-83.
[208] Yeap WS, Bevk D, Liu X, Krysova H, Pasquarelli A, Vanderzande D, et al. Diamond functionalization with light-harvesting molecular wires: improved surface coverage by optimized Suzuki cross-coupling conditions. Rsc Advances. 2014;4(79):42044-53.
[209] Yeap WS, Liu X, Bevk D, Pasquarelli A, Lutsen L, Fahlman M, et al. Functionalization of Boron-Doped Nanocrystalline Diamond with N3 Dye Molecules. ACS Appl Mater Interfaces. 2014;6(13):10322-9.
[210] Christianson JR, Zhu D, Hamers RJ, Schmidt JR. Mechanism of N-2 Reduction to NH3 by Aqueous Solvated Electrons. J Phys Chem B. 2014;118(1):195-203.
[211] Zhang LH, Zhu D, Nathanson GM, Hamers RJ. Selective Photoelectrochemical Reduction of Aqueous CO2 to CO by Solvated Electrons. Angew Chem Int Edit. 2014;53(37):9746-+.
[212] Diederich L, Küttel OM, Aebi P, Schlapbach L. Electron affinity and work function of differently oriented and doped diamond surfaces determined by photoelectron spectroscopy. Surf Sci. 1998;418(1):219-39.
[213] Diederich L, Kuttel OM, Ruffieux P, Pillo T, Aebi P, Schlapbach L. Photoelectron emission from nitrogen- and boron-doped diamond (100) surfaces. Surf Sci. 1998;417(1):41-52.
[214] Takeuchi D, Kato H, Ri GS, Yamada T, Vinod PR, Hwang D, et al. Direct observation of negative electron affinity in hydrogen-terminated diamond surfaces. Appl Phys Lett. 2005;86(15):152103.
[215] Hees J, Hoffmann R, Kriele A, Smirnov W, Obloh H, Glorer K, et al. Nanocrystalline Diamond Nanoelectrode Arrays and Ensembles. Acs Nano. 2011;5(4):3339-46.
[216] du Toit H, Di Lorenzo M. Glucose Oxidase Directly Immobilized onto Highly Porous Gold Electrodes for Sensing and Fuel Cell applications. Electrochim Acta. 2014;138:86-92.
[217] Jiang D, Liu Q, Wang K, Qian J, Dong X, Yang Z, et al. Enhanced non-enzymatic glucose sensing based on copper nanoparticles decorated nitrogen-doped graphene. Biosens Bioelectron. 2014;54:273-8.

[218] Periasamy AP, Chang YJ, Chen SM. Amperometric glucose sensor based on glucose oxidase immobilized on gelatin-multiwalled carbon nanotube modified glassy carbon electrode. Bioelectrochemistry. 2011;80(2):114-20.
[219] Toghill KE, Xiao L, Phillips MA, Compton RG. The non-enzymatic determination of glucose using an electrolytically fabricated nickel microparticle modified boron-doped diamond electrode or nickel foil electrode. Sensors Actuators B: Chem. 2010;147(2):642-52.
[220] Wang Q, Subramanian P, Li M, Yeap WS, Haenen K, Coffinier Y, et al. Non-enzymatic glucose sensing on long and short diamond nanowire electrodes. Electrochem Commun. 2013;34:286-90.
[221] Watanabe T, Einaga Y. Design and fabrication of nickel microdisk-arrayed diamond electrodes for a non-enzymatic glucose sensor based on control of diffusion profiles. Biosens Bioelectron. 2009;24(8):2684-9.
[222] Zhao W, Xu JJ, Qiu QQ, Chen HY. Nanocrystalline diamond modified gold electrode for glucose biosensing. Biosens Bioelectron. 2006;22(5):649-55.
[223] Zou YS, He LL, Dou K, Wang SL, Ke PL, Wang AY. Amperometric glucose sensor based on boron doped microcrystalline diamond film electrode with different boron doping levels. Rsc Advances. 2014;4(102):58349-56.

Acknowledgement

I would like to thank Prof. Dr. Oliver Ambacher, Dr. Christoph E. Nebel, Dr. Volker Cimalla and Dr. Nianjun Yang for guiding and training me throughout my work during my PhD work. I would also like to thank Prof. Dr. Jose Antonio Garrido Ariza for his interest in this thesis and his contribution as the second referee.

I gratefully acknowledge the funding from European Commission Seventh Framework Programs (FP7) *NEST* and *MatCon*. The equal opportunity that FP7 projects provided to EU and non-EU citizens is highly appreciated.

I sincerely thank the pioneering work from Dr. Waldemar Smirnov, Dr. Hiromitsu Kato and Dr. Jan Jakob Hees. Working upon their work makes this thesis possible. Also, my special thanks go to Dr. René Hoffmann who has always been so open to my discussions (both scientific and non-scientific) and enlightened me in numerous ways.

I owe a lot to Fraunhofer Institute for Applied Solid State Physics (IAF) for providing me this great research platform to finish my PhD work. I especially express my gratitude to

- Dr. Wolfgang Müller-Sebert, Dr. Harald Obloh, Dr. Marco T. Wolfer, Mr. Dietmar Brink, Ms. Georgia Lewes-Malandrakis, Mr. Sascha Klingelmeier, Ms. Anli Ding and Mr. Johannes Hartwiger the help and discussion in materials processing, devices designing and sample measurements
- Colleagues from the TE department, Dr. Christian Giese, Mr. Wolfgang Luppold, Ms. Sabine Bühler, for assistance for etching and device processing
- Colleagues from workshop, especially Mr. Heiko Mohr, for fabricate experimental devices which made my research so much easier

Also, I would like to thank all the people, no matter mentioned above or not, for working together with me during my time here. You are an indispensable part of my life here in Germany. The lunch-time talks, department/institute trips and group dinners mean a lot to people who are 15000 km away from home.

Finally, I am deeply obliged to my parents: Mrs. Qi Li and Mr. Song Gao, and my girlfriend Ms. Yi Gong, for their unconditional supports at the time of depression and difficulties.